Nanoscale

REVIEW

View Article Online
View Journal | View Issue



Cite this: *Nanoscale*, 2025, **17**, 25426

# Recent progress in the synthesis of $CuCr_2O_4$ nanomaterials and their composites for catalytic, energy, and biomedical applications: a state-of-the-art-review

Kajalben Patel,[a] Mamta Patil,[a] Yogita Abhale,*[a] Kun-Yi Andrew Lin,[b] Kar Ban Tan,[c] Ankush Chauhan,[d] Abhinav Kumar,[e] Vishnu Adole,[f] Majid S. Jabir[g] and Suresh Ghotekar*[d]

Copper chromite nanoparticles ($CuCr_2O_4$ NPs) are in the spotlight of modern nanoscience due to their versatile applications across various scientific and industrial domains. This review addresses the synthesis of $CuCr_2O_4$ NPs, metal-doped $CuCr_2O_4$ NPs, and nanocomposites (NCs), emphasizing the key parameters, *viz*., reaction time, pH, temperature, precursor concentration, and the choice of fuel or surfactant, influencing their morphology, crystallinity, and functional properties. $CuCr_2O_4$ NPs are fabricated using several chemical methods, namely, sol–gel, co-precipitation, hydrothermal, solution combustion, and ball-milling, with different types of fuels or surfactants serving as complexing agents. These materials exhibit remarkable thermal, electrical, and catalytic characteristics. The discussion extends to their broad spectrum of applications, including biological activities such as antimicrobial, anticancer, and bone regeneration as well as their genotoxic impact. We also explore their role in photocatalysis, heterogeneous catalysis, and electrochemical applications, including supercapacitors and lithium-ion batteries. The emerging utility of $CuCr_2O_4$ NPs in sensor development is also highlighted. This review covers the recent advancements in the synthesis of $CuCr_2O_4$ NPs, highlighting their key challenges and future directions. Analyzing the structure–property relationships and the influence of synthesis parameters on their performance provides valuable insights into optimizing the design and functionalization of $CuCr_2O_4$ NPs for specific applications.

Received 21st July 2025,
Accepted 12th September 2025

DOI: 10.1039/d5nr03084f

rsc.li/nanoscale



## 1. Introduction

In recent years, nanotechnology has emerged in the limelight through its diverse applicability in various fields, ushering in what can be called a "nano-era". Richard Feynman's (1959) talk "There is plenty of room at the bottom" and the invention of the scanning tunneling microscope (1981) paved the way for the development of nanoscience and nanotechnology. Japanese scientist Norio Taniguchi first used the term "nanotechnology" to describe semiconductor processes at the nanoscale about fifteen years after Feynman's discussion. They promoted the idea that materials may be processed, separated, consolidated, and deformed by a single atom or molecule as part of nanotechnology.[1]

In the present scenario, there has been considerable interest in advancing spinel oxide nanoparticles (NPs) across various disciplines of study. Their beneficial traits, including affordability, enhanced efficiency, effortless recuperation, and superior recyclability, suggest that they are potent catalysts.[2–5] The remarkable catalytic activity of spinel oxides makes them noteworthy. Spinel oxides are inexpensive, harmless, and extremely stable materials with good acid and alkali resistance and high melting temperatures, and their NPs have a comparatively large surface area. Due to these qualities, they can be utilized as solid heterogeneous catalysts in organic chemical

[a]*Department of Chemistry, Government College Daman (Veer Narmad South Gujarat University, Surat), Daman 396210, UT of DNH & DD, India.*
*E-mail: mahayogi.85@gmail.com*
[b]*Department of Environmental Engineering & Innovation and Development Center of Sustainable Agriculture, National Chung Hsing University, Taichung, 40227, Taiwan*
[c]*Department of Chemistry, Faculty of Science, University Putra Malaysia, 43400 UPM, Serdang, Selangor, Malaysia*
[d]*Centre for Herbal Pharmacology and Environmental Sustainability, Chettinad Academy of Research and Education, Kelambakkam, Tamil Nadu 603103, India.*
*E-mail: ghotekarsuresh7@gmail.com*
[e]*Centre for Research Impact & Outcome, Chitkara University Institute of Engineering and Technology, Chitkara University, Rajpura 140401, Punjab, India*
[f]*Department Chemistry, Mahatma Gandhi Vidyamandir's Loknete Vyankatrao Hiray Arts, Science and Commerce College (Savitribai Phule Pune University), Panchavati, Nashik, Maharashtra 422003, India*
[g]*College of Applied Sciences, University of Technology, Baghdad, Iraq*

reactions.[6–8] The most common type of spinel chromite is binary transition metal oxides, $M^{2+}B_2^{3+}O_4^{2-}$, where M = $Mg^{2+}$, $Mn^{2+}$, $Co^{2+}$, $Ni^{2+}$, $Cu^{2+}$, or $Zn^{2+}$. Spinel nanostructures have garnered attention due to their diverse applications in various fields, *including* nanomedicine, photocatalysis, catalysis, energy storage, lithium-ion batteries, and sensors.[2,9–11] $CuCr_2O_4$ is a fascinating chromate spinel due to its cost-effectiveness and non-toxicity. As a tetragonally deformed normal spinel, $CuCr_2O_4$ has an axial ratio ($c/a$) of less than 1, suggesting that its $c$-axis is compressed relative to its $a$-axis.[7] $Cr^{3+}$ ions occupy the octahedral (B) sites, while $Cu^{2+}$ ions are positioned at the tetrahedral (M) sites, and the perfect crystal is anticipated to be an insulator. At normal and high temperatures, spinel $CuCr_2O_4$ crystallizes into a cubic phase and tetragonal phase, respectively. Its first-order phase transition occurs at approximately 854 K (upon heating).[12,13] According to the Jahn-Teller phenomenon, spinel oxides containing copper have excellent thermal stability.[14]

Numerous approaches have been documented in the literature for preparing $CuCr_2O_4$ NPs, including hydrothermal,[15] co-precipitation,[16] sol–gel,[17] solution combustion,[8] microwave-assisted,[18] and mechanical ball milling.[19] Various fuels and surfactants, such as ethylene glycol, CTAB, tartaric acid, citric acid, glycine, and glucose, have been utilized as capping agents during the synthesis process. These agents are crucial in the synthesis of NPs, given that they enhance the monodispersity, reduce the particle size, and minimize the aggregation of nanoparticles. Surfactants reduce the surface tension of the solution, lowering the energy required to create a new phase from the precursor ions.[20]

$CuCr_2O_4$ has been identified as a p-type semiconductor ($E_g$ = 1.40 eV) for a range of photocatalytic applications.[15,21–27] Materials known as catalysts accelerate chemical reactions without being consumed by the reaction; however, they are frequently difficult to separate and recover.[28–30] A green and cost-effective catalyst should have minimal preparation costs, high activity, selectivity, stability, ease of separation, and recyclability.[31–33] Surprisingly, $CuCr_2O_4$ NPs function as a heterogeneous catalyst in several reactions, such as the thermal disintegration of ammonium perchlorate (AP),[34] oxidation of aniline to azoxybenzene,[35] preparation of pyrazine,[36] synthesis of triarylamine,[16] oxidation of benzene to phenol,[15,24] hydrogenation of 2-furfuraldehyde,[37] and synthesis of biscoumarin and pyrano[*c*]chromene,[38] and this catalyst effectively catalyzes toluene oxidation by interfering with C–H bond activation[39] and synthesis of [1]benzopyran azo dyes, *etc*.[40]

Intriguingly, $CuCr_2O_4$ nanomaterials/composites show a broad spectrum of biological activities, including anticancer,[41] antibacterial,[42,43] bone regeneration,[44] hemolysis,[41] and genotoxicity tests,[45] with significant potential. Furthermore, $CuCr_2O_4$ nanomaterials and composites have been studied for energy storage applications. The development of high-energy and high-power batteries,[46] as well as hybrid supercapacitor electrodes due to their capacitive characteristics, cyclic stability, and high power density,[47] is crucial for meeting energy storage needs. Rechargeable metal–air batteries based on oxygen electrocatalysis are a viable alternative, particularly when the energy source is intermittent, such as solar or wind. These batteries use bifunctional oxygen electrocatalysis, which includes both oxygen reduction (ORR) and oxygen evolution processes (OER).[48] Also, $CuCr_2O_4$ has potential as an electrocatalyst in electrochemical hydrogen storage systems, providing a sustainable solution to renewable energy technology.[49]

This review thoroughly examined $CuCr_2O_4$ NPs. The current literature was gathered from Google Scholar, ResearchGate, PubMed, Scopus, and books using the search terms "synthesis + $CuCr_2O_4$ NPs/doped metal/nanocomposites + energy storage + biological + catalytic/photocatalytic applications". Fig. 1 shows a pie chart of the data received from these keywords. A significant amount of studies has been done on the synthesis and characterization of $CuCr_2O_4$ NPs that can be applied in a variety of scientific and engineering domains. The current summary will help researchers better understand the opportunities and challenges associated with the production of $CuCr_2O_4$ NPs.

## 2. Synthesis of $CuCr_2O_4$ NPs

The growth and production processes of $CuCr_2O_4$ NPs determine their structure and shape. To date, $CuCr_2O_4$ NPs have been synthesized using several processes, such as sol–gel, co-precipitation, solution combustion, precipitation, hydrothermal, microwave-assisted procedures, and mechanical ball milling, which are summarized in Table 1.

### 2.1. Pristine $CuCr_2O_4$ NPs

**2.1.1. Sol–gel method.** The sol–gel approach effectively produces very uniform NPs without any foreign material or co-

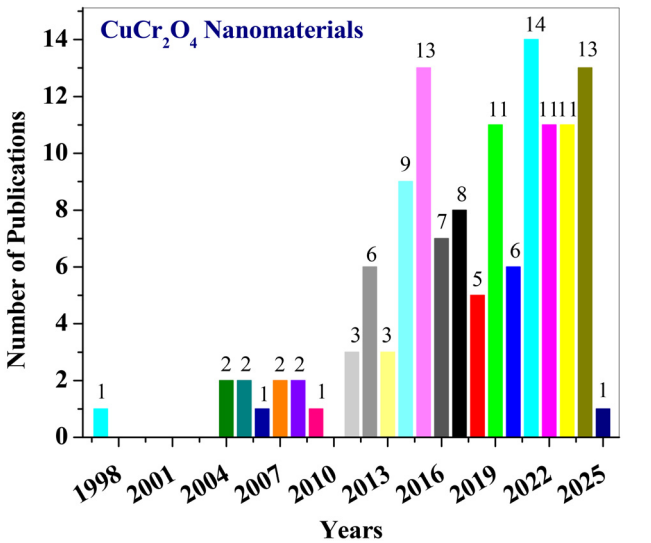


Fig. 1 Data of the number of papers published on "synthesis of $CuCr_2O_4$ nanomaterials and their applications" from Google Scholar, ResearchGate, PubMed, Scopus, and Book database.

**Table 1** Summary of the synthesis methods, characterization techniques, morphology, and applications of $CuCr_2O_4$ NPs

| Synthesis method | Morphology | Particle size (nm) | Characterization techniques | Applications | Ref. |
|---|---|---|---|---|---|
| Sol–gel combustion | Laminate, octahedral, and spherical | — | XRD, UV-Vis, FTIR, DSC, TEM, SEM-EDX, ATR | Selective absorber coatings | 17 |
| Sol–gel | Spherical | 30–55 | XRD, FESEM, TEM, TGA-DSC | Catalytic activity | 50 |
| | Semi spherical | — | XRD, UV-vis-DRS, FTIR, SEM | Photocatalytic activity | 51 |
| Sol–gel | Spherical | 37 | FT-IR, XRD, BET, FESEM-EDS | Electrochemical hydrogen storage | 49 |
| Green synthesis | Spherical | 54 | | | |
| Sol–gel | Quasi-spherical | 20–60 | XRD, UV–Vis, FTIR, TEM, SEM, RSR, MEM | Photocatalytic activity | 52 |
| | Uniform | 850 °C < 100 | XRD, FTIR. SEM, VSM | Microwave absorber | 53 |
| | Poly tetragonal | — | XRD, FTIR, SEM | Antibacterial activity | 42 |
| | Spherical | 33 | UV-Vis-DRS, FESEM, XRD, FTIR | — | 55 |
| | Cubic | 20–60 | XRD, FTIR, SEM. TGA/DTA | Catalytic activity | 56 |
| | — | 34 | XRD, XPS, SEM, HRTEM-SAED | Sensor | 60 |
| | — | 20–60 | XRD, TEM, TG-DTA | — | 61 |
| | Octahedral | 20–30 | XRD, FESEM, EDAX, TG–DTG | — | 62 |
| Pechini | — | 500 °C-30<br>700 °C-100 | XRD, TG-DTA, TEM-SAED | Catalytic combustion | 57 |
| Pechini & modified Pechini | — | 650 °C-200 | XRD, SEM | — | 58 |
| Sol–gel self-combustion | Tetragonal | 82.56 | XRD, FESEM, EDS, HRTEM-SAED, XPS, CIS | Electrical conductivity | 59 |
| Solution combustion self-combustion | Spherical | 200 and 225 | XRD, TGA-DTA, SEM, BET, XPS | Catalytic activity | 8 |
| Combustion | Irregular | 25.16 | UV-VIS-NIR, XRD, BET, SEM | — | 63 |
| | Spherical | $CuCr_2O_4$-35–40<br>$NiCuCr_2O_4$-38–46 | XRD, FTIR, BET, HRSEM, HRTEM, GC-MS | Polypropylene pyrolysis oil into diesel | 66 |
| | Spherical | 135.2 | XRD, FTIR, TEM, SEM, EDAX, TGA-DTA | Catalytic activity | 65 |
| Self-combustion | Spherical | — | XRD, UV-vis-DRS, FTIR, and SEM-EDX | Photocatalytic activity | 64 |
| Flow microreactor | — | 192–300 | XRD, FTIR, FESEM, $^1H$, $^{13}C$ NMR | — | 87 |
| Co-precipitation | Spherical | 20–30 | XRD, IR, SEM | Catalytic activity | 16 |
| | Spherical | 13.1 | SEM, TEM, DLLS | Catalytic activity | 69 |
| | Spherical | Uniform | XRD, FTIR, SEM, $^1H$, $^{13}C$ NMR | Catalytic activity | 67 |
| | Octahedral | — | XRD, SEM, TGA-DTA | Photocatalytic activity | 71 |
| | Spherical | 22–28 | XRD, FTIR, SEM, $^1H$, $^{13}C$ NMR | Catalytic activity | 68 |
| | Spherical and cubic | 26–30 | XRD, TEM, Raman spectroscopy, X-ray microanalyses | Catalytic activity | 92 |
| | Irregular | 20–30 | XRD, SEM, $^1H$ and $^{13}C$ NMR | Catalytic activity | 38 |
| | Quasi-spherical | 600 °C-15.1<br>700 °C-21.7 | XRD, TEM, BET | Photocatalytic activity | 23 |
| | Spherical | 48 | XRD, SEM, UV-vis, TG–DSC | Dye sensitized solar cells | 72 |
| Inverse-coprecipitation | Spherical | 520 °C-72 | XRD, FTIR, FESEM, TG–DSC | — | 70 |
| Hydrothermal | Almost uniform | 20–45 | XRD, XPS, ICP-AES, SEM, TEM, TGA | Catalytic activity | 15 |
| | Almost uniform (25–50 nm) | $CuCr_2O_4$ fresh-35, $CuCr_2O_4$ spent after five reuses-39 | XRD, ICP-AES, XPS, EXAFS, SEM, TEM, TGA | Catalytic activity | 74 |
| | Uniform | 20–60 | XRD, ICP-AES, XPS, FTIR, SEM, TEM, TGA | Catalytic activity | 75 |
| | Almost uniform (25–50 nm) | $CuCr_2O_4$ fresh-35, $CuCr_2O_4$ spent after five reuses-36 | XRD, XPS, SEM, TEM, TGA, ICP-AES | Catalytic activity | 35 |
| | Spherical | 20–40 | XRD, XPS, ICP-AES, SEM, TEM, TGA | Catalytic activity | 15 |
| | Irregular-500 °C<br>Cubic-600–800 °C | — | XRD, UV–vis-DRS, TEM, TG–DSC, XPS, zeta potential | Photocatalytic activity | 22 |
| | Uniform | 20 | XRD, FTIR, SEM, TEM | Supercapacitor | 47 |
| | Spherical | 12 | XRD, SEM, TEM | Catalytic activity | 79 |
| | Almost uniform | 30–60 | XRD, FTIR, SEM-EDAX, TEM, XPS | Catalytic activity | 76 |
| | Sphere | 23 | XRD, FTIR, SEM, EDS, $^1H$, $^{13}C$ NMR | Catalytic activity | 40 |
| | — | 7.9–23.9 | XRD, FTIR, SEM, TEM, TPR, TGA, BET | Catalytic activity | 77 |

**Table 1** *(Contd.)*

| Synthesis method | Morphology | Particle size (nm) | Characterization techniques | Applications | Ref. |
|---|---|---|---|---|---|
| | Uniform | 20–40 | XRD, ICP-AES, XPS, TPR, BET, SEM, TEM, EXAFS | Catalytic activity | 39 |
| | Uniform | $CuCr_2O_4$-35<br>$Mn_{0.5}Cu_{0.5}Cr_2O_4$-90 | XRD, FTIR, UV-Vis, FESEM, TGA | Photocatalytic activity | 80 |
| | Uniform | 20–50 | XRD, ICP-AES, FTIR, SEM, TEM, TGA, XPS | Catalytic activity | 78 |
| | — | 45 | XRD, TEM, SEM, EDAX | Catalytic activity | 93 |
| | 800 °C-spherical | 100–300 | XRD, SEM-EDX | Solar absorber coatings | 14 |
| | Irregular and spherical | $CuCr_2O_4$-30.17 | XRD, FT-IR, UV–Vis, FE-SEM, HR-TEM, BET | Photocatalytic activity | 81 |
| | | $CuCr_2O_4$–citric acid-26.38, $CuCr_2O_4$–tartaric acid-13.13 nm | | | |
| Mechanical ball milling | — | 30 | XRD, FTIR, SEM, TEM, BET, TGA/DSC | Catalytic activity | 84 |
| Ultrasonic dispersion method and a mechanical grinding | Spherical | — | XRD, FTIR, SEM, EDS, DSC–TG–DTG | Catalytic activity | 85 |
| Microwave assisted co-precipitation | Flower | 21–46 | XRD, UV-Vis, IR, FESEM, HRTEM | — | 18 |
| Microwave | Spherical | Citric acid-23, oleic acid-8.43<br>Coconut oil-9.62<br>Urea-15.48 | XRD, FTIR, SEM-EDS | — | 82 |
| | Hexagonal | 41–25 | UV-vis, XRD, FTIE, SEM, TEM | Dye-sensitized solar cell | 83 |
| Microwave combustion | Irregular plate | 37–26 | XRD, SEM | Antibacterial and electrical conductivity | 43 |
| Sputtering | — | 500 °C-30–40<br>800 °C-100 | XRD, SEM, AFM, TEM | — | 89 |
| Wet chemical grinding | Semi-spherical | 40 | XRD, SEM, TEM, DSC/TG | Catalytic activity | 90 |
| Co-precipitation, ultrasound, and green chemistry | — | 41.51 | XRD, FT-IR, EDX, SEM, zeta potential | Anti-breast cancer activity | 41 |

crystals. It is known for its simplicity, high yield, and controllability. Pakzad *et al.* synthesized $CuCr_2O_4$ pigment using a sol–gel combustion–calcination process. In this investigation, they employed Cu and Cr nitrate ions as oxidizers, using a mixture of fuels, such as glycine and citric acid, with low and high fuel ratios, respectively (eqn (1)).[17]

$$\begin{aligned} &9Cu(NO_3)_2 \cdot 3H_2O + 18Cr(NO_3)_3 \cdot 9H_2O \\ &\quad + 20C_6H_8O_7 \cdot H_2O + 2NH_2CH_2COOH + 9/O_2 \\ &\quad \rightarrow \mathbf{9CuCr_2O_4} + 37N_2 + 124CO_2 + 29H_2O \end{aligned} \quad (1)$$

Hosseini *et al.* produced $CuCr_2O_4$ NPs using a temperature-programmed procedure after a sol–gel method in the presence of urea, and the resulting particles were homogeneous, well-separated, and had a sphere-like morphology.[50] In another study, the researchers used sucrose as a template in the synthesis process and compared the template-assisted and template-free approaches.[51] Lachini *et al.* manufactured $CuCr_2O_4$ NPs using two different methods, sol–gel synthesis with stearic acid and green synthesis using *Aloe vera*. Researchers successfully investigated the performance of these materials as electrocatalysts in electrochemical hydrogen storage.[49] Benrighi *et al.* found that $CuCr_2O_4$ NPs have a spinel structure with an orthorhombic phase, specifically belonging to the *Fddd* space group.[52]

Peymanfar *et al.* investigated the microwave absorption properties of NPs produced using silicone rubber as a polymeric matrix. In the first study, they investigated a $CuCr_2O_4$/silicone rubber nanocomposite, which has a microwave absorption of 48.56 decibels (dB) at 10.9 GHz, a thickness of 2.6 mm, and more than 92.99% microwave absorption along the X-band frequency.[53] In the second investigation, they created $CuCr_2O_4$/poly(vinylidene fluoride) (PVDF) nanocomposites. They achieved a maximal reflection loss of −65.57 dB at 14 GHz with a thickness of 2 mm, and absorbed a bandwidth of 7.73 GHz with more than 10 dB absorption. $CuCr_2O_4$ NPs play a promising function in improving microwave absorption properties in polymeric matrices.[54] As discussed in a previous report, Akbar Mirzai and team synthesized $CuCr_2O_4$ NPs using glucose and created antibacterial films using PVDF and silicone rubber.[42]

Habibi *et al.* employed the citrate sol–gel synthesis method to synthesize $CuCr_2O_4$ NPs at room temperature using a fuel. The XRD data from the samples indicated the development of the $CuCr_2O_4$ nanocomposite at a calcination temperature of 700 °C.[55] Wang *et al.* synthesized nanochromates $MCr_2O_4$ (M = Co, Ni, Cu, and Zn) using the sol–gel technique. The structural and morphological traits were disclosed employing XRD and SEM.[56] The Pechini method involves dissolving Cu and Cr salts, and then adding citric acid to produce a homogeneous solution. This mixture was heated at 95 °C for many hours (h) to evaporate the water, yielding dark brown, clear, viscous gels. After that, the gel was dried at 160 °C for 2 h, resulting in frothy dark powders known as the precursor to $CuCr_2O_4$/CuO nanocomposites.[57] Additionally, Billman *et al.* manufactured $CuCr_2O_4$ NPs utilizing two nitrate–citrate combustion syn-

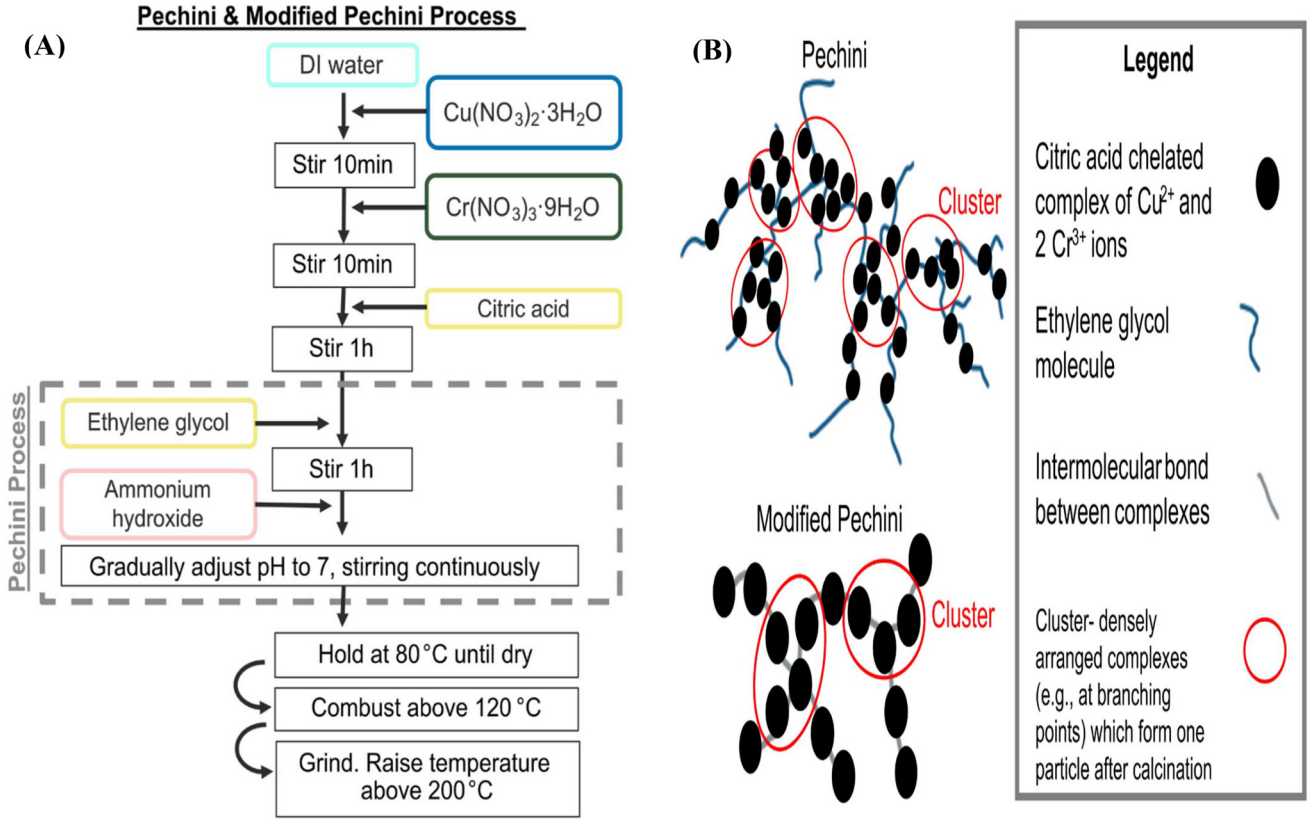


**Fig. 2** (A) Diagram of Pechini and modified Pechini method and (B) graphic showing the differences between the two methods for producing gel structures from chelated complexes.[58]

thesis sol–gel methods, as indicated in Fig. 2A, *i.e.*, one with ethylene glycol and neutralized with ammonium hydroxide (Pechini technique (Pechini, 1967)) and one without (modified Pechini method). The Pechini technique yields a broader particle size distribution, characterized by generally smaller and more scattered agglomerates, as shown in Fig. 2B, which exhibits a more branching structure with larger cluster sizes.[58]

Javed *et al.* conducted a detailed analysis of the physical characteristics of $CuCr_2O_4$ NPs. For the study of their structural attributes, a schematic representation was generated using the VESTA program (Fig. 3). $CuCr_2O_4$ NPs have a single-phase, tetragonally distorted normal spinel structure with an *I*41/*amd* space group in the crystal lattice. In the $CuO_4$ tetrahedral geometry, Cu(II) bonds have shorter lengths and angles compared to Cr(III) bonds in the $CrO_6$ octahedron. The TEM images revealed *d*-spacing values of 0.27310 nm. XPS analysis revealed the presence of several electrical routes in the $CuCr_2O_4$ spinel system, including $Cu^{2+}$–$O^{2-}$–$Cr^{2+}$, $Cr^{3+}$–$O^{2-}$–$Cr^{3+}$, $Cr^{6+}$–$O^{2-}$–$Cr^{6+}$, and $Cr^{3+}$–$O^{2-}$–$Cr^{6+}$.[59]

Kong *et al.* reported that the $CuCr_2O_4$ material has a pore structure that allows rapid analyte transport and generates well-dispersed, small-sized NPs with a minimal polyhedral content.[60] Cui *et al.* created various types of spinel NPs, including $CoAl_2O_4$ (blue), $CoCr_2O_4$ (bluish green), $ZnFe_2O_4$ (brown), and $CuCr_2O_4$ (black), employing propylene oxide as a gelation agent *via* the sol–gel technique, which reduces the required calcination temperature and minimizes particle agglomeration.[61] Habibi *et al.* investigated the decomposition mechanism of $Cu(NO_3)_2{\cdot}3H_2O$ and $Cr(NO_3)_3{\cdot}9H_2O$ precursors, as well as the copper chromite xerogel precursor, using thermal analysis. The results revealed that mass loss for copper(II) nitrate and chromium(III) nitrate occurred at 258 °C and 140 °C, respectively. In comparison, the major mass loss for the dried copper chromite gel occurred at 310 °C, confirming the decomposition of nitrates and the phase transformation leading to the complete crystallization of $CuCr_2O_4$.[62]

**2.1.2. Solution combustion method.** Studies found that the combustion reaction is an excellent chemical approach for synthesizing ceramic oxide spinels ($MCr_2O_4$). Compared to conventional methods, the solution combustion method enables the synthesis of $CuCr_2O_4$ NPs with smaller particle sizes and a larger surface area even before calcination.[8] Barros and colleagues successfully produced chromium spinel $MCr_2O_4$ (M = Zn, Co, Cu, and Ni) utilizing urea as fuel.[63] Paloma de Jesus Cubas and research team created $CuCr_2O_4$ NPs employing a self-combustion approach, which is a quick, easy, and effective technique. The synthesized NPs were analyzed, and the findings demonstrate their good purity, homogeneity, and excellent degrading capacity under visible

 

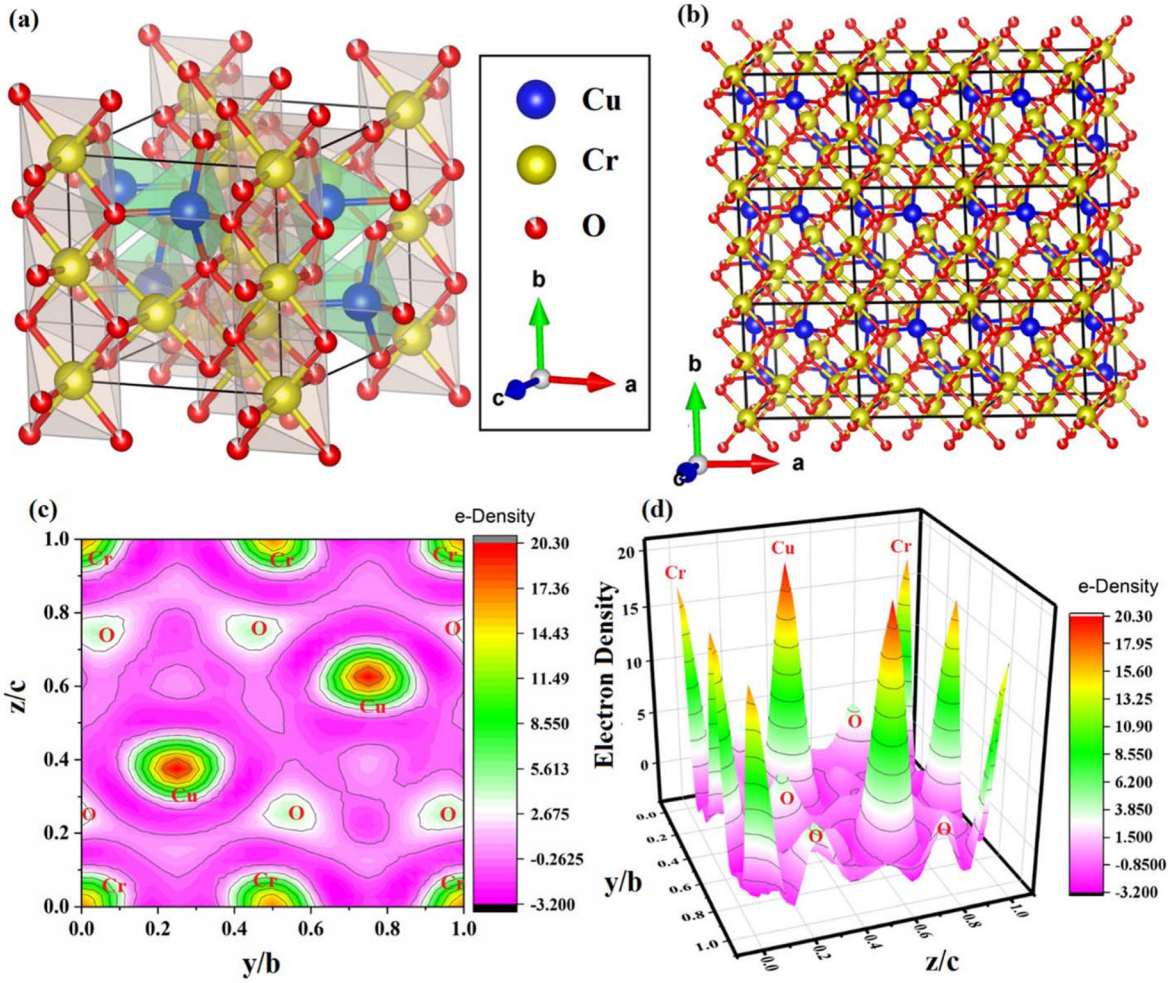


**Fig. 3** Schematic of the tetragonally distorted $CuCr_2O_4$: (a) unit cell, (b) extended crystal structure, and (c) 2D and (d) 3D electron density maps.[59]

light.[64] Surprisingly, Viswanath *et al.* synthesized an alginate mixed metal oxide complex. A sodium alginate solution was gradually mixed into a Cu and Cr nitrate solution, forming equal-sized beads. The generated beads were soaked for 24 h. After that, Cu and Cr ions were absorbed into the core of the alginate beads, resulting in a mixture of Cu and Cr alginate. After 24 h, the beads were filtered and vacuum-dried. Finally, the material was calcined at 750–800 °C for 3 h.[65] Tamizhdurai and research team synthesized undoped and doped Ni–$CuCr_2O_4$ NPs. They studied the hydro processing of polypropylene pyrolysis oil into diesel fuel.[66]

**2.1.3. Co-precipitation method.** In the co-precipitation approach, authors used sodium acetate (NAOAc) as the precipitating agent and adjusted the pH to 10. After the reaction mixture was maintained at 60 °C, it was heated to 80 °C, at which point precipitation began. Afterward, the sample was calcined, yielding 86% of synthesized $CuCr_2O_4$ NPs.[16,38,67–69] The inverse co-precipitation approach was used in the work by Tavakoli and Mamoory to create $CuCr_2O_4$ NPs at different calcination temperatures of 400 °C, 520 °C, and 800 °C. According to the XRD data, the sample calcined at 400 °C exhibited amorphous character. After being calcined for 2 h at 520 °C, pure-phase $CuCr_2O_4$ was produced. The enhanced crystallinity of the NPs was demonstrated by a gradual rise in the intensity of all the diffraction peaks and the narrowing of the peak widths at 800 °C.[70]

Pan *et al.* described the synthesis process of $CuCr_2O_4$ NPs. They used the appropriate mixed amount of $Cu(NO_3)_2{\cdot}3H_2O$ and $CrCl_3{\cdot}6H_2O$, along with $(CH_2)_6N_4$ and $NH_4HCO_3$, and then agitated for 1 h. After aging the mixture for 12 h, the samples were dried in a vacuum at 105 °C for 6 h, and the dry precursor was obtained. After that, the precursor was calcined at 400 °C, 450 °C, 500 °C, and 600 °C for 3 h each.[71] A mono-dispersed $CuCr_2O_4$ nanopowder was effectively generated using an alcohol–aqueous mixture and applied as photoanodes in dye-sensitized solar cells.[72]

Paul *et al.* manufactured $CuCr_2O_4$ NPs utilizing a co-precipitation method with a 1 : 2 molar ratio of Cu and Cr hydroxide precursors. Initially, urea decomposed to $NH_3$ and $CO_2$ (eqn (2)). $NH_3$ reacts with water molecules to form $NH_4^+$ and $OH^-$ (eqn (3)). The free $OH^-$ ions subsequently mix with $Cu^{2+}$ and $Cr^{3+}$ ions to form $Cu(OH)_2$ and $Cr(OH)_3$ (eqn (4) and (5)),

respectively. The sample was calcined to produce $CuCr_2O_4$ NPs (eqn (6)).[23]

$$(NH_2)_2CO + H_2O \rightarrow 2NH_3 + CO_2 \quad (2)$$

$$NH_3 + H_2O \rightarrow NH_4^+ + OH^- \quad (3)$$

$$Cu^{2+} + 2OH^- \rightarrow Cu(OH)_2 \quad (4)$$

$$Cr^{3+} + 3OH^- \rightarrow Cr(OH)_3 \quad (5)$$

$$Cu(OH)_2 + 2Cr(OH)_3 \xrightarrow{\Delta} \mathbf{CuCr_2O_4} + 4H_2O \quad (6)$$

**2.1.4. Hydrothermal method.** The hydrothermal technique crystallizes materials by heating water at high pressure to produce high-quality, composition-controlled crystals. To allow the quick passage of metal ions, the phases that dissolve at their melting points are provided with a homogeneous composition and stability.[73] Cu–Cr samples were manufactured utilizing a non-hydrothermal technique, although the particles were not homogeneous. According to a study by Acharyya *et al.*, autogenous pressure during hydrothermal conditions was required to form homogeneous $CuCr_2O_4$ NPs.[74] The energy required to form a new phase from the precursor ions is reduced when the surfactant lowers the surface tension. Various studies on $CuCr_2O_4$ NPs by Acharyya and colleagues have successfully fabricated $CuCr_2O_4$ NPs using cetyltrimethylammonium bromide (CTAB), a cationic surfactant,[35,39,75–78] and cetyl alcohol.[15] Yuan *et al.* reported that cubic-like $CuCr_2O_4$ particles can be achieved using the hydrothermal approach.[22]

Ismael *et al.* produced $CuCr_2O_4$ NPs *via* a hydrothermal method. Fig. 4 shows how colloidal $CuCr_2O_4$ was re-dispersed in acetone after being recovered from its production medium using an ultrasonic probe. Ammonium perchlorate (AP) particles, followed by dissolution in acetone and colloidal $CuCr_2O_4$ NPs, were integrated into the AP matrix using the antisolvent method.[79]

Soleimani *et al.* prepared $CuCr_2O_4$ and $Mn_{0.5}Cu_{0.5}Cr_2O_4$ and compared their effectiveness in degrading malachite green with $CuCr_2O_4$ NPs.[80] Pleasingly, Acharyya *et al.* reported the 3D raspberry-like morphology of $CuCr_2O_4$ in one of their studies. Crystal-face attraction, electrostatic fields, van der Waals forces, hydrophobic interactions, hydrogen bonds, and the autogenous pressure in the autoclave influence the creation of the raspberry morphology. The "soft template" CTAB and Ostwald ripening also have a substantial contribution. $Cr^{6+}$ precursors, such as $K_2Cr_2O_7$, play a significant role in forming the raspberry-like structure, but $Cr^{3+}$ precursors, including $CrCl_3$ and $Cr(NO_3)_3{\cdot}9H_2O$, do not. Synthesizing chromium(III) oxide with CTAB, $(NH_4)_2Cr_2O_7$, and hydrazine resulted in a characteristic 3D strawberry-like texture, underlining the significance of $Cr^{6+}$ in self-assembly (Fig. 5).[78]

Rubin *et al.* hydrothermally synthesized $CuFeMnO_4$ and $CuCr_2O_4$ NPs, whereas large-batch sintering produced $Cu_{0.5}Cr_{1.1}Mn_{1.4}O_4$. These samples were annealed at 800 °C for

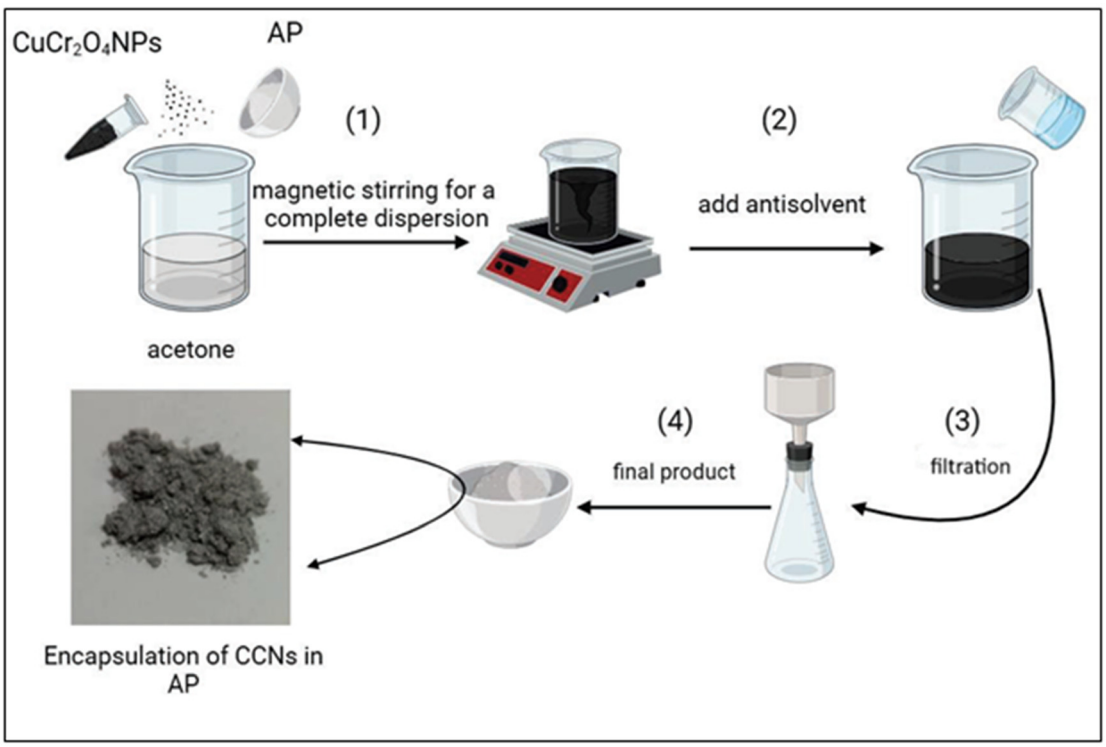


Fig. 4 Integration of $CuCr_2O_4$ NPs into AP.[79]

 

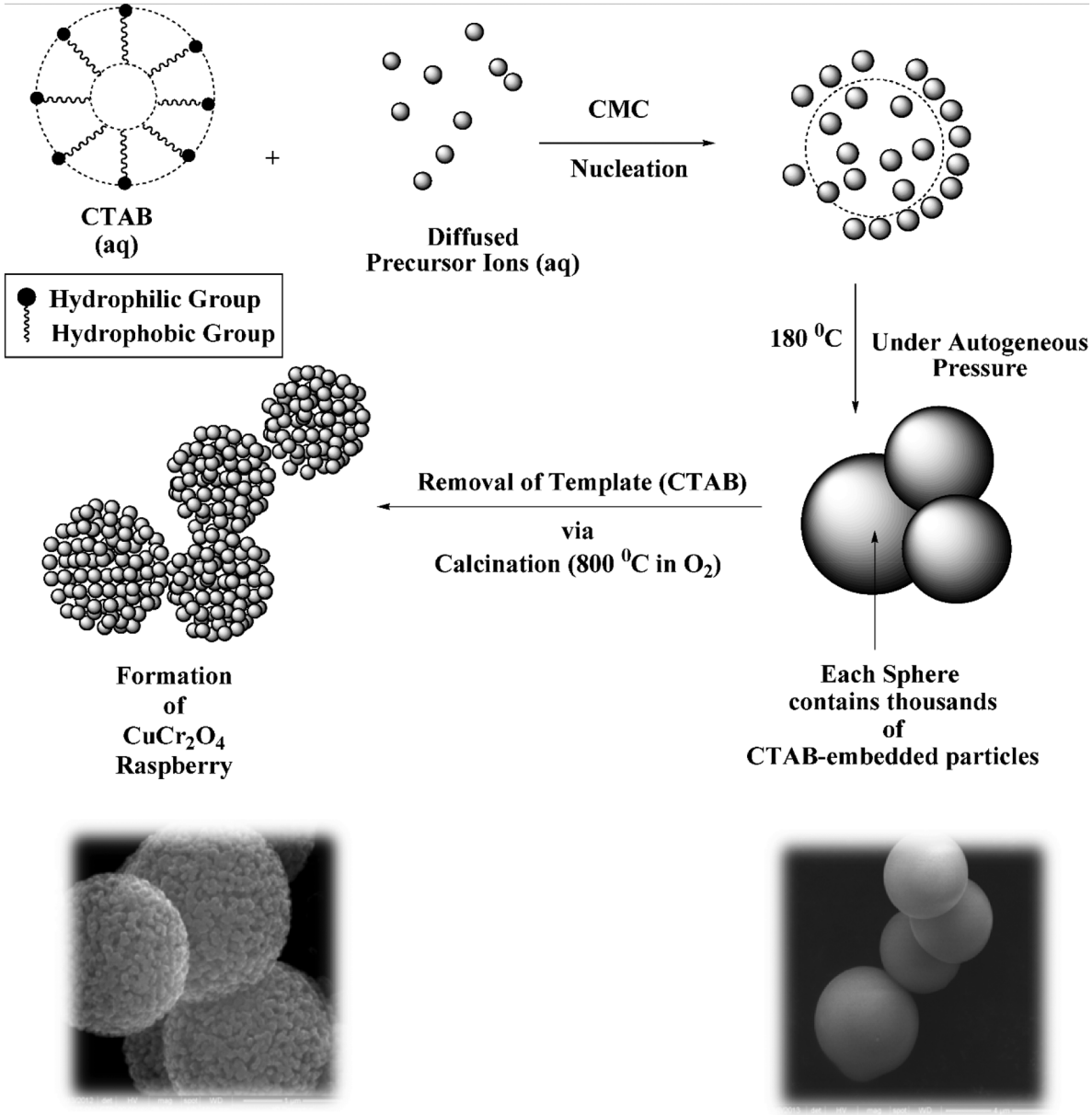


Fig. 5 Schematic of the production of $CuCr_2O_4$ spinel catalyst with a 3D raspberry-like structure.[78]

various durations, including 100, 300, 1000, and 2000 h. After 2000 h, XRD data verified that the relevant peaks are indeed that of $CuCr_2O_4$, and there is no reason to assume a phase transition from $CuCr_2O_4$ to $CuCrO_2$ (delafossite).[14] Al-Wasidi *et al.* demonstrated the facile synthesis of $CuCr_2O_4$ NPs using citric acid and tartaric acid templates, as well as in their absence.[81]

**2.1.5. Microwave-assisted method.** Innovation has made preparation easier using microwave radiation for homogeneous heating. Monika *et al.* manufactured nanocomposites of $Cr_2O_3$ incorporated with CuO using microwave-assisted co-precipitation. They used NaOH (precipitating agent) and annealed it at 600 °C before pouring 10% chromium oxide and igniting at 200 °C, 400 °C, and 600 °C.[18] The SEM images of the samples synthesized by microwave energy in a 1 min on-off cycle at 600 W with different capping agents revealed a pyramidal morphology that transformed into a spherical or pseudo-spherical shape as a result of clustering, with inadequate homogeneity due to the large variety of particle sizes.[82] Rajeswari *et al.* produced pristine $CuCr_2O_4$ (0.00) and La-doped $CuCr_2O_4$ (0.01–0.03) using a microwave oven at 2450 MHz.[83] Additionally, pristine $CuCr_2O_4$ and La-doped $CuCr_2O_4$ were synthesized by Sankudevan *et al.*[43]

**2.1.6. Mechanical ball-milling method.** Gou *et al.* synthesized raw $CuCr_2O_4$ and nano-$CuCr_2O_4$ using mechanical grinding.[19] The $CuCr_2O_4$ suspension was prepared using a ball milling process with a mixture of water and ethanol. The suspension was then ground in a 01-HDDM machine at 1200

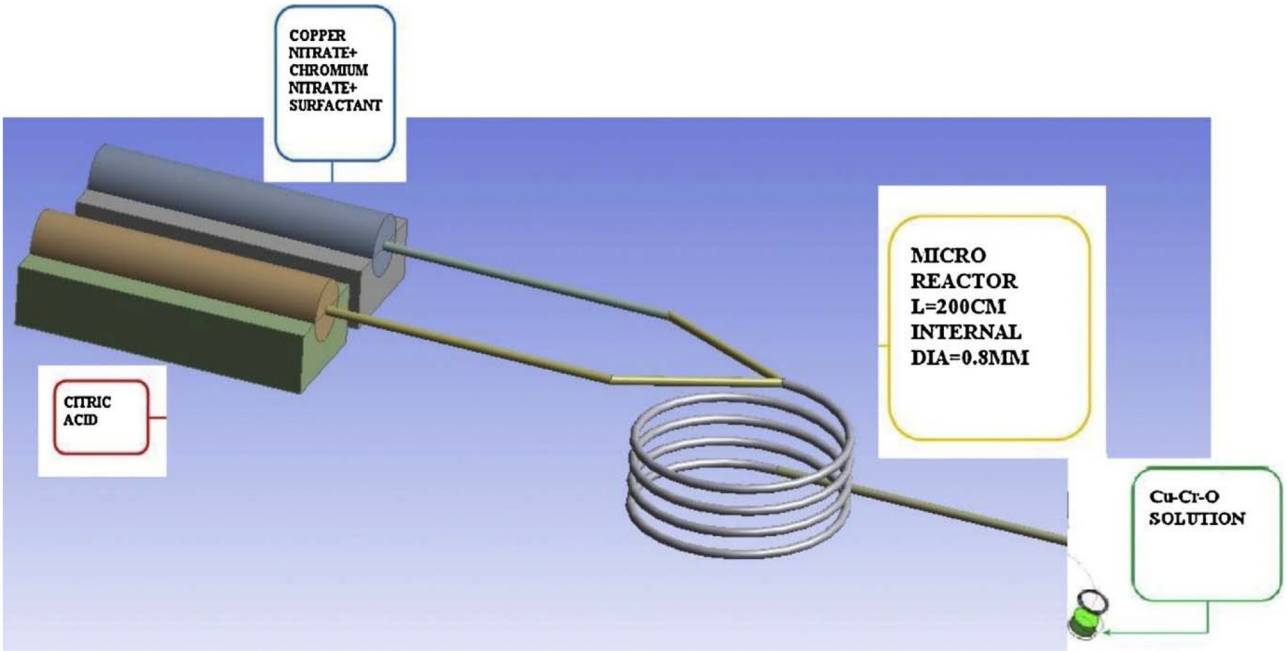


Fig. 6 Illustration of the fabrication of $CuCr_2O_4$ NPs in a continuous flow microchannel reactor.[87]

rpm for 3 h, maintaining the temperature between 20–30 °C. Finally, the slurry was transferred to a vacuum dryer to obtain nano-$CuCr_2O_4$.[84] Nano-$CuCr_2O_4$/ultrafine AP composites were prepared using an ultrasonic dispersion and mechanical ball milling approach by Zhang *et al.*, and varying ball milling periods (30 min, 1, 3, 6, 12, 24, and 48 h) created different dispersions. The researchers examined both methods and determined that nano-$CuCr_2O_4$ exhibits a better dispersion in ultrafine AP composites made by mechanical ball milling. The dispersion of nano-$CuCr_2O_4$ on ultrafine AP is improved with longer milling times. The most consistent dispersion of nano-$CuCr_2O_4$ occurs in ultrafine AP after 6–12 h of milling.[85]

**2.1.7. Other methods.** Han *et al.* employed the polyacrylamide gel method to synthesize $CuAl_2O_4$ in the cubic phase, whereas $CuCr_2O_4$ and $CuFe_2O_4$ were synthesized in the tetragonal phase. $CuAl_2O_4$ was produced without impurities, but $CuCr_2O_4$ and $CuFe_2O_4$ included CuO impurities. $CuAl_2O_4$ showed superior photocatalytic activity to the other spinel NPs due to its smaller particle size.[86]

Appalakutti *et al.* fabricated Cu–Cr–O nanocomposites using a continuous flow microreactor. As depicted in Fig. 6, Cu, Cr nitrate, and surfactant (PVP and CTAB) mixtures were filled in a syringe at varying molar ratios. Alternatively, another syringe was filled with a citric acid solution in a 2 : 1 molar ratio relative to the total metal ion concentration. The microreactor was placed in a water bath at 80 °C, with a flow rate ranging from 25 to 150 mL $h^{-1}$. After that, the nanopowder was generated by calcining at 200 °C for a specific period of 2 h. The hydrolysis and polycondensation reaction (eqn (7)–(10)) mechanisms are provided below.[87]

**Hydrolysis reaction**

$$\begin{aligned}
&Cu(NO_3)_2 \rightarrow Cu^{2+} + 2NO_3{}^- \\
&Cr(NO_3)_2 \rightarrow Cr^{3+} + 3NO_3{}^- \quad \text{citric acid} = CA \\
&Cu^{2+} + CA \rightarrow [Cu(CA)]^{2+} \\
&H_2O \rightarrow H^+ + OH^- \\
&2Cr^{3+} + [Cu(CA)]^{2+} + 6OH^- + 2NO_3{}^- \\
&\quad \rightarrow [Cr_2Cu(CA)(OH)_6](NO_3)_2
\end{aligned} \tag{7}$$

(Precursor A)

$$\begin{aligned}
&Cr^{3+} + 3OH^- \rightarrow Cr(OH)_3 \\
&Cr^{3+} + Cr(OH)_3 + Cu^{2+} + 5OH^- + 4H_2O \\
&\quad \rightarrow [Cr_2Cu(OH)_8] \cdot 4H_2O
\end{aligned} \tag{8}$$

(Precursor B)

$$14H^+ + 14NO_3{}^- \rightarrow 14HNO_3$$

**Polycondensation by dehydration**
(Precursor A)

$$\begin{aligned}
&[Cr_2Cu(CA)(OH)_6](NO_3)_2 \\
&\quad \rightarrow [Cr_2Cu(OH)_6](NO_3)_2 + CA \\
&[Cr_2Cu(OH)_6](NO_3)_2 \rightarrow Cr_2CuO(OH)_6 \\
&\quad \rightarrow Cr_2O_2(OH)_2 \cdot CuO + 2H_2O \\
&Cr_2O_2(OH)_2 \cdot CuO \rightarrow Cr_2O_3 \cdot CuO + H_2O \\
&Cr_2O_3 \cdot CuO \rightarrow \mathbf{CuCr_2O_4}\ (\mathbf{black\ spinel})
\end{aligned} \tag{9}$$

(Precursor B)

$$\begin{aligned}
&[Cr_2Cu(OH)]_8 \cdot 4H_2O \rightarrow Cr_2Cu(OH)_8 + 4H_2O \\
&Cr_2Cu(OH)_8 \rightarrow Cr_2O_2(OH)_2CuO + 3H_2O \\
&Cr_2O_2(OH)_2CuO \rightarrow Cr_2O_3 \cdot CuO + H_2O \\
&Cr_2O_3 \cdot CuO \rightarrow \mathbf{CuCr_2O_4}\ (\textit{b}\mathbf{lack\ spinel})
\end{aligned} \tag{10}$$

Interestingly, Chiu and research team used an electrospinning approach to produce 1-D $CuCr_2O_4$ fibers.[88] Tsai and colleagues successfully examined the production of transparent conducting Cu–Cr–O films on fused silica substrates utilizing DC reactive magnetron sputtering with a single equimolar Cu–Cr alloy target and a post-annealing method in a controlled Ar atmosphere at 500–800 °C for 2 h.[89]

The wet mechanical grinding method and the vacuum freeze-drying process present a promising technique for easily producing Cu-based NPs, which have potential applications in the mass preparation of other nanosized catalysts. The Cu-based NPs, including CuO, $CuCr_2O_4$, and copper β-resorcylate, are illustrated in Fig. 7a and b, which detail the synthesis and drying processes, respectively.[90]

Ahmed *et al.* produced $CuCr_2O_4$ using rosemary (*Rosmarinus officinalis*) leaf extract, employing three techniques including co-precipitation, ultrasonication, and green chemistry. Researchers evaluated its anti-breast cancer efficacy using the MCF-7 cell line, which revealed encouraging results.[41] The $CuCrO_2$ phase develops at a temperature of 750–800 °C for all five mixes. CuO, $Cr_2O_3$, and $CuCr_2O_4$ phases exist in this temperature range; hence, the $CuCrO_2$ phase is produced by reacting the spinel phase with CuO.[91]

In conclusion, various physical, chemical, and green synthesis methods have been employed to fabricate $CuCr_2O_4$ nanomaterials. Among them, the sol–gel method is the most widely used due to its low calcination temperature, excellent chemical homogeneity, and ability to produce monodispersed NPs with a controlled size and morphology. The citric acid-assisted sol–gel technique is particularly effective, given that citric acid functions as a chelating agent, forming homo-

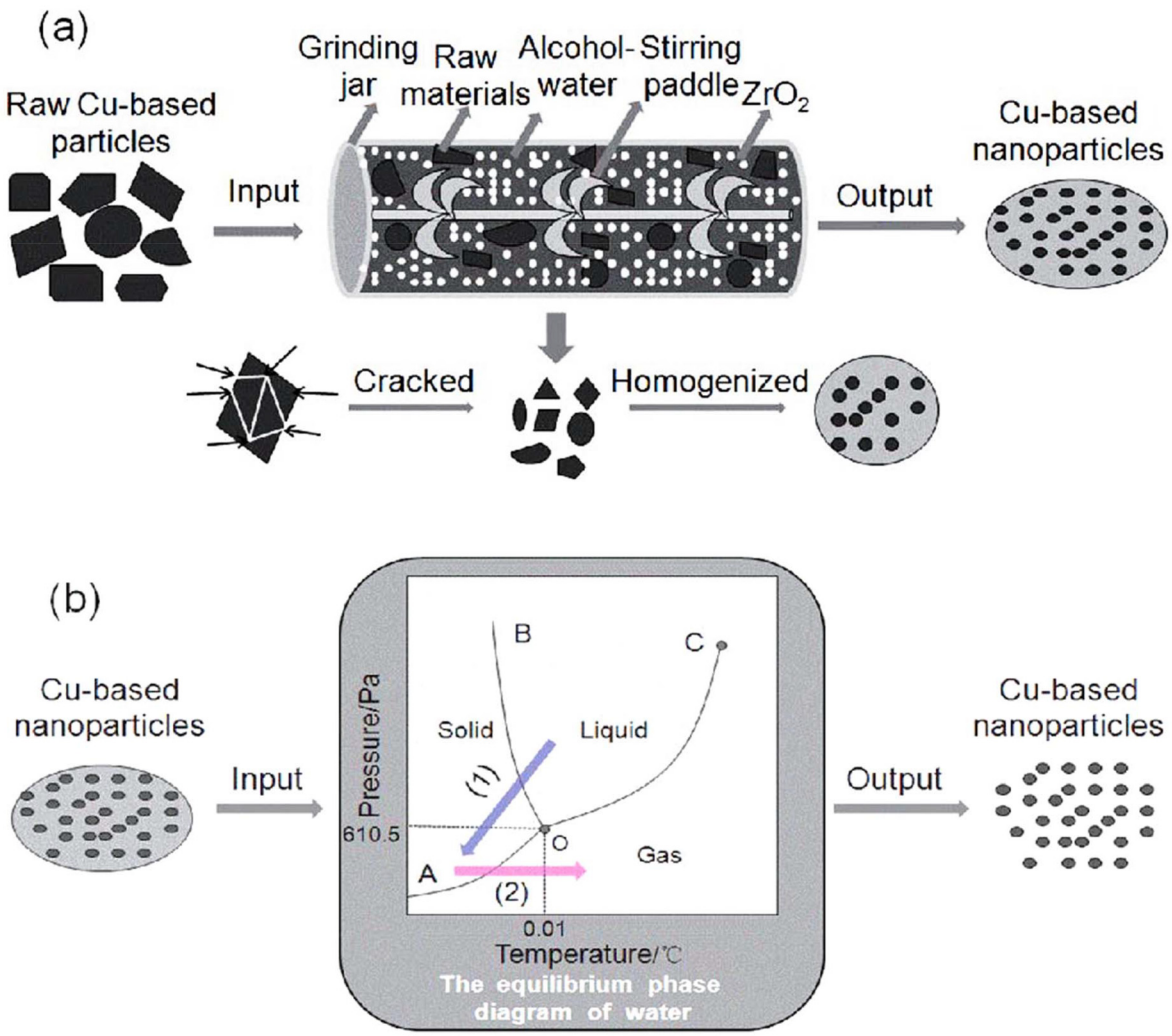


**Fig. 7** Diagram of the production of Cu-based NPs: (a) vacuum freeze-drying and (b) wet mechanical grinding.[90]

geneous metal–citrate gels that promote the uniform mixing of metal ions and result in smaller crystallite sizes. According to the literature, this method typically yields nanoparticles with small sizes and spherical morphology, which enhance their surface area and improves their catalytic performance. The improved homogeneity of $CuCr_2O_4$ synthesized *via* this approach significantly boosts its photocatalytic activity, especially in the degradation of antibiotics, making it more advantageous than conventional synthesis techniques. Additionally, the sol–gel approach facilitates the incorporation of capping agents, such as amino acids, and green alternatives, such as sucrose. These stabilizing agents effectively minimize the agglomeration, enhance the crystallinity, and refine the morphology of the particles. Therefore, the sol–gel method, when combined with suitable chelating and capping agents, provides a versatile, efficient, and environmentally friendly approach for synthesizing high-performance $CuCr_2O_4$ nanostructures for various applications.

### 2.2. Synthesis of metal-doped $CuCr_2O_4$ NPs

Batool *et al.* manufactured Cd- and Nd-doped $CuCr_2O_4$ NPs ($M_xCu_{1-x}Cr_2O_4$) with $x$ values of 0.2, 0.4, 0.6, and 0.8. The band gap of the parent compound was ascertained employing photoluminescence (PL) spectra and found to be 4.96 eV. When elements were doped in the parent compound at varying concentrations, the band gap ($E_g$) decreased for Nd (2.43 eV) and Cd (2.42 eV). Additionally, microscopic images revealed that the texture of pure $CuCr_2O_4$ NPs was tetragonal and that doping with other compounds alters the structure according to the characteristics of the NPs.[94] Anusree *et al.* produced Ba and Co-doped $CuCr_2O_4$ NPs using a hydrothermal technique and evaluated the catalytic efficacy of the created NPs for the heat breakdown of AP.[95] These studies, conducted by Acharyya *et al.*, reported the formation of nanoclusters of Cu(II) supported by $CuCr_2O_4$ NPs. They investigated their catalytic activity in the selective hydroxylation of benzene to phenol,[24] the oxyamination of benzene to aniline,[96] and the selective oxidation of ethanol.[97]

Bai *et al.* reported the synthesis of Fe and Mn-doped $CuCr_2O_4$ NPs with the formula $CuCr_{2-x-y}Fe_xMn_yO_4$. The doped pigments exhibited a higher UV-visible absorbance than $CuCr_2O_4$, attributed to electron transfer between $O^{2-} \rightarrow Fe^{3+}$, $O^{2-} \rightarrow Mn^{3+}$, and d–d intra-atomic transitions of $Fe^{3+}$ and $Mn^{3+}$. The $CuCr_{1.93}Fe_{0.07}O_4$ black pigment showed a higher NIR solar reflectance ($R^*$ = 27.7%) than the $CuCr_2O_4$ black pigment ($R^*$ = 19.0%), which was ascribed to the decreased concentration of free carriers.[98]

Yadagiri *et al.* employed the sol–gel method for generating $CuCr_2O_4$ and Fe-substituted $CuCr_2O_4$. XRD analysis of $CuCr_{2-x}Fe_xO_4$ revealed that for $x$ = 0.0, the phase is tetragonal, whereas the other three compounds ($x$ = 0.5, 1.0, and 1.5) have a cubic phase. It was discovered that the average crystalline size increased with Fe substitution.[99] Ramezanalizadeh *et al.* created La-doped $CuCr_2O_4$ NPs. The photocatalytic study of doped NPs revealed the outstanding degradation of contaminated dyes.[100] Jagadeesan *et al.* synthesized pure $CuCr_2O_4$ and doped $CuCr_{2-x}Mg_xO_4$ ($x$ = 0.00–0.1%, 0.2%, and 0.3%) nanocomposites. In short, the Mg-doped sample has a higher specific surface area than the pure $CuCr_2O_4$ sample.[101] Interestingly, Zn-doped $CuCr_2O_4$ was synthesized at different concentrations and calcined at various temperatures.[102] Interestingly, scientists utilized $CuCr_2O_4$ black oxide pigment doped with various metals, including Mn, Ni, Co, Al, Zn, and Sn, to create solar-absorbing spinel structures. Among them, the Mn–$CuCr_2O_4$ pigment exhibited much higher levels of solar absorption than the other metal dopants.[103]

Using a microscopic model and Green's function theory, Apostolov *et al.* theoretically investigated the magnetic, electric, and optical characteristics of both pure and ion-doped $CuCr_2O_4$ in bulk and nanoparticle forms. Their results showed that the magnetization and band gap energy ($E_g$) decrease with an increase in the nanoparticle size. Magnetization and polarization ($P$) peaked when doped with Co ions, while both qualities decreased as the Pr ion concentration increased. Therefore, compared to that substituted with rare-earth elements, Co-doped $CuCr_2O_4$ NPs are more appropriate for spintronic applications. Alternatively, Pr ion doping raises the $E_g$, which makes it more suitable for solar cell technology.[104]

Table 2 summarizes the diverse synthetic approaches, characterization techniques, and applications of metal-doped $CuCr_2O_4$ NPs.

### 2.3. Synthesis of $CuCr_2O_4$ nanocomposites

The interaction of NPs with the matrix and particle–particle interactions are important variables in determining the properties of nanocomposites. Strong interactions between particles and epoxy can enhance the mechanical properties of nanocomposites.[106–108] Lao *et al.* created $CuCr_2O_4$ NPs using the sol–gel technique. Then, a suspension was created by diluting the $CuCr_2O_4$ sample with glucose. $Ag(NH_3)_2OH$ was created by titrating a 0.01 mol $L^{-1}$ $AgNO_3$ solution from a diluted $NH_3{\cdot}H_2O$ solution. They combined the suspension with the Ag solution. Then, the mixture was centrifuged and dried, yielding a final weight ratio of $CuCr_2O_4$ : Ag of 9 : 1. The SEM investigation revealed that the surfaces of the NPs were shiny and smooth. Following electroless plating with Ag, nanosized particles were found to be equally dispersed on the surface of $CuCr_2O_4$, indicating that Ag was efficiently coated onto the $CuCr_2O_4$ surface.[46] Kien and colleagues used the sol–gel and impregnation methods to produce $CuCr_2O_4{\cdot}Pd/\gamma\text{-}Al_2O_3$.[109] As previously described in their studies, they first synthesised $Bi_2O_3$.[110] Subsequently, the complexing-coprecipitation method was employed to synthesise $CuCr_2O_4$–CuO. As depicted in Fig. 8, electrostatic interaction between $NH_4^+$ and $Bi_2O_3$ NPs resulted in the coating of $NH_4^+$ on $Bi_2O_3$ surfaces because of their higher specific surface area and plentiful $OH^-$. $Cu^{2+}$ and $Cr^{3+}$ salts were then deposited on the $Bi_2O_3$ surfaces. $NH_4^+$ on $Bi_2O_3$ particles exhibits a strong complexing interaction with $Cu^{2+}$, and it may be absorbed on the surface of $Bi_2O_3$, forming $[Cu(NH_3)_4]^{2+}$. Similarly, $Cr^{3+}$ can be coated on the surface of $Bi_2O_3$ particles through electrostatic interaction between $[Cu(NH_3)_4]^{2+}$ and $[Cr(OH)_4]^-$. After calcination,

 

**Table 2** Summary of the synthesis method, characterization techniques, morphology, and applications of metal-doped $CuCr_2O_4$ NPs

| Doped nanoparticles | Synthesis method | Morphology | Particle size (nm) | Characterization techniques | Applications | Ref. |
|---|---|---|---|---|---|---|
| $CuCr_2O_4$ | Sol–gel | Spherical | >100 | XRD, EDS, SEM, PL, Raman spectroscopy | — | 94 |
| $Cu_{1-x}Cd_xCr_2O_4$ and $Cu_{1-x}Nd_xCr_2O_4$ | | — | 25–55 | | | |
| Ba and Co doped $CuCr_2O_4$ | Hydrothermal | Irregular | $CuCr_2O_4$-42 $CoCuCr_2O_4$-52 $BaCuCr_2O_4$-32 | XRD, SEM, TEM, BET | Catalytic activity | 95 |
| Cu(II) oxide $CuCr_2O_4$ NPs | Hydrothermal | — | 2–8 ~55 | XRD, SEM, TEM, XPS, FTIR, TGA, TPR, BET, XANES, ICP-AES | Catalytic activity | 24 |
| Cu(II) supported $CuCr_2O_4$ | — | — | ~10 30–60 | XRD, XPS, SEM, TEM, TPR, TGA | Catalytic activity | 96 |
| Cu(II)-supported $CuCr_2O_4$ | Hydrothermal | — | 30–60 | XRD, BET, ICP-AES, SEM, TEM, TGA | Catalytic activity | 97 |
| Fe/Mn co-doped $CuCr_2O_4$ | Co-precipitation | Octahedron | — | XRD, UV-vis-NIR, XPS, SEM, Raman spectroscopy | — | 98 |
| $CuCr_2O_4$ and Fe-substituted $CuCr_2O_4$ | Sol–gel | Rectangular | — | XRD, UV-vis, Mossbauer, Raman spectroscopy, FESEM | — | 99 |
| La–$CuCr_2O_4$ | Sol–gel Pechini | Spherical | — | XRD, SEM, FTIR, DRS, VSM | Photocatalytic activity | 100 |
| $CuCr_2O_4$ | Combustion | Irregular | 49–53 | XRD, FTIR, FESEM, TEM, BET | Catalytic activity | 101 |
| Mg (0.1%) $CuCr_2O_4$ | | | 43–39 | | | |
| Mg (0.2%) $CuCr_2O_4$ | | | 40–31 | | | |
| Mg (0.3%) $CuCr_2O_4$ | | | 39–29 | | | |
| $CuCr_2O_4$ | Hydrothermal and co-precipitation | Octahedral | 71.84 | XRD, UV–vis–NIR, SEM | Solar power | 103 |
| $CuCrMnO_4$ | | Octahedral | 38.07 | | | |
| $CuCrNiO_4$ | | Flake | 51.88 | | | |
| $CuCrCoO_4$ | | Flake | 33.71 | | | |
| $CuCrAlO_4$ | | Irregular rods and polyhedral | 31.64 | | | |
| $CuCrZnO_4$ | | Flake | 38.41 | | | |
| $CuCrSnO_4$ | | Octahedral | 86.36 | | | |
| $ZnCuCr_2O_4$ | Sol–gel | — | — | XRD, SEM-EDS UV, PL, Raman spectroscopy | — | 102 |
| $Cu_{1-x}Mg_xCr_2O_4$ | Sol–gel | Quasi spherical | — | XRD, UV, SEM | — | 105 |

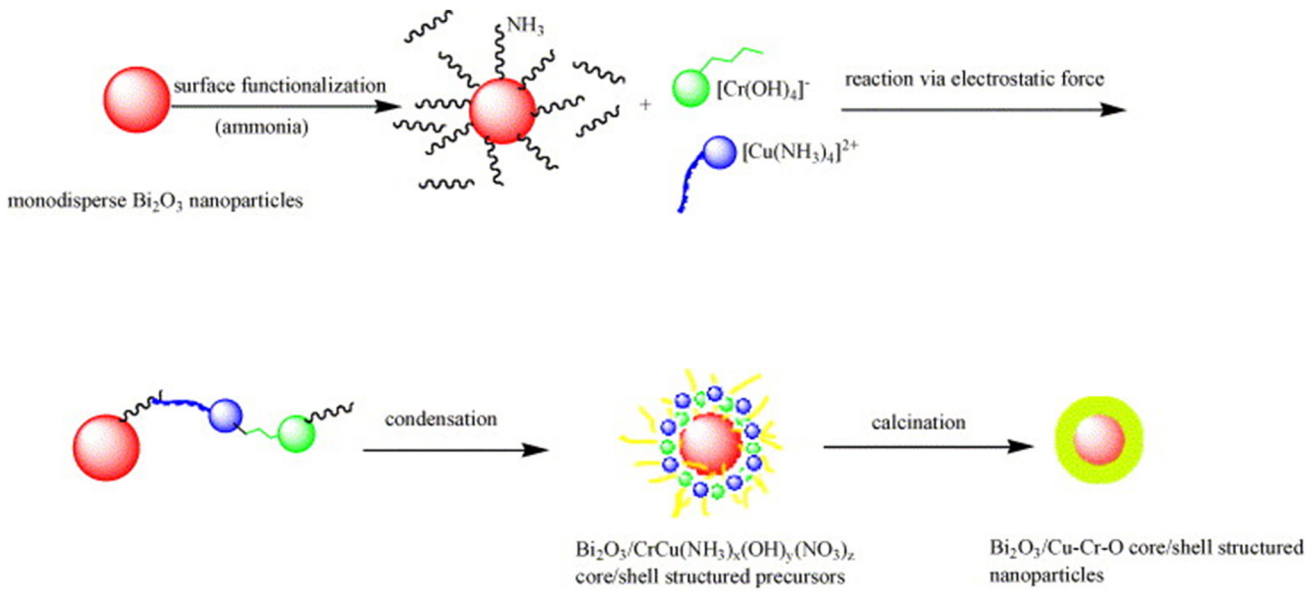


**Fig. 8** Schematic of the spherical $Bi_2O_3/CuCr_2O_4$–CuO core/shell NCs.[111]

monodisperse spherical $Bi_2O_3/CuCr_2O_4$–CuO core/shell nanocomposites were produced.[111]

Balasurya *et al.* synthesized NCs using the co-precipitation method to synthesize $CuCr_2O_4$ NPs. Using these NPs and Bi salt, they synthesized $CuCr_2O_4$–$BiI_3O_9$ nanocomposites *via* a sonochemical method.[45] Ghorai and co-workers described $CuCr_2O_4$/BiOBr NC. Sol–gel combustion produces spherical $CuCr_2O_4$ NPs, which are then decorated on BiOBr plates using precipitation. CTAB was used as the Br source and template (Fig. 9).[112]

A $CuCr_2O_4$@CaFe–LDO hybrid was synthesized by Oladipo and group. They investigated its photocatalytic potential for treating olive mill effluent (OMW). These nanocomposites demonstrated outstanding absorption and photocatalytic activity.[113,114] The researchers synthesized various nanocomposites, including $CuCr_2O_4$–$CeO_2$, using the sol–gel and co-precipitation methods, as well as a combination of these techniques.[115] Additionally, they employed the impregnation method,[116] reflux condensation,[26] and ultrasonication-assisted methods[117] to synthesize Cu/$CuCr_2O_4$, CuO–$CuCr_2O_4$, and mesoporous $CuCr_2O_4$–g-$C_3N_4$ heterojunctions, respectively.

Hummers' approach was adapted to produce graphene oxide.[118] Graphene nanocomposites with electron-donating inclusions increase the electronic significance of the molecules they support.[119–121] g-$C_3N_4$–NS/$CuCr_2O_4$ using refluxing,[119] $CuCr_2O_4$/GO using co-precipitation,[120] MXene ($Ti_3C_2T_x$)/$CuCr_2O_4$ used wet-chemical sonication-assisted co-precipitation approach,[122] nanospherical–$CuCr_2O_4$ nanocomposite decorated with polyaniline (PANI),[123] heterogeneous p-$CuCr_2O_4$/n-$SnO_2$,[124] and $MCr_2O_4/TiO_2$ (M–Cu, Ni) using the co-precipitation method.[125]

Gao *et al.* employed a high-temperature phase separation technique to synthesize $CuCr_2O_4/Cr_2O_3$ nanogranular from Cu-doped $Cr_2O_3$ NPs, as confirmed by XRD tests. Its magnetic susceptibility has two transitions, *i.e.*, $CuCr_2O_4$ becomes ferrimagnetic at 130 K, and $Cr_2O_3$ becomes antiferromagnetic at 310 K.[126]

Mechanical milling is a viable solid-state method for creating new $CuCrO_2/CuCr_2O_4$ nanocomposites. This approach affects both the outcome of the reaction product and the phase transitions that occur during the process. This research compares the heat treatment and characteristics of the nanocomposite to that of single-phase delafossite.[127]

As depicted in the reaction pathway in Fig. 10, firstly $CuCr_2O_4$ NPs were fabricated *via* a sol–gel auto-combustion approach. Then, calcined NPs were dispersed in epoxy resin and polyurethane (PU) using ultrasonication to synthesize EP/PU/$CuCr_2O_4$ nanocomposites. By adding $CuCr_2O_4$ NPs to the

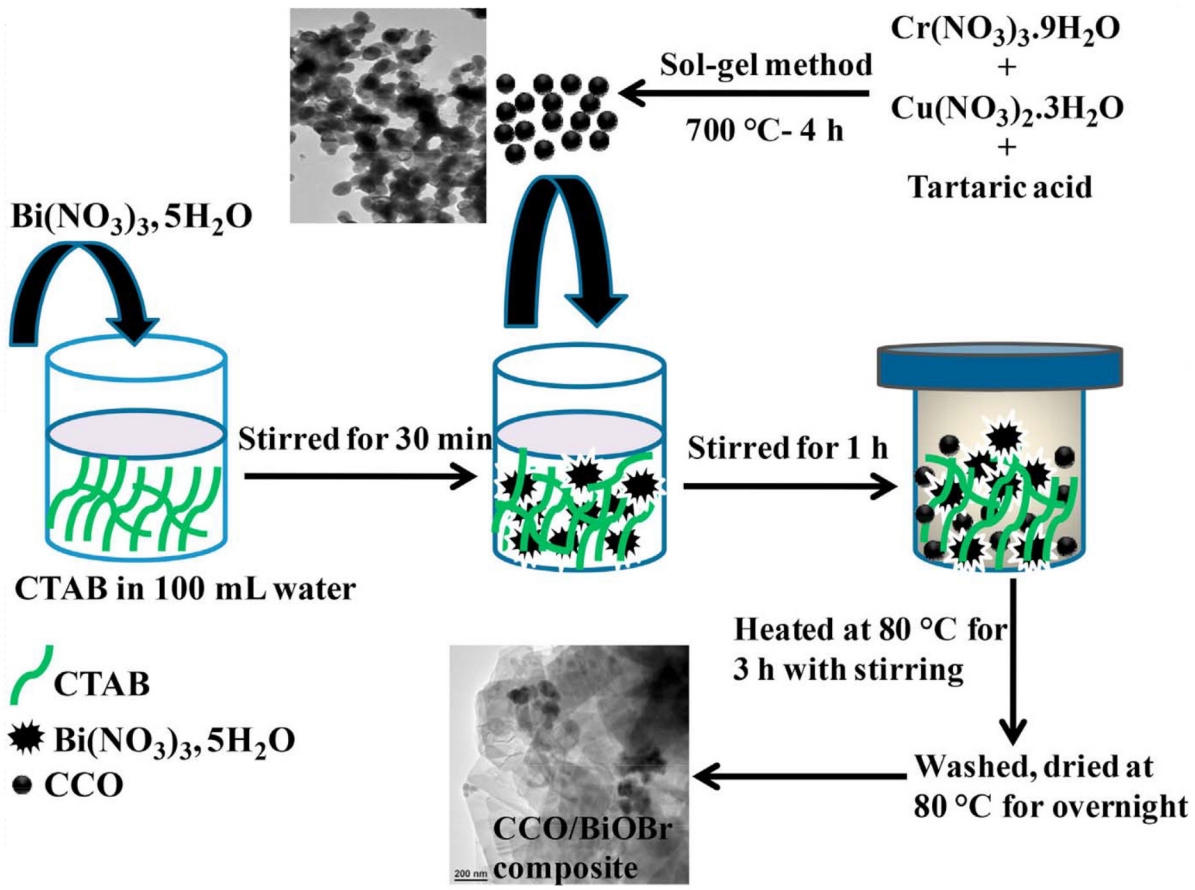


Fig. 9 Fabrication procedure of $CuCr_2O_4$/BiOBr nanocomposite.[112]

 

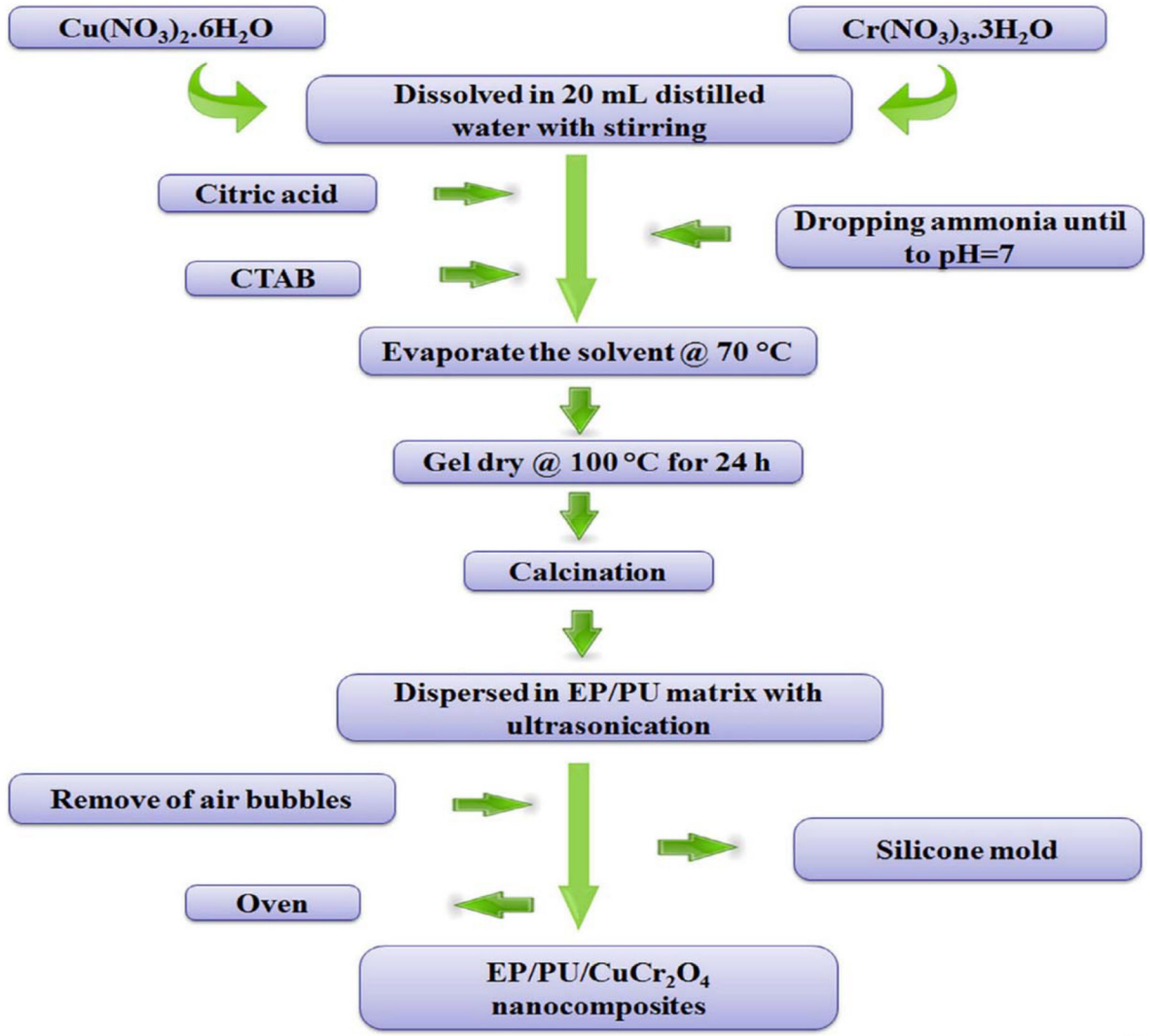


**Fig. 10** Schematic layout of the synthesis of EP/PU/$CuCr_2O_4$ nanocomposites.[128]

EP/PU matrix, the tensile test showed that the mechanical properties were greatly improved. The ideal composition was 0.76 wt% $CuCr_2O_4$ NPs and 2.6 wt% polyurethane in the epoxy resin. Additionally, molecular dynamics simulations showed how the NPs affected the mechanical properties and interaction energy of the nanocomposite.[128]

The synthesis of $CuCr_2O_4$ NPs *via* the co-precipitation technique, using 6 M KOH as the precipitating agent, is illustrated in Fig. 11a. The TGA examination of the as-dried sample, as shown in Fig. 11b, indicates a weight loss of 25% between 28 °C and 260 °C because of the removal of $C_2H_5OH$ and $H_2O$ and a slight weight loss of 5.5% between 400 °C and 460 °C because of the elimination of HCl. According to the study, annealing should occur at 460 °C, while slower heating rates could lower this temperature. Using XRD analysis, Fig. 11c verifies the generation of $CuCr_2O_4$ NPs, and Fig. 11d displays the optical absorbance band. The band gap of $CuCr_2O_4$ NPs is 3.35 eV, according to Fig. 11e.[129]

Susanti *et al.* produced N-doped reduced GO *via* hydrothermal temperature changes. XRD investigation revealed that the *d*-spacing value increased with temperature, indicating the presence of more substituted N atoms. The EDX examination revealed that the sample treated at a hydrothermal temperature of 160 °C had the highest N concentration (14.88%).[130] Interestingly, $CuCr_2O_4$ particles were supported on macroscopic polystyrene beads using a low-temperature ultrasonic technique.[8] According to the SEM pictures, the $CuCr_2O_4$ particles completely coated the PS surface.[131] TEM examination revealed that $CuCr_2O_4$ was uniformly distributed on rGO.[132]

Intriguingly, Shi *et al.* synthesized $CuCr_2O_4/SiO_2$ composite membranes by impregnating a quartz glass fibrous (QGF) membrane with Cu and Cr precursors, followed by drying at 110 °C and calcining at 700 °C. Flat and frisbee-shaped membranes with varying $CuCr_2O_4$ loadings were produced with the frisbee-shaped samples assembled with round EPS disks to

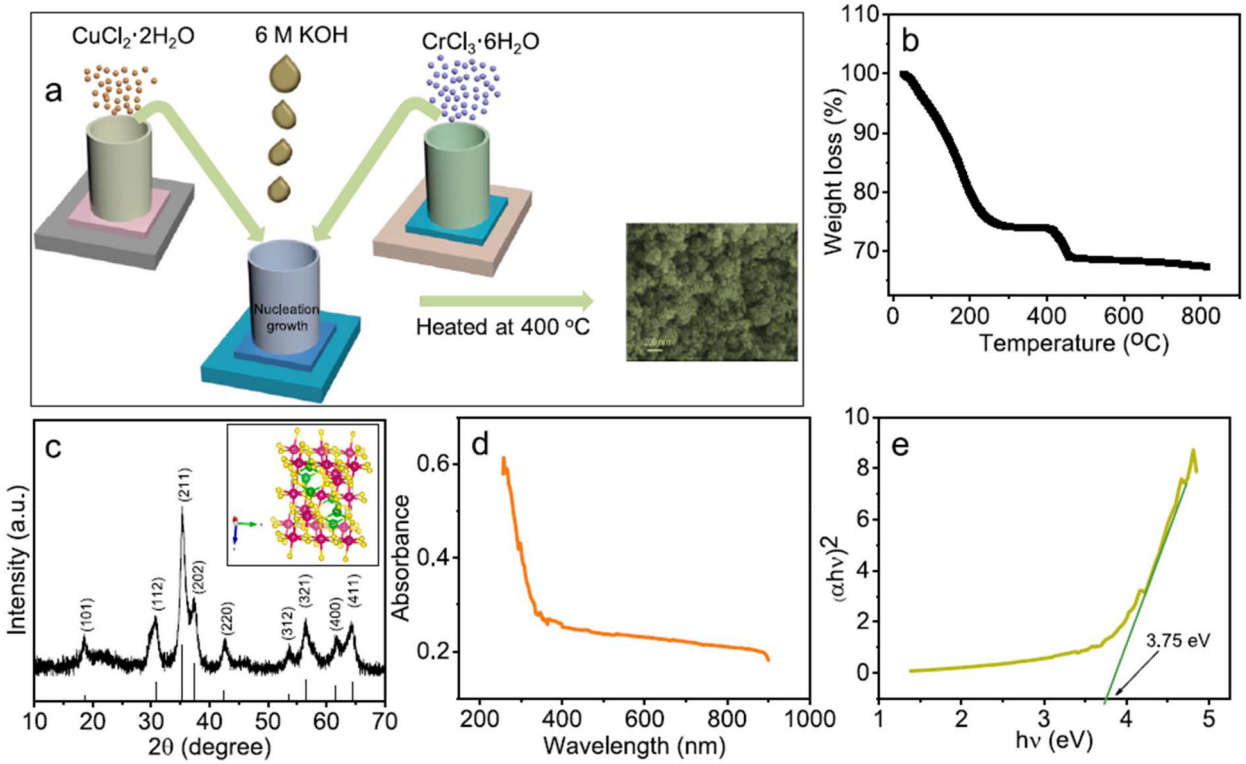


**Fig. 11** (a) Diagram of the synthesis of $CuCr_2O_4$ (with an image of the final product), (b) TGA, (c) XRD spectra of the NPs, with an inset showing thw crystal structure, (d) UV-visible spectra, and (e) optical band gap energy of $CuCr_2O_4$ NPs.[129]

enable floating and provide heat barrier functionality for water distillation performance testing (Fig. 12).[133]

Holec *et al.* used the sol–gel method to produce $ZnCr_2O_4/SiO_2$, $CuCr_2O_4/SiO_2$, and $CdCr_2O_4/SiO_2$, with $HNO_3$ as an acid catalyst, formamide (modifier), methanol (solvent), and TEOS (precursor). Furthermore, they studied the magnetic behavior of the synthesized NPs; among them, the magnetic behavior of $CuCr_2O_4$ exhibits a ZFC-FC bifurcation at 150 K, hysteresis necking at 2 K, indicating two magnetic phases, and a wide anomaly at 30 K attributed to a surface spin superparamagnetic-like phenomenon.[134] Ghorai *et al.* and their research team constructed $CuCr_2O_4$ and $TiO_2$ by chemically depositing

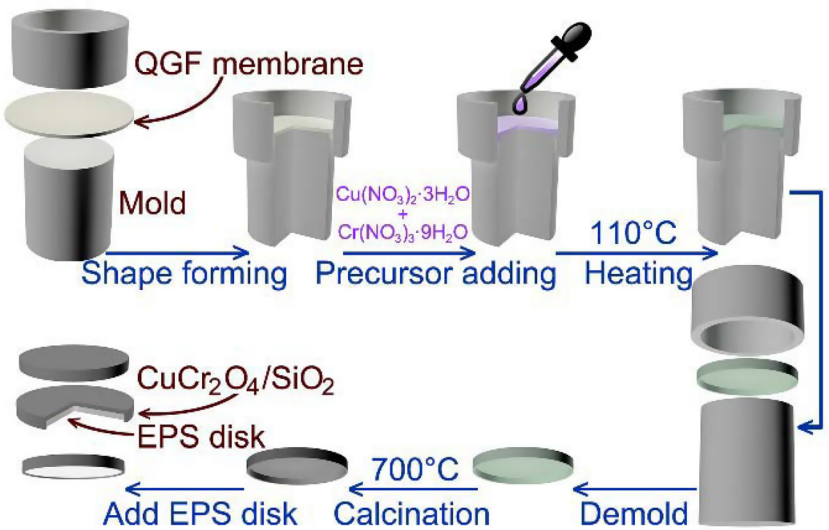


**Fig. 12** Frisbee-shaped $CuCr_2O_4/SiO_2$ composite membrane disk synthesis and EPS assembly to generate a composite $CuCr_2O_4/SiO_2$-EPS tandem-structured disk.[133]

$CuCr_2O_4$ on a Ti precursor *via* sonochemical treatment, followed by thermal treatment.[48] Sivaranjani *et al.* observed that adding $CuCr_2O_4$ increased the particle size and decreased the full-width at half-maximum of the $TiO_2$ patterns, indicating improved crystallinity. According to the XRD analysis, $CuCr_2O_4$ improves the crystal structure of $TiO_2$ NPs.[118]

Khan *et al.* found that coupling the $V_2O_5/CuCr_2O_4$–MCM-41 nanocomposite interface considerably improves the photocatalytic decomposition of alizarine red (AR) and bromothymol blue (BTB), as well as photoinhibition of *Staphylococcus aureus* and *Escherichia coli* bacteria.[135] Hosseini *et al.* employed CTAB and the sol–gel method to conduct a qualitative and quantitative study of $CuCr_2O_4$ NCs with different Cu and Cr molar ratios. Titration procedures were employed to determine the mass percentages of $Cr_2O_3$ and CuO. For each sample, the total percentage of $Cr_2O_3$ and CuO was approximately 100%, indicating the absence of impurities and confirming that the samples contained only $Cr_2O_3$ and CuO.[136] Vinothkumar *et al.* reported the synthesis of $CuCr_2O_4/Cr_2O_3$ NCs involving dissolving Cu(II) and Cr(III) precursors in dist. $H_2O$ with stirring to obtain a homogeneous solution. Liquid ammonia is then added as a precipitating agent. The resulting precipitate is dried and calcined to form $CuCr_2O_4/Cr_2O_3$ NCs. The researchers successfully studied the supercapacitor performance of $CuCr_2O_4/Cr_2O_3$ composites on nickel foam, as demonstrated in Fig. 13.[137]

Barman *et al.* created nano-copper chromite-loaded H-mordenite by combining equal quantities of copper and chromium salt precursors, followed by the addition of triethanolamine, while continuously stirring. To avoid precipitation, the pH was adjusted using $HNO_3$. The solution was heated, and the resulting fluffy mass was calcined at 923 K. The particle size was found to be 31 nm by TEM examination. The nano-copper chromite was then blended with H-mordenite in different ratios, mixed with 20% bentonite as a binder, extruded, and dried overnight at 373 K.[138] By thermally breaking down Cu(II) and Cr(III) carboxylate-type precursors that were generated *in situ* inside a silica matrix by a redox reaction with 1,3-propanediol, Ştefănescu *et al.* created $CuCr_2O_4/SiO_2$ and $Cu_2Cr_2O_4/SiO_2$ NCs that included 50 wt% of the corresponding oxides. Upon heating, the precursors decomposed at around 300 °C into amorphous CuO and $Cr_2O_{3-x}$. $Cr_2O_{3-x}$ crystallized to α-$Cr_2O_3$ at 400 °C, which reacted with CuO to form $Cu_2Cr_2O_4$. Further heating to 800 °C and 1000 °C resulted in the formation of residual CuO and well-crystallized $Cu_2Cr_2O_4$, respectively. In both composites, the oxides were uniformly distributed in the amorphous silica matrix. The samples produced at various annealing temperatures were analyzed using thermal techniques.[139]

Abbasi and colleagues used the sol–gel process to create spherical $CuCr_2O_4$ NPs with various amino acids as capping agents. They successfully examined how the molar ratio of the stabilizing agent affected the purity, particle size, and shape of the copper chromite. Moreover, a photodeposition method was used to create $CuCr_2O_4$/Ag nanostructures. They reported that the surface roughness and particle size increase in the $CuCr_2O_4$/Ag nanostructures compared to pristine $CuCr_2O_4$, indicating effective surface modification through Ag coating and potential impact on photocatalytic capabilities.[140]

Table 3 summarizes the diverse fabrication strategies, characterization techniques, and applications of $CuCr_2O_4$ nanocomposites.

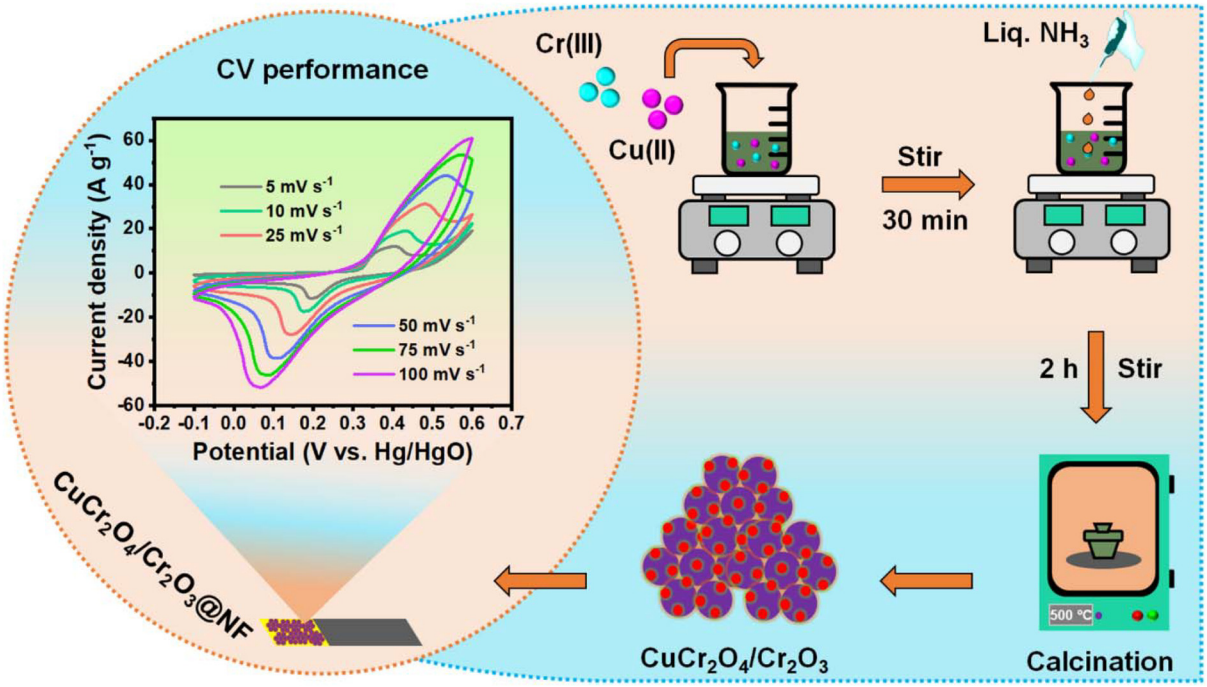


**Fig. 13** Schematic layout of the synthesis of $CuCr_2O_4/Cr_2O_3$ composite on an Ni foam for supercapacitors.[137]

Table 3 Summary of the synthesis method, characterization techniques, morphology, and applications of $CuCr_2O_4$ nanocomposites

| Nanocomposites | Synthesis method | Morphology | Particle size (nm) | Characterization techniques | Applications | Ref. |
|---|---|---|---|---|---|---|
| Ag-coated $CuCr_2O_4$ | Sol–gel | — | — | XRD, SEM-EDS, TEM, TG-DSC | Li-ion batteries | 46 |
| $CuCr_2O_4$·Pd/γ-$Al_2O_3$ | Sol–gel and impregnation | Rod | — | XRD, SEM-EDS, BET | Catalytic activity | 109 |
| $Bi_2O_3$/$CuCr_2O_4$–CuO core/shell | Co-precipitation | Spherical | 78 | XRD, TEM, EDS, FTIR | Catalytic activity | 111 |
| $CuCr_2O_4$ | Co-precipitation | Flake | — | XRD, UV-vis-DRS XPS, SEM-EDAX, SAED, BET, EIS, PL | Photocatalytic activity and genotoxic effect | 45 |
| $CuCr_2O_4$–$BiI_3O_9$ | Sono chemical | $CuCr_2O_4$ Cube $BiI_3O_9$ | | | | |
| $CuCr_2O_4$ | Sol–gel combustion | Spherical | 30–80 | XRD, UV-Vis, DRS, FESEM, TEM, HRTEM, EDX, XPSPL, BET, Raman spectroscopy | Photocatalytic and electrochemical activity | 112 |
| $CuCr_2O_4$/BiOBr | Co-precipitation | | | | | |
| $CuCr_2O_4$ $BiVO_4$ | Sol–gel Chemical route | Spherical | 65 | XRD, UV-vis, FTIR, PL | Photocatalytic activity | 141 |
| $CuCr_2O_4$@CaFe-LDO | — | — | — | XRD, UV–Vis, DRS XPS, SEM-EDX, TEM, TG–DTA | Photocatalytic activity | 114 |
| $CuCr_2O_4$@CaFe-LDO | — | — | 12.51 | — | Photocatalytic activity | 113 |
| $CuCr_2O_4$–$CeO_2$ | Sol–gel combustion | Semi-spherical | 15 | XRD, UV-Vis DRS, TEM, EDS, XPS, Raman spectroscopy, PL, BET | Photocatalytic activity | 115 |
| Cu/$CuCr_2O_4$ | Impregnation | — | 50–100 | XRD, FTIR, HRTEM, FESEM, XPS, XANES/EXAFS | Catalytic activity | 116 |
| $CuCrO_2$/$CuCr_2O_4$ | Ball milling | — | 174 ± 5 | XRD, UV-vis, FESEM, XPS, DTA, FESEM, EDS, TEM, SAED | Photocatalytic activity | 127 |
| $CuCr_2O_4$/CuO | Co-precipitation | — | — | SEM/EDAX, ICP/AES, XRD, and XPS | Catalytic activity | 142 |
| CuO–$CuCr_2O_4$ | Reflux condensation | Flower | — | XRD, UV-vis-DRS, TEM, PL, FESEM | Photocatalytic activity | 26 |
| EP/PU/$CuCr_2O_4$ | Sol–gel auto combustion | Octahedral | — | XRD, UV-vis, FTIR, SEM, XPS, TG–DSC | — | 128 |
| $CuCr_2O_4$–g-$C_3N_4$ | Ultrasonication-assisted | Irregular | 12–16 | XRD, FTIR, UV–vis DRS, TEM, PL, XPS, BET, EDX | Photocatalytic activity | 117 |
| g-$C_3N_4$–NS/$CuCr_2O_4$ | Refluxing | — | 12.6 | XRD, UV-Vis DRS, FTIR, SEM, EDX, TEM, XPS, PL, BET, TGA | Photocatalytic activity | 119 |
| $CuCr_2O_4$/GO | Co-precipitation | Quasi-spherical | GO-1.39 $CuCr_2O_4$/GO-3.54 | XRD, SEM, TEM, EDS, PL, Raman spectroscopy | Energy storage and electrochemical activity | 143 |
| $CuCr_2O_4$ and MWCNT/$CuCr_2O_4$ | Co-precipitation | Quasi-spherical | — | XRD, UV–Vis, FTIR, XPS, SEM-EDS, BET, HRTEM-SAED | Supercapacitor | 129 |
| MXene/$CuCr_2O_4$ | Co-precipitation | — | $CuCr_2O_4$-21.2, $Ti_3C_2T_x$-25.5 $Ti_3C_2T_x$/$CuCr_2O_4$-8.7 | UV-vis, SEM-EDX, zeta potential, Raman spectroscopy, PL, FTIR | Energy storage | 122 |
| N-doped graphene $CuCr_2O_4$ | Sonication-assisted mechanical mixing | — | — | XRD, FTIR, XPS, SEM-EDS, STEM | Supercapacitor | 121 |
| N-doped rGO $CuCr_2O_4$ | Sol–gel | — | — | XRD, FTIR, SEM-EDX | Supercapacitor | 130 |
| PANI: $CuCr_2O_4$ | — | Nano spherical | — | XRD, UV–Vis, FTIR, XPS, BET, TEM, and PL | Photocatalytic activity | 123 |
| $CuCr_2O_4$–PS | Low-temperature ultrasonic | — | — | XRD, FTIR, UV–Vis, SEM-EDS, BET | Photocatalytic activity | 131 |
| $CuCr_2O_4$/rGO | Hydrothermal | — | 50 | XRD, FTIR, TEM, TGA, XPS, zeta potential, Raman spectroscopy | Catalytic activity | 132 |
| $CuCr_2O_4$/$SiO_2$ | — | Frisbee | — | XRD, UV-vis-NIR, SEM, IR | Solar driven water evaporation | 133 |
| $CuCr_2O_4$/$SiO_2$ | Sol–gel | — | — | XRD, TEM | — | 134 |
| $CuCr_2O_4$/$SnO_2$ | Sol–gel | — | — | XRD, XPS, FTIR | Photocatalytic activity | 124 |
| $CuCr_2O_4$ $TiO_2$ | Sol–gel Sonication | Spherical Semi sphere | 25–30 6–10 | XRD, TEM-SAED, SEM-EDX, BET | Photocatalytic and photoeletrocatalytic activity | 48 |
| $CuCr_2O_4$/$TiO_2$ | Co-precipitation | — | 54 | XRD, UV-vis | Dye sensitized solar cell | 125 |
| $CuCr_2O_4$/$TiO_2$ | Sol–gel | — | 50 | XRD, UV-Vis-DRS, TEM | Photocatalytic activity | 144 |

**Table 3** *(Contd.)*

| Nanocomposites | Synthesis method | Morphology | Particle size (nm) | Characterization techniques | Applications | Ref. |
|---|---|---|---|---|---|---|
| $CuCr_2O_4$·0.7$TiO_2$–rGO | Sol–gel assisted Hummers' method | Spherical | 100 | XRD, FTIR, SEM-EDX, XPS, TGA-DTA, Raman spectroscopy | Catalytic activity | 145 |
| $CuCr_2O_4$/$TiO_2$ | Sol–gel | Spherical | 25–40 | XRD, SEM, TEM | Catalytic activity | 146 |
| $CuCr_2O_4$/$TiO_2$ | Sol–gel | — | 66 | XRD, DRS-UV, BET, FT-IR | Photocatalytic activity | 118 |
| $V_2O_5$/$CuCr_2O_4$/MCM-41 | Hydrothermal | $CuCr_2O_4$/MCM-41-hexagonal $V_2O_5$-spherical | 32<br>6 | XRD, UV–Vis, FTIR, BET, HRTEM, SEM-EDX, TGA | Photocatalytic and antibacterial activity | 135 |
| $CuCr_2O_4$ nanocomposites | Sol–gel | Pseudospherical | 50–500 | XRD, SEM, EDAX, FTIR | Photocatalytic activity | 136 |
| $CuCr_2O_4$–$Cr_2O_3$ | Co-precipitation | Spherical | ±25 | XRD, FTIR, UV-Vis, SEM, EDX TEM, SAED, XPS, EIS, BET | Supercapacitors | 137 |
| 50 mass% $CuCr_2O_4$/$SiO_2$ | Modified sol–gel | — | 43 | XRD, FTIR | — | 139 |
| 50 mass%$Cu_2Cr_2O_4$/$SiO_2$ | | | 50.5 | | | |
| $CuCr_2O_4$/Ag-leucine | Sol–gel | Quasi-spherical | 30–60 | ICP-OES, DRS, XRD, SEM, EDS, TEM | Photocatalytic activity | 140 |

# 3. The impact of experimental parameters on $CuCr_2O_4$ NPs physico-chemical properties

## 3.1. pH

According to Pakzad *et al.*, particle size is significantly affected by pH and the amount of fuel. Doubling the amount of fuel greatly increases the particle size. They observed that low citric acid (4 mmol) : glycine (10 mmol) and high citric acid (8 mmol) : glycine (20 mmol) ratios resulted in average particle sizes of 0.74 and 5.18 μm, respectively. It was also discovered that as the fuel/oxidizer ratio increased, the particle shape shifted toward octahedral structures, with larger particles observed at pH 9. They concluded that particle size increases with an increase in the fuel/nitrate ratio or solution pH.[17]

## 3.2. Time

Mobini *et al.* investigated the effect of aging time on material structure and found that prolonged aging significantly influenced crystallinity. They reported that the surface area increased from 20.4 to 42.8 $m^2\ g^{-1}$ as the aging period progressed. At the same time, the overall crystallinity decreased, accompanied by an increase in amorphous content and the development of different crystalline phases.[77] Chiu *et al.* delved into the impact of time on nanoparticle morphology. The topology of the fibers was altered significantly as the sintering time increased. All the fibers had a coarse morphology, and this roughness increased with sintering time.[88] Surprisingly, researchers aimed to study the development of 3D raspberry-like structures. They conducted time-dependent experiments at 180 °C utilizing a hydrothermal approach. As seen in Fig. 14, after 18 h of crystallization, the particles formed a raspberry-like shape with homogeneous diameters. However, prolonged crystallization (>18 h) led to the development of polydispersed particles.[78] Similarly, Yuan *et al.* used a Teflon-lined stainless-steel autoclave heated to 180 °C and maintained for 11 h to synthesise cubic-like $CuCr_2O_4$ particles.[22]

## 3.3. Concentration

Sankudevan *et al.* found that increasing the Mn doping concentration in $CuCr_2O_4$ NPs reduced the particle size from 37 to 26 nm, as confirmed by XRD analysis.[43] Pure CuO and CuO–$CuCr_2O_4$ NCs were made with various $Cr^{3+}$ concentrations. The monoclinic structure of pure CuO is reflected in its XRD. CuO–$CuCr_2O_4$ with a 10% $Cr^{3+}$ concentration exhibits a weak peak at 18.12°, indicating the presence of $CuCr_2O_4$, which has a tetragonal structure. The $CuCr_2O_4$ peak intensifies when the $Cr^{3+}$ concentration increases (CuO–$CuCr_2O_4$: 20% $Cr^{3+}$ concentration and CuO–$CuCr_2O_4$: 30% $Cr^{3+}$ concentration), whereas the CuO peaks diminish. The crystallite size decreases with an increase in $Cr^{3+}$ content, indicating that $CuCr_2O_4$ inhibits CuO growth and may diminish the lattice characteristics of CuO.[26] Batool *et al.* reported that the grain size reduced when the Cd and Nd doping concentrations increased, which was further

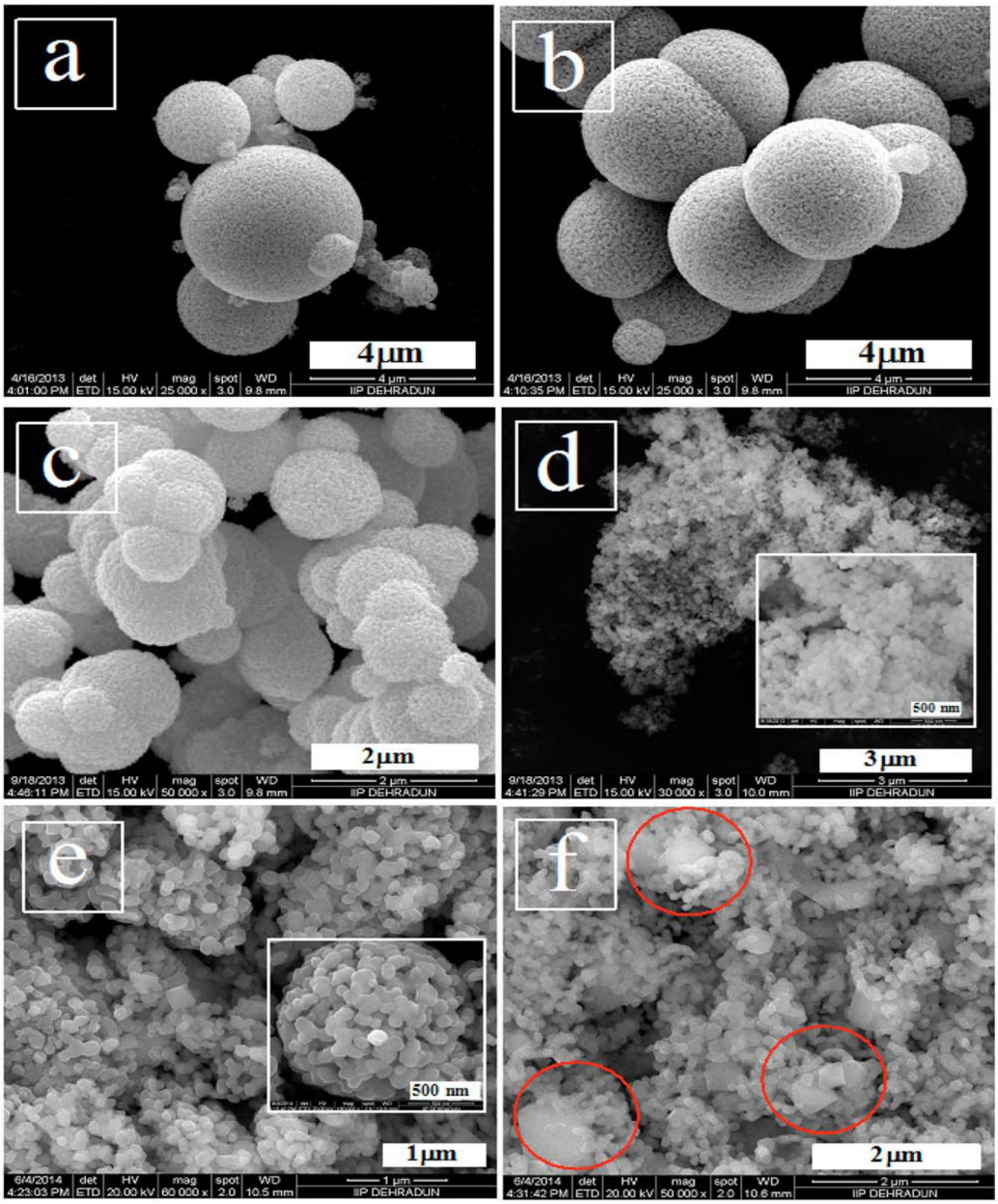


**Fig. 14** SEM images of $CuCr_2O_4$ NPs synthesized using hydrothermal techniques at 180 °C for (a) 6 h, (b) 18 h, (c) 72 h, (d) 7 days, (e) after 7 days of constant stirring, and (f) after 7 days of aging.[78]

confirmed by SEM analysis.[102] Ramezanalizadeh *et al.* investigated the effect of varying the La loading on the morphology, size, and crystallinity of $CuCr_2O_4$ NPs using FESEM analysis. According to the experimental findings, the shape of the nanostructure changed dramatically with an increase in La concentration, going from plate-like at 0.35 La loading to spherical-like at 0.7, as shown in Fig. 15. Additionally, a marked change in particle size was observed. These structural and morphological changes, as supported by XRD data, indicate that the addition of La to the $CuCr_2O_4$ lattice has a significant impact on the crystalline phases and physical properties of the material.[100]

### 3.4. Temperature

Hosseini *et al.* investigated several factors, including the Cu/Cr ratio and calcination temperature in the range of 500–750 °C, to examine the formation of diverse phases, including $CuCr_2O_4$, CuO, and $CuCrO_2$. It was established that the phase composition of the resulting $CuCr_2O_4$ NPs is determined by the molar ratio of Cu–Cr in the initial reactants. When the reaction temperature is set to 600 °C and the Cu/Cr molar ratio is 0.5, pure spinel $CuCr_2O_4$ NPs are obtained.[50]

Tavakoli *et al.* demonstrated that the phase structure of the $CuCr_2O_4$ compound depends on the initial reactant tempera-

 

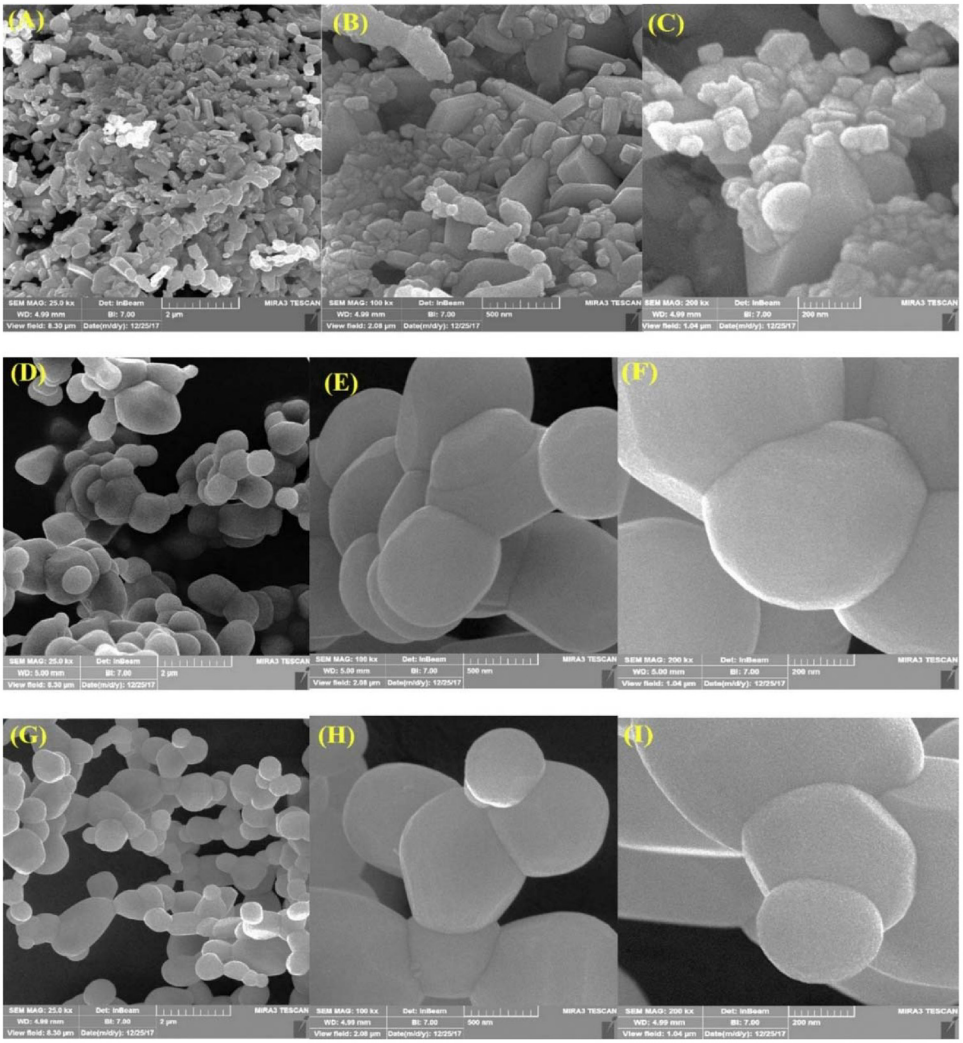


**Fig. 15** FESEM images of $CuCr_{1.65}La_{0.35}O_4$ (A–C), $CuCr_{1.3}La_{0.7}O_4$ (D–F), and $CuCrLaO_4$ (G–I).[100]

ture and the molar ratio of Cu : Cr.[70] Pal *et al.* observed that $CuCr_2O_4$ samples synthesized at 400–500 °C formed NPs with slight agglomeration, while calcination at 550 °C led to significant particle growth and the formation of predominantly octahedral-shaped structures. The particle size increased in tandem with the calcination temperature, primarily due to the aggregation of smaller particles at higher temperatures.[71] Chiu *et al.* tested a sample sintered at temperatures in the range of 500–800 °C for varying periods of time. The fiber sintered at 500 °C included a combination of $Cr_2O_3$ and $CuCr_2O_4$, but sintering at 600–800 °C produced single-phase $CuCr_2O_4$. The mean fiber diameter reached 500 nm. Secondary-phase $Cr_2O_3$ was discovered when the fiber was sintered at 700 °C for 5 and 10 min, while single-phase $CuCr_2O_4$ occurred when the sintering time was raised to 15–30 min.[88] Mobinia's study suggested that the thermal sintering of particles at high temperatures causes the BET surface area to decrease, given that sintering reduces the porosity and crystal size.[77]

Billman *et al.* suggested that the modified Pechini method produces smaller particle sizes and increased agglomeration. The measured particle growth kinetics are consistent with a diffusion-limited, inhibited grain growth model.[58] Similarly, Tsai *et al.* revealed that higher temperatures increase the particle size by boosting atomic diffusion, and also enlarge the voids by inducing atoms to cluster around the void margins due to capillary forces. They further reported that annealing the nanostructure at 500 °C transformed the film structure from amorphous to a mixture of monoclinic CuO and spinel $CuCr_2O_4$. Delafossite $CuCrO_2$ was formed by further annealing at 600 °C, which depleted the $CuCr_2O_4$ phase. Increasing the annealing temperature also altered the microstructure, evolving from compact nanograins to larger agglomerated grains with voids, resulting in a rougher surface.[89] Similarly, Batool *et al.* also observed the effect of temperature on the morphology of $CuCr_2O_4$ NPs doped with Mg. The researchers observed that at lower temperatures, the particles exhibited quasi-spherical shapes with low homogeneity. As the temperature increased, the particle size increased, and the shapes became less uniform. The particles showed higher aggregation, less spherical appearance, and more disorder at 750 °C.[105]

### 3.5. Fuel

Capping agents play a crucial role in the synthesis of nanoparticles by increasing the monodispersity, reducing the particle size, and preventing the aggregation of NPs. Sathiskumar and colleagues studied Cu–Cr–O NC oxide catalysts manufactured using various Cu–Cr mole ratios to better understand the impact of the mole ratio on the final product, using fuels such as glycine and citric acid.[8] Bisht *et al.* utilized capping agents, namely, urea, coconut oil, oleic acid, and citric acid, to generate $CuCr_2O_4$ NPs. It was observed that improved surface capping occurred in the presence of oleic acid.[82] Paymenfar *et al.* studied the influence of a capping agent on $CuCr_2O_4$ NPs using FESEM analysis. According to the analysis, they concluded that the uncapped particles exhibited a semi-spherical morphology with noticeable aggregation and low monodispersity. In contrast, the use of sucrose as a green capping agent reduced the particle size, minimized the agglomeration, and greatly enhanced the monodispersity. The findings demonstrate the importance of the capping agent in regulating the shape and crystallinity of nanoparticles during sol–gel production.[51] To adjust morphology and particle size, Kumar *et al.* employed a variety of surfactants, including PEG, CTAB, and PVP. Among them, the $CuCr_2O_4$ material made with CTAB surfactant exhibits the greatest specific capacitance due to its larger surface area, rougher surface, and enhanced ion adsorption active sites resulting from its spherical shape.[73] Al-Wasidi *et al.* created $CuCr_2O_4$ NPs with and without citric acid and tartaric acid as templates. The presence of organic acids caused lower crystallite sizes. Organic templates had a considerable influence on crystallite size and morphology; the nanoparticles produced without templates had irregular forms, but those with templates were spherical.[81] The impact of glycine, alanine, valine, and leucine as capping agents in the synthesis of $CuCr_2O_4$ NPs was examined by Ali Abbasi *et al.* Glycine, the smallest amino acid, has a weak steric barrier due to its tiny molecular size, resulting in the development of agglomerated particles with an unknown shape. In contrast, the NPs synthesised with leucine as both a capping and reducing agent have a well-defined, sphere-like shape. Among the amino acids investigated, leucine exhibited the most pronounced steric hindrance effect, resulting in more uniform and smaller particles. Based on the structural properties of the amino acids, it can be concluded that larger amino acids provide more steric hindrance, which is advantageous for the controlled synthesis of subminiature NPs with enhanced shape and reduced agglomeration.[140]

Table 4 describes the diverse parameter-dependent fabrication of $CuCr_2O_4$ nanomaterials.

## 4. Proposed mechanism for plant extract-mediated green synthesis of $CuCr_2O_4$ NPs

This eco-friendly process produces nanoparticles that are more stable, less prone to deformation and aggregation, and promote the adsorption of phytochemicals on their surface, thereby accelerating the reaction times.[147] Lachini *et al.* employed an aqueous extract of *Aloe vera* leaves as a reducing agent for the synthesis of $CuCr_2O_4$ NPs.[49] Fig. 16 presents the probable mechanistic process for the green synthesis of $CuCr_2O_4$ NPs. The proposed reaction mechanism demonstrates the stabilising and reducing effects of active phytochemicals. Numerous active phytochemicals, including anthraquinones, polysaccharides, flavonoids, vitamins, enzymes, saponins, tannins, and sterols, are found in *Aloe vera* leaves.[148–150] To suggest the possible reaction mechanism, a flavonoid has been chosen as a model biomolecule.[151] The electrostatic interaction between the hydroxyl groups of flavonoids and the cations of metal precursors causes aromatic hydroxyl groups to bind to copper and chromium ions, and stable complexes are formed between the metal ions and flavonoids. After calcination, the complex breaks down, yielding $CuCr_2O_4$ NPs.

Furthermore, the $CuCr_2O_4$ NPs were created by reducing $Cu^{2+}$ and $Cr^{3+}$ ions using bioactive phytochemicals, such as polyphenols, flavonoids, and terpenoids, which are present in rosemary leaf extract and serve as natural stabilizing and reducing agents. The reduction was then finished by adding $NaBH_4$, and the crystalline spinel structure was achieved by calcining the mixture at 650 °C.[41]

## 5. Applications of $CuCr_2O_4$ nanomaterials

### 5.1. $CuCr_2O_4$ nanomaterials as catalysts

In an aqueous medium, ethyl acetoacetate, hydrazine hydrate, and aldehydes underwent a pseudo-five-component reaction to produce 4,4′-(arylmethanediyl)bis(3-methyl-1*H*-pyrazol-5-ols), according to Safaei-Ghomi *et al.* (Scheme 1).[67]

Safaei-Ghomi *et al.* utilized $CuCr_2O_4$ NPs as a catalyst in the Ullman reaction. C–N cross-coupling reactions between anilines and iodobenzenes were performed in toluene under reflux conditions with a nitrogen atmosphere, using KOH as the base and a $CuCr_2O_4$ nanocatalyst under ligand-free conditions. This nanocatalyst enhanced the pace and efficiency of triarylamine synthesis (Scheme 2).[16]

Shahbazi-Alavi *et al.* described a one-pot pseudo-five-component condensation reaction utilizing a nano-$CuCr_2O_4$ catalyst to produce bis-thiazolidinones (Scheme 3). The creation of primary imine intermediates, followed by the attack of the sulphur atoms of thioglycolic acid on the activated imine groups, intramolecular cyclization, and the removal of water, results in the cyclized product bis-thiazolidines, according to the suggested mechanism. By activating the C=O, C=N, and S–H groups, the nano-$CuCr_2O_4$ surface atoms improve the interaction with nucleophiles. These surface atoms are hubs for catalytically stimulating chemical processes.[68]

The study by Shahbazi-Alavi *et al.* employed a similar process, but they incorporated ammonium acetate as a key component to alter the synthesis of arylated dipyrazolodihydropyridine derivatives. When ammonium acetate, EAA, 4-nitrobenzal-

 

**Table 4** Overview of the parameters influencing the development of $CuCr_2O_4$ NPs

| | Parameters for the synthesis of $CuCr_2O_4$ NPs | | | | | | | |
|---|---|---|---|---|---|---|---|---|
| | | | | | Temperature | | | |
| Synthesis method | Concentration of Cu salt or weight | Concentration of Cr salt or weight | Molar ratio $Cr^{3+}$ : $Cu^{2+}$ | pH | Reaction (°C) | Calcination (°C) | Time (h) | Ref. |
| Sol–gel | 0.01 mol | 0.02 mol | — | — | 95 | 600 | 3 | 50 |
| | — | — | — | — | 50 | 700 | 6 | 52 |
| | 0.01 | 0.02 | — | — | 90 | 750 and 850 | 4 | 53 |
| | — | — | 1 : 2 | 8.5 | 90 | 300 and 850 | 6 and 4 | 42 |
| | 2 mmol | 4 mmol | — | — | 70 | — | — | 55 |
| | — | — | — | 10–11 | 80 | 820 | 4 | 56 |
| | 0.799 g | 1.833 g | — | — | 180 | 600 | 4 | 60 |
| | — | — | 1 : 2 | 7 | 120 | 900 | 24 | 46 |
| | — | — | 0.5 | 3 | — | 550 | 5 | 109 |
| | 0.005 mol | 0.01 mol | — | — | 80 | 800 | 1.5 | 141 |
| | — | — | — | — | 95 | 750 | 4 | 143 |
| | 0.1 mol | 0.2 mol | — | — | 50–65 | 500 | 2 | 121 |
| | — | — | — | — | 40 | 800, 900, 1000, 1100 | 2 | 134 |
| | 0.005 mol | 0.01 mol | — | — | 80 | 300, 500, 700 | 1.5 | 144 |
| | 5 mmol | 10 mmol | — | — | 80 | 600 | 3 | 146 |
| | 5 mM | 10 mM | — | — | 95 | 600 | 3 | 118 |
| | 0.01 | 0.02 | — | ~7 | 90 | 750 | 4 | 102 |
| | 0.01 mol | 0.02 mol | — | — | 95 | 600 | 3 | 99 |
| | 2.0 g | 10 g | — | 8 | 180 | 750 | 6 | 27 |
| | 0.01296 | 0.02592 | 1 : 1 | — | 90 | 800 | 3 | 139 |
| | 0.5 g (2 mmol) | 1.658 g (4 mmol) | 1 : 2 | 7 | 70 | 1000 | 2 | 62 |
| | 1 mmol | 2 mmol | 1 : 2 | — | 70 | 650 | 3 | 140 |
| Sol–gel auto combustion | 7.5 mmol | 15 mmol | 1 : 2 | 8–10 | 90 | 950 | 1 | 17 |
| | — | — | — | — | 120 | 900 | 10 | 59 |
| | 0.9053 g | 3 g | — | — | 80 | 700 | 4 | 112 |
| | 2.152 mmol | 4.298 mmol | — | 7 | 70 | 700 | 3 | 128 |
| | 0.9057 g | 3 g | 1 : 2 | — | 80 | 700 | 4 | 48 |
| Sol–gel | 1 mmol | 2 mmol | — | — | 80 | 650 | 3 | 49 |
| Green synthesis | 1 mmol | 2 mmol | — | — | 100 | 650 | 3 | |
| Pechini | 0.07 mol | 0.1 mol | — | — | 95 | 600 | 3 | 57 |
| Pechini-and modified Pechini | — | — | 1 : 2 | 7 | 80 | 650, 750, and 850 | 1 and 24 h | 58 |
| Combustion | 36.23 g | 60 g | — | — | — | 750–800 | 2 | 65 |
| | 0.5 M | 1 M | — | — | | 400 | 5 | 101 |
| Self-combustion | 10 mmol | 20 mmol | — | — | 90 | 600 | 3 | 64 |
| Co-precipitation | 1.4 g | 4.0 g | — | 10 | 80 | 600 | 5 | 16, 38 and 67–69 |
| | 0.020 mol | 0.040 mol | — | — | — | 400, 450, 500 and 600 | 3 | 71 |
| | 0.35 M | 0.35 M | — | — | — | 300 Reduced with $H_2$ 300 | 6 8 | 92 |
| | 1.208 g | 4.0015 g | — | — | 110 | 600 and 700 | 4 | 23 |
| | 0.5 M | 0.5 M | — | 8 | 90 | 800 | 5 | 111 |
| | 0.1 M | 0.2 M | — | 11 | 80 | 700 | 4 | 45 |
| | 0.005 mol | 0.01 mol | — | 8–9 | — | 1000 | 2 | 72 |
| | 1.70 g | 5.32 g | — | — | 85 | 400 | 4 | 129 |
| | — | — | 1 : 2 | — | — | 700 | 6 | 131 |
| | 0.05 mol $L^{-1}$ | — | 8–9 | — | — | 900 | 1 | 98 |
| Inverse-coprecipitation | 0.005 mol | 0.01 mol | 1 : 2 | 9 | — | 400, 520, and 800 | 2 | 70 |

Table 4 *(Contd.)*

| Synthesis method | Parameters for the synthesis of $CuCr_2O_4$ NPs | | | | | | | |
|---|---|---|---|---|---|---|---|---|
| | Concentration of Cu salt or weight | Concentration of Cr salt or weight | Molar ratio $Cr^{3+}$ : $Cu^{2+}$ | pH | Temperature | | Time (h) | Ref. |
| | | | | | Reaction (°C) | Calcination (°C) | | |
| Hydrothermal | 1.5 g | 5.0 g | 1 : 2 | 8 | 180 | 750 | 6 | 74 and 75 |
| | 3.5 g | 11 g | 1 : 2 | 8 | 200 | 700 | - | 35 |
| | 5 mmol | 10 mmol | 1 : 2 | 10–10.3 | 70 | 500–800 | 4 | 22 |
| | 2.25 g | 7.5 g | 1 : 2 | 8 | 180 | 750 | 6 | 24 |
| | 5.54 g | 15.4 g | — | 7 | — | 500 | 5 | 47 |
| | 2.3 g | 7.5 g | 1 : 2 | 8 | 180 | 750 | 6 | 76 |
| | 3.8 g | 12.3 g | 1 : 2 | 9 | 180 | 650 | 6 | 39 |
| | 0.1 g | 0.27 g | — | — | 120 | 400 | 3 | 40 |
| | — | — | 1 : 2 | 9, 10, 11, 12 | 160, 180 and 200 (11 h) | 400, 500, 600 and 700 | 4 | 77 |
| | 1 mmol | 2 mmol | — | 14 | 180 | 700 | 5 | 80 |
| | 2.6 g | 2.7 | 1 : 2 | — | 180 | 800 | 6 | 78 |
| | 1 mmol | 2 mmol | — | — | — | — | — | 93 |
| | 1 M | 2 M | — | 10–11.5 | 200 | 550 | 5 | 14 |
| | Equal | Equal | — | 7 | 200 | 750 | 5 | 95 and 103 |
| | 5.5 g | 16 g | — | 8 | 200 | 750 | — | 97 |
| | 2.30 g | 7.50 g | — | 10 | 180 | 700 | 6 | 81 |
| Microwave | 1 mmol | 2 mmol | — | — | — | 500–800 | 3 | 82 |
| Ultrasonication assisted | 5.5 g | 15.4 g | — | — | 40 | 550 | 3 | 117 |
| Refluxing | 0.03 g | 0.19 g | — | 10 | 96 | 520 | 4 | 119 |
| — | 5.54 g | 15.4 g | — | 7 | 60 | 500 | 5 | 123 |
| — | 0.03 g | 0.07 g | — | 10 | 60 | 500 | 4 | 135 |
| Co-precipitation, ultrasound, and green chemistry | 1.7 g | 0.5 M | — | 7 | — | 650 | 4 | 41 |

dehyde, and hydrazine hydrate were reacted in ethanol at room temperature, using nano-$CuCr_2O_4$ as a catalyst, significant yields of tetrahydrodipyrazolopyridines were produced (Scheme 4). Furthermore, the recyclability of the catalyst was demonstrated up to five cycles in the model reaction.[152]

Wołosiak-Hnat *et al.* produced a $CuCr_2O_4$ catalyst with a more crystalline structure and a higher copper concentration than the commercial catalyst, enabling greater selectivity for 1,2-propanediol. At 210 °C, 80 wt% aqueous glycerol and 8 wt% catalyst resulted in the maximum glycerol conversion of 76.9% and 90.7% selectivity to 1,2-propanediol compared to the inserted glycerol, respectively. The studies were conducted under an initial hydrogen pressure of 3.0 MPa, stirring speed of 100 rpm, reaction time of 24 h, and pressure of 5.6 MPa throughout the process. Under the same conditions, the maximum selectivity for 1,3-propanediol was just 2.5% at a glycerol conversion rate of 30.9%. This study suggested that the catalyst must be present for the C–O bond in alcohols to be activated for hydrogenolysis. The hydrogenolysis of glycerol to 1,2- and 1,3-propanediol is generally considered a two-step procedure. Glycerol is dehydrated to produce acetol or 3-hydroxypropanal in the first stage. Hydrogenating these intermediates to 1,2- and 1,3-propanediol, respectively, is the second step (Scheme 5).[92]

Karimi-Jaberi *et al.* described the formation of benzylidene bis(4-hydroxycoumarin) and dihydropyrano[*c*]chromene analogs in $H_2O$ at RT with nano-$CuCr_2O_4$ as a catalyst. This process is eco-friendly, consumes less time, produces high yields, and the catalyst can be reused, making it simple, practical, and sustainable (Scheme 6a and b).[38]

Acharyya and research team have published multiple reports on the synthesis of $CuCr_2O_4$ NPs and their catalytic activity. In this report, a nano-catalyst with improved thermal stability and enhanced catalytic performance in the hydroxylation of benzene to phenol, oxidation of ethylbenzene to acetophenone, and oxidation of aniline to azoxybenzene was generated, utilizing $H_2O_2$ as the oxidizing agent. The study found that at 80 °C, the benzene conversion was 72.5% with 94% phenol selectivity (entry 1, Table 5).[74] In comparison, at 70 °C, the ethylbenzene conversion was 68.5%, yielding 78% acetophenone (entry 2, Table 5),[75] aniline conversion was 78%, with 92% selectivity to azoxybenzene (entry 3, Table 5),[35] at 75 °C the benzene conversion of 67% with 94% phenol selectivity (entry 4, Table 5),[15] and at 50 °C, 70% cyclohexane conversion and 85% selectivity towards cyclohexanone (entry 5, Table 5),[76] and 57.5% toluene conversion with 84.4% selectivity of benzaldehyde. $CuCr_2O_4$ NPs can be reused several times without losing effectiveness (entry 6, Table 5).[39] Similarly, the effect of Cu(II) nanoclusters supported by $CuCrO_4$ spinel NPs on the selective oxidation of ethanol was investigated. Without a solvent, this process yielded 65% con-

 

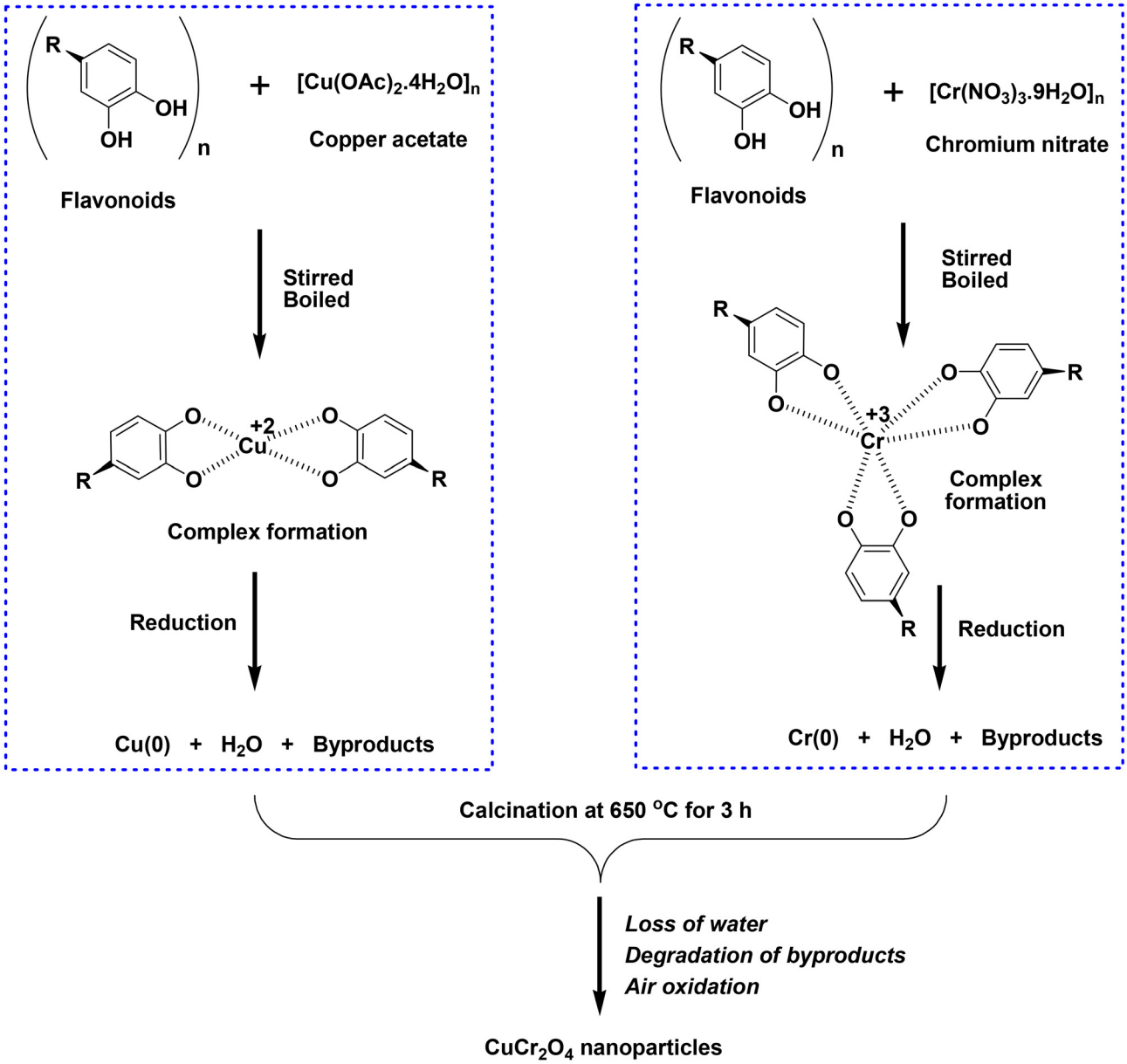


**Fig. 16** Possible reaction mechanism behind the green synthesis of $CuCr_2O_4$ NPs using plant extract.

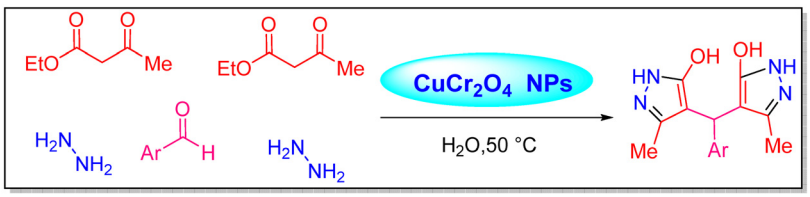


**Scheme 1** Production of 4,4′-(arylmethanediyl)bis(3-methyl-1*H*-pyrazol-5-ol) analogues using catalytic amounts of $CuCr_2O_4$ NPs.[67]

version of ethanol to acetic acid with 97% selectivity at 75 °C, utilizing $H_2O_2$ as the liquid-phase oxidant.[97] However, Table 5 describes the diverse organic transformations catalyzed by $CuCr_2O_4$ NPs.

In another study, Cu(II) nanoclusters supported on $CuCr_2O_4$ NPs were used to explore their catalytic activity in the sustained oxyamination conversion of benzene to aniline *via* a direct procedure employing $NH_3$ and $H_2O_2$. The technique was

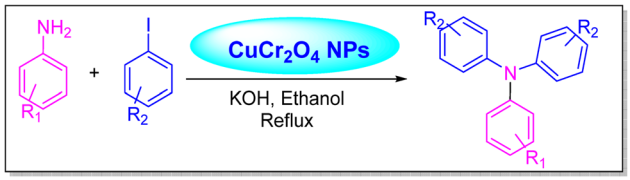


**Scheme 2** Triarylamine synthesis using $CuCr_2O_4$ NPs.[16]

efficient in terms of activity, selectivity, mild reaction conditions, and catalyst. The Cu(II) component was found to significantly affect both the conversion rate and product selectivity.[96]

Scheme 7 illustrates that ultra-small Cu(II) oxide supported on $CuCr_2O_4$ spinel NPs participates in converting benzene to phenol when air is used as an oxidant. The textural promoter Cr(III) prevents the sintering of Cu(II) oxide, thereby preserving the surface area of the catalyst during the reaction. In this process, the supported Cu(II) species is reduced by benzene to Cu(I) species **A**, which subsequently transitions into its canonical form **B**. Simultaneously, benzene generates a peroxide radical ($HOO^{\bullet}$) and a benzene radical cation ($C_6H_6^{\bullet+}$). The benzene radical cation then reacts with species **B** to form complex **C**, which subsequently converts into its canonical form **D**. After that, a proton is removed by complex **D**, restoring aromaticity and creating intermediate **E**. Phenol and Cu(II) oxide species **F** are produced when intermediate **E** dissociates. The interaction between species **F** and the concurrently generated hydroxyl radical ($^{\bullet}OH$) results in the production of intermediate **G**. The catalytic cycle is finished when a benzene molecule reduces **G** back to Cu(I) species, creating a benzene radical cation that rejoins the cycle.[24]

Chen *et al.* found that $CuCr_2O_4$ was the most effective catalyst, achieving a cyclohexane conversion rate of up to 95.8% and a cyclohexanone selectivity of 78.1%. The catalyst also showed good cycle stability after five cycles.[132]

Abdolmohammadi's research shows that $CuCr_2O_4$ NPs have a larger surface area due to their acidic coordinated sites. $CuCr_2O_4$ NPs interact with the carbonyl oxygen group in (*E*)-1,2-diphenyl-1-diazene to generate an intermediate. This intermediate then undergoes a Knoevenagel reaction with 4-hydroxycoumarin, resulting in the formation of an alkene. Following that, a Michael-type addition occurs, in which another mole of 4-hydroxycoumarin interacts with the alkene. After cyclization and dehydration procedures, 7-(4-hydroxy-2-oxo-2*H*-[1]benzopyran-3-yl)-9-[(*E*)-2-(phenyl)-1-diazenyl]-6*H*,7*H*-[1]benzopyrano[4,3-*b*][1]benzopyran-6-one is produced (Scheme 8).[40]

The long-term stability test results show that the catalyst exhibited excellent stability, even at 400 °C in the presence of $CO_2$ and water vapor. The calcination temperature is a key factor in improving the catalytic performance in the oxidation of CO.[77]

Interestingly, a zinc oxide-doped, strongly acidic zeolite catalyst increased the formation of a toluene intermediate during the catalytic pyrolysis of cellulose. As shown in Fig. 17, $CuCr_2O_4$@MCM-41 exhibited strong catalytic activity. $H_2O_2$, as an oxidizing agent, under optimal conditions of 60 °C and 4 h, resulted in 87.5% cresol selectivity and 83.0% conversion.[153]

Scheme 9 depicts a multicomponent reaction involving 3,4-methylenedioxyphenol, aromatic aldehydes, and C–H-activated acidic compounds, such as dimedone. This method confirmed the universality of the route by producing high yields of xanthenones and chromenopyrimidinediones. Water was used as a green, non-volatile solvent, and ultrasonic irradiation was

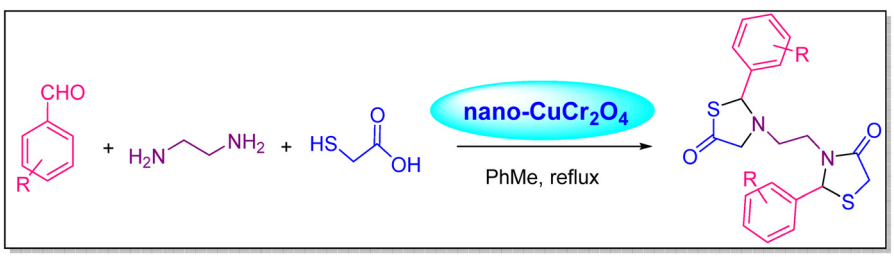


**Scheme 3** Bis-thiazolidine synthesis using nano-$CuCr_2O_4$ catalyst.[68]

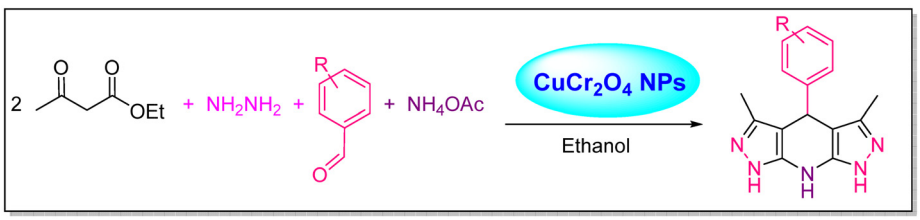


**Scheme 4** Preparation of tetrahydrodipyrazolopyridines using nano-$CuCr_2O_4$.[152]

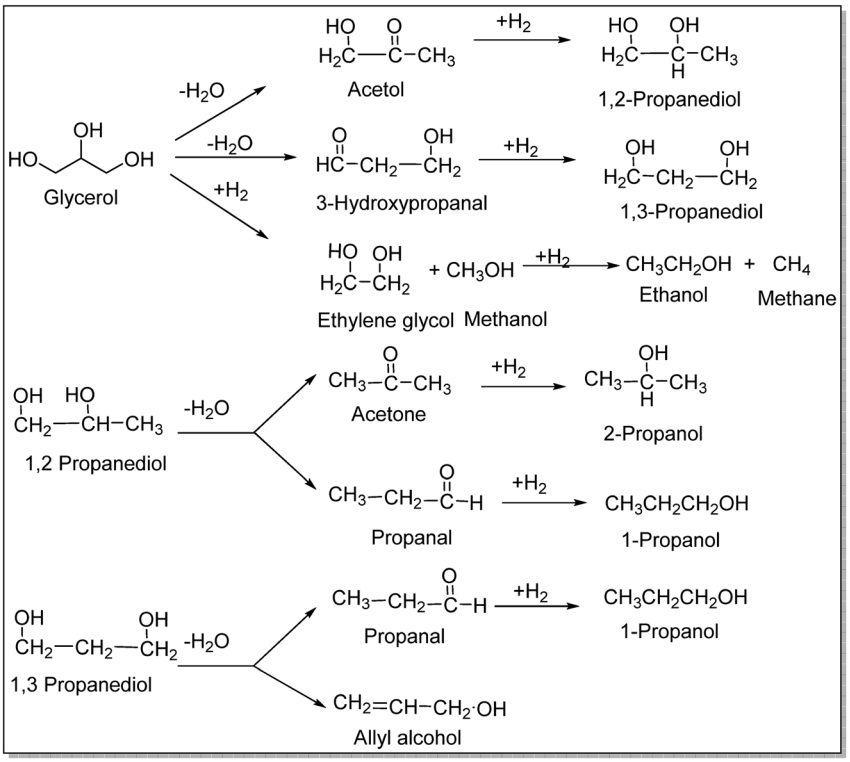


**Scheme 5** Possible pathways for the catalytic hydrogenolysis of glycerol.[92]

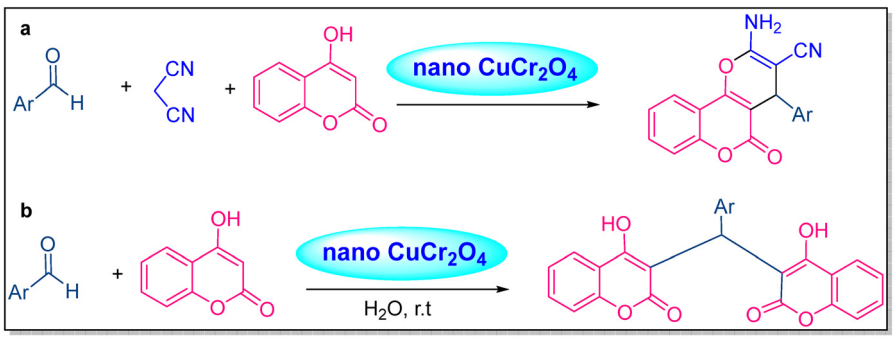


**Scheme 6** (a) Synthesis of dihydropyrano[*c*]chromene and (b) benzylidene bis(4-hydroxycoumarin).[38]

employed as a safe energy source, enabling the quick synthesis of products.[154]

Kien and colleagues examined the fact that Pd may enhance the catalytic efficacy of spinel $CuCr_2O_4$ and Pd catalytic processes for the oxidation of carbon monoxide.[109] Using 0.100 g of catalyst, a temperature range of 30–450 °C, and a gas flow of 15 L $h^{-1}$, the study employed the temperature programmed surface reaction (TPSR) method to investigate a mixture of 1% CO, 20% $O_2$, and 79% $N_2$. The overall catalytic activity was considerably enhanced by distributing Pd NPs on $CuCr_2O_4$ NPs.[109] The core/shell NPs demonstrated promising catalytic activity for CO oxidation.[111] According to the researchers, HCOOH is more difficult to create than $CH_3OH$ due to its more complex chemical structure. The conversion of $CO_2$ into $CH_3OH$ is most likely the predominant reaction. Furthermore, the selectivity of HCOOH and $CH_3OH$ at 110–180 °C with calcined $Cu/CuCr_2O_4$ catalysts demonstrates alterations in the $CO_2$ conversion pathway.[116]

Shojaei *et al.* investigated the catalytic activity of $CuCr_2O_4$ and $CuCr_2O_4/TiO_2$ with an optimal chromite-to-$TiO_2$ molar ratio, catalyst amount, oxidant type and amount, and solvents. $CuCr_2O_4$–$TiO_2$ heterojunctions significantly enhance the catalytic activity in converting benzylic alcohols to aldehydes, particularly under microwave irradiation with *t*-BHP and $H_2O_2$ as oxidants.[146]

As seen in Scheme 10, homolytic cleavage of the $H_2O_2$ molecules gives two $^{\bullet}OH$ radicals. The resulting radicals combine with $Cr^{3+}$ and $Cu^{2+}$ ions on the surface of $CuCr_2O_4$, producing

**Table 5** Diverse organic transformations catalyzed by $CuCr_2O_4$ NPs

| Entry | Reaction | Ref. |
|---|---|---|
| 1 | 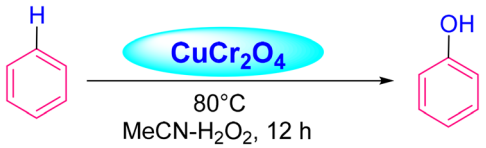  | 15, 74 and 78 |
| 2 | 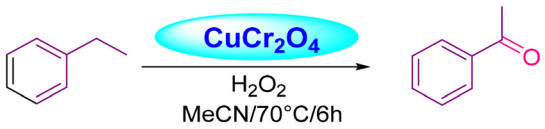  | 75 |
| 3 | 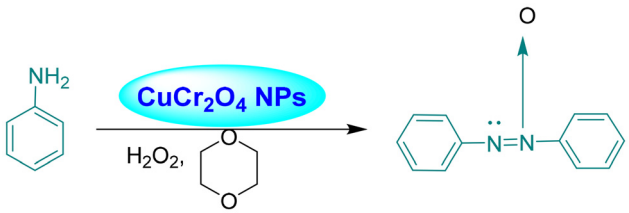  | 35 |
| 4 | 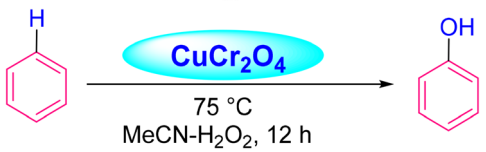  | 15 |
| 5 | 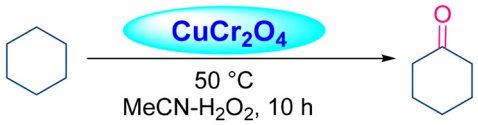  | 76 |
| 6 | 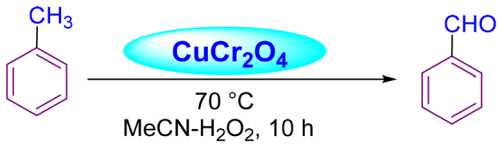  | 39 |

$Cu^{2+}$ and $Cu^{+}$ ions, respectively, as well as hydroperoxyl. The hydroperoxy radicals also further react with hydroxyl radicals on the surface, producing water and oxygen. Veratryl alcohol (VA) molecules are absorbed into the surface of $CuCr_2O_4$, generating metal–alkoxide intermediates and adsorbing hydrogen through O–H bond breakage. The surface O–H group is generated when the adsorbed hydrogen bonds with the surface lattice oxygen and coordinates with the carbon atom of the methyl group in the VA molecule. After activating the C–H bond in the β site, veratraldehyde and water are formed.[101]

Ghasemi *et al.* utilized $CuCr_2O_4$ NPs, along with a basic ionic liquid, to fabricate cyclopropanecarboxylic acids. They fabricated (±)-*trans*-2-phenylcyclopropanecarboxylic acid using *trans*-cinnamic acid as the starting material, along with the NPs. They utilized various solvent forms, but THF gave the optimal results (Scheme 11).[155]

Barman *et al.* presented a method for hydrogenating acetone using a catalyst. Firstly, chromite reversibly reacts with hydrogen, resulting in the formation of a decreased spinel and the release of copper as surface-bound particles. Acetone adsorbs onto $Cu^0$ atoms as π-complexes, getting electrons from the metal and a proton from chromite, resulting in negative charges. The oxidised copper returns to the spinel. A second proton is injected, and a proton from the acidic medium combines with the OH groups to produce a carbonium ion and water. This ion conducts electrophilic substitution with benzene to form cumene (Scheme 12).[138] As depicted in Fig. 18, the catalytic performance of $CuCr_2O_4$ NPs for various organic transformations was demonstrated.

Patil and colleagues studied the thermal decomposition of p-type nano-CuO and $CuCr_2O_4$ using AP. The DSC analysis concluded that the electrochemical technique produced NPs with better catalytic effects on HTD and AP. Nano-$CuCr_2O_4$ outperformed nano-CuO in reducing high-temperature decomposition by 118 °C at a 2 wt% concentration. Nano-CuO and $CuCr_2O_4$ produced significant heat emissions of 5.430 and 3.921 kJ $g^{-1}$, respectively.[156] A similar investigation was conducted by Shukri Ismael *et al.* They proposed that the transition metal $Cr^{3+}$ in $CuCr_2O_4$ exhibits hole conductivity due to its partially filled outermost d-orbitals. It rapidly takes electrons released by $ClO_4^-$, generating $Cr^{2+}$, which then migrates to the surface of the catalyst and reacts with $NH_4^+$ to generate

 

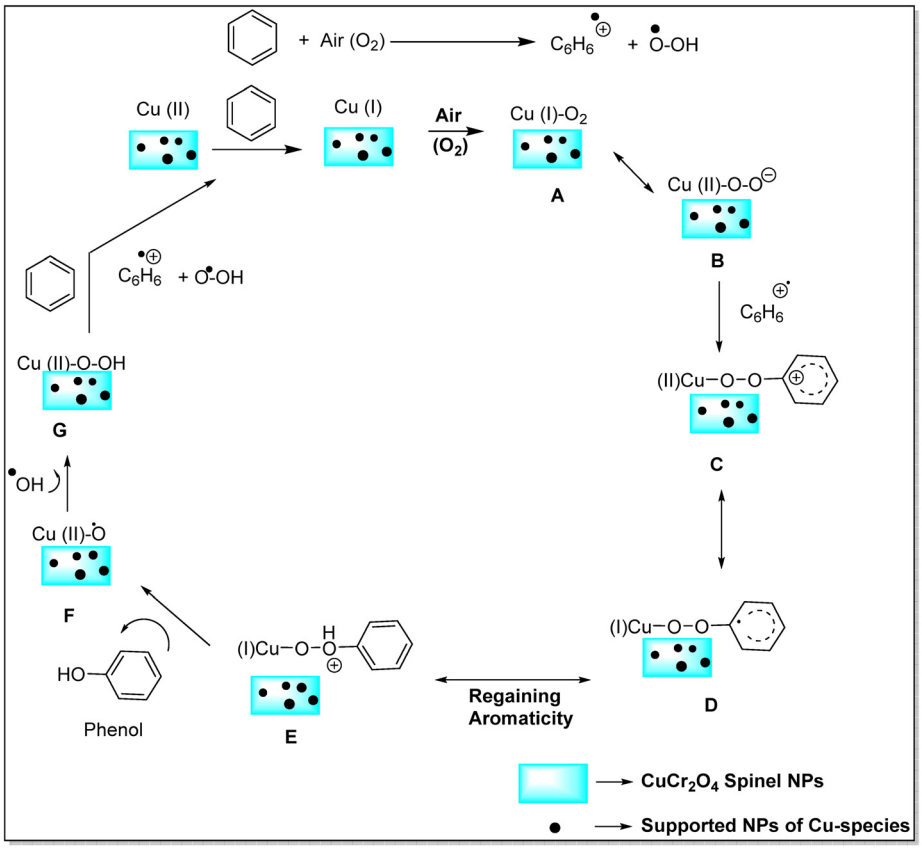


**Scheme 7** Possible process for phenol production over ultra-small Cu(II) based on $CuCr_2O_4$ NPs.[24]

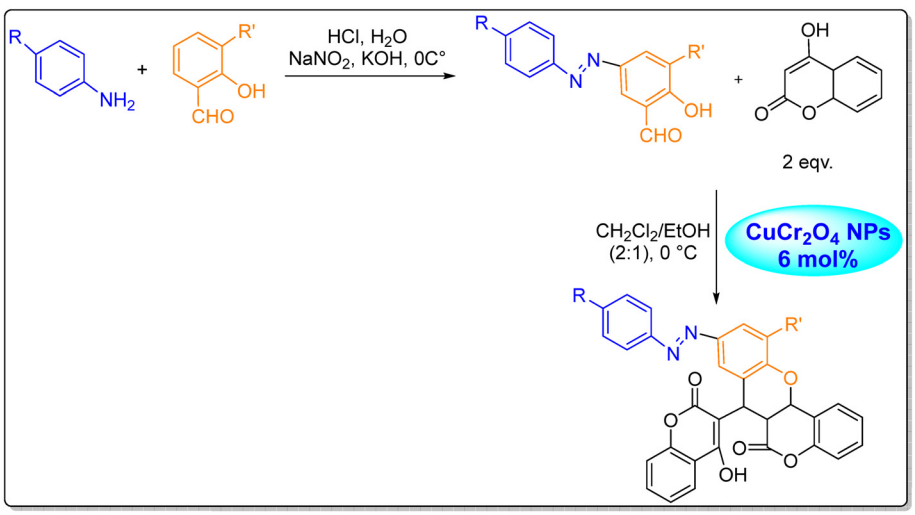


**Scheme 8** Formation of [1]benzopyran azo dyes catalyzed by $CuCr_2O_4$ NPs.[40]

ammonia and hydrogen atoms. As a result, the AP ion and its intermediate products can absorb electrons, accelerating the thermal deterioration of AP (Fig. 19).[79]

Ashraf *et al.* reported that copper chromite was efficiently incorporated into an ammonium nitrate (AN) matrix. The possible effect of copper chromite on the thermal behavior and decomposition enthalpy of AN was examined using TGA and DSC. Copper chromite had a considerable impact on the primary breakdown process of AN. AN decomposition was entirely transformed from a strong endothermic reaction ($+1554$ J $g^{-1}$) to a strong exothermic reaction ($-1625$ J $g^{-1}$).[93] Nano-$CuCr_2O_4$ noticeably enhances the degradation tempera-

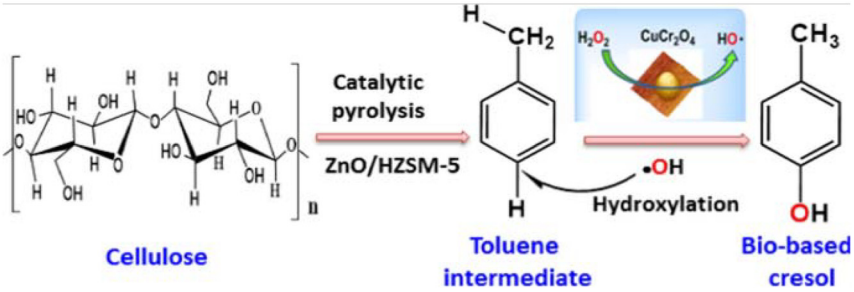


Fig. 17 $CuCr_2O_4$@MCM-41 catalyst used for the efficient catalytic pyrolysis of cellulose and catalytic oxidation.[153]

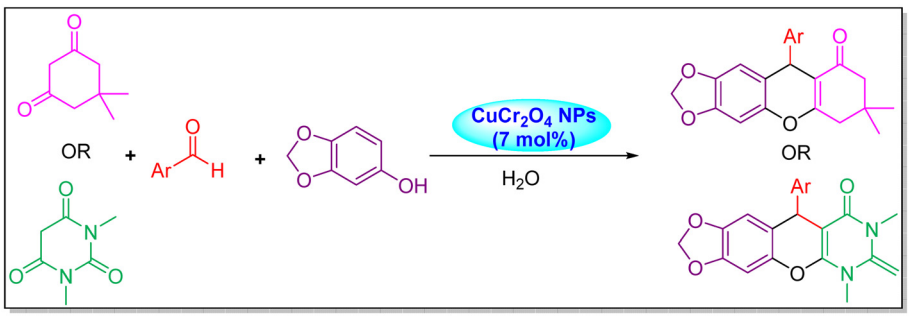


Scheme 9 Ultrasound-based, green, and sustainable method for xanthenone and chromenopyrimidinedione derivatives.[154]

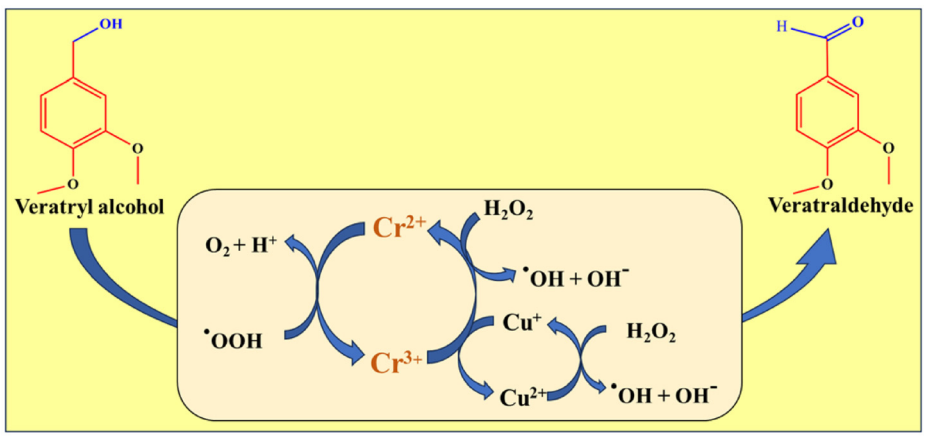


Scheme 10 Oxidation of VA to veratraldehyde.[101]

ture of AP/HTPB (ammonium perchlorate/hydroxy-terminated polybutadiene propellant) and AP/CMDB (ammonium perchlorate/composite modified double-base propellant), hence increasing the apparent heat of degradation. Furthermore, the burning rates of nano-$CuCr_2O_4$–AP/HTPB and nano-$CuCr_2O_4$–AP/CMDB propellants increased to 1.60 mm $s^{-1}$ and 3.23 mm $s^{-1}$, representing an increase of 28.3% and 26.3%, respectively.[19]

The TGA/DSC study verified that nano $CuCr_2O_4$ had a higher catalytic effect on ammonium dinitramide (AND) than nano CuO. Fuyao Chen and team believed that this could be because the catalytic activity of the two NPs differed for the preliminary decomposition product (AN) of ADN. They also conducted an ignition test on raw ADN and several copper-based catalyst/ADN composites. Raw ADN produced only a small amount of smoke at 200 ms, with the most intense decomposition time at 514 ms. The entire decomposition process of four distinct catalysts/ADN composites took less than 500 ms, indicating that copper-based catalysts can greatly facilitate ADN decomposition, and nano $CuCr_2O_4$ had a stronger catalytic effect on ADN decomposition than nano CuO. Moreover, researchers explored the adsorption capacity for $NH_3$ on the selected typical crystal face of nano $CuCr_2O_4$ (211) and the typical crystal faces of nano CuO (002) and (200). The

 

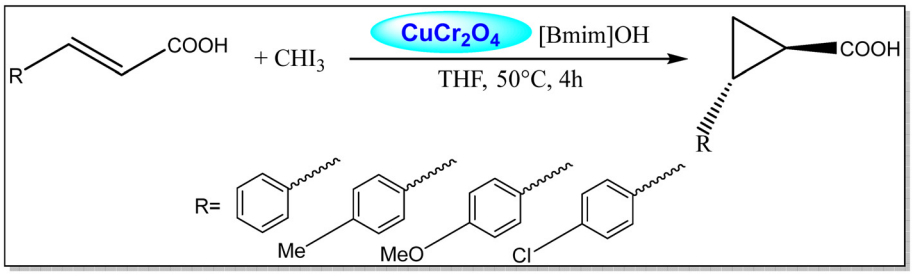


**Scheme 11** Reaction of functionalized *trans*-cinnamic acids *via* cyclopropanation.[155]

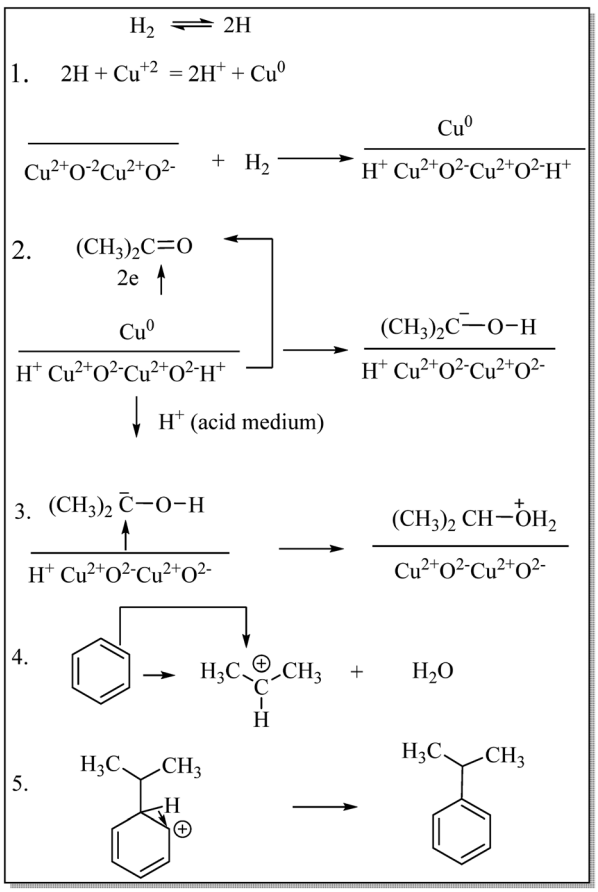


**Scheme 12** Mechanism of reductive isopropylation of benzene with acetone.[138]

(211) crystal face of nano $CuCr_2O_4$ showed the greatest negative value of $E_{ads}$ among the three models, implying that nano $CuCr_2O_4$ has stronger adsorption ability to the $NH_3$ molecule than that of nano CuO, which may be the primary explanation for the excellent catalytic performance of nano $CuCr_2O_4$ for AN (Fig. 20).[84]

Li *et al.* proposed that the efficient phase interaction between spinel $CuCr_2O_4$ and delafossite $CuCrO_2$ is present in Cu–Cr–O NCs. The catalyst with Cu/Cr of 0.7 shows excellent catalytic performance, a low-pressure exponent (0.43), and a high burning rate at all pressures.[57] Hosseini *et al.* found that adding $CuCr_2O_4$ NPs to pure AP decreases its decomposition temperature by 56 °C to 84 °C and increases the apparent heat released by 516 to 608 J $g^{-1}$.[50] Several studies have shown that AP decomposes at high temperatures.[85,90,142] $CuCr_2O_4$ NPs demonstrated remarkable catalytic activity on ultrafine AP, as revealed by the lowest high-temperature decomposition temperature and Gibbs free energy of the nano-$CuCr_2O_4$/ultrafine AP composite generated *via* ball milling for 6–12 h.[85]

Wang *et al.* investigated the catalytic effects of chromate NPs on the thermal decomposition of FAP and CL-20. The inclusion of chromate nanoparticles significantly decreased the decomposition temperature of FAP. Specifically, the produced $CuCr_2O_4$ NPs reduced the decomposition temperature of FAP by 57.7 °C, demonstrating that $CuCr_2O_4$ has significantly greater catalytic effectiveness than other chromates.[56] Viswanath *et al.* studied nano $CuCr_2O_4$ as a ballistic modifier in a typical solid rocket propellant (SRP) composition. According to the report, 17.5% CuO was required to achieve the desired phase for its application as a potential ballistic modifier. This excess CuO in $CuCr_2O_4$ enhances the burn rate of the typical SRP.[65] The addition of 5 wt% Cu–Cr–O–0.7$TiO_2$–rGO catalyst to AP considerably improved the thermal decomposition. Compared to the industrial catalyst (activated $CuCr_2O_4$), it showed a 133.61% greater solid composite propellant (SCP) burn rate. With 0.6% catalyst in AP, the burn rate increased from 4.866 mm $s^{-1}$ (pure AP) to 8.531 mm $s^{-1}$, exceeding that of the industrial catalyst of 6.385 mm $s^{-1}$ at 33 bar and displaying good ballistic performance.[145] The superior catalytic performance of metal-doped $CuCr_2O_4$ can be attributed to the presence of mixed active sites, including $Co^{2+}$ and $Ba^{2+}$ sites, as well as $Cu^{2+}$ and $Cr^{2+}$ sites. The mechanism indicates that the interaction between the catalyst and AP, which benefits from more active metal sites in the doped catalyst, demonstrates significant potential for AP decomposition. Furthermore, factors such as pore volume and the presence of active sites, as presented by doping, are also critical in influencing the catalytic performance.[95]

### 5.2. $CuCr_2O_4$ nanomaterials as photocatalysts

Environmental issues, notably water pollution, have received much attention in the last few years.[157] One of the main types of contaminants in wastewater is dyes.[158,159] Wastewater containing dyes has a significant impact on humans, animals,

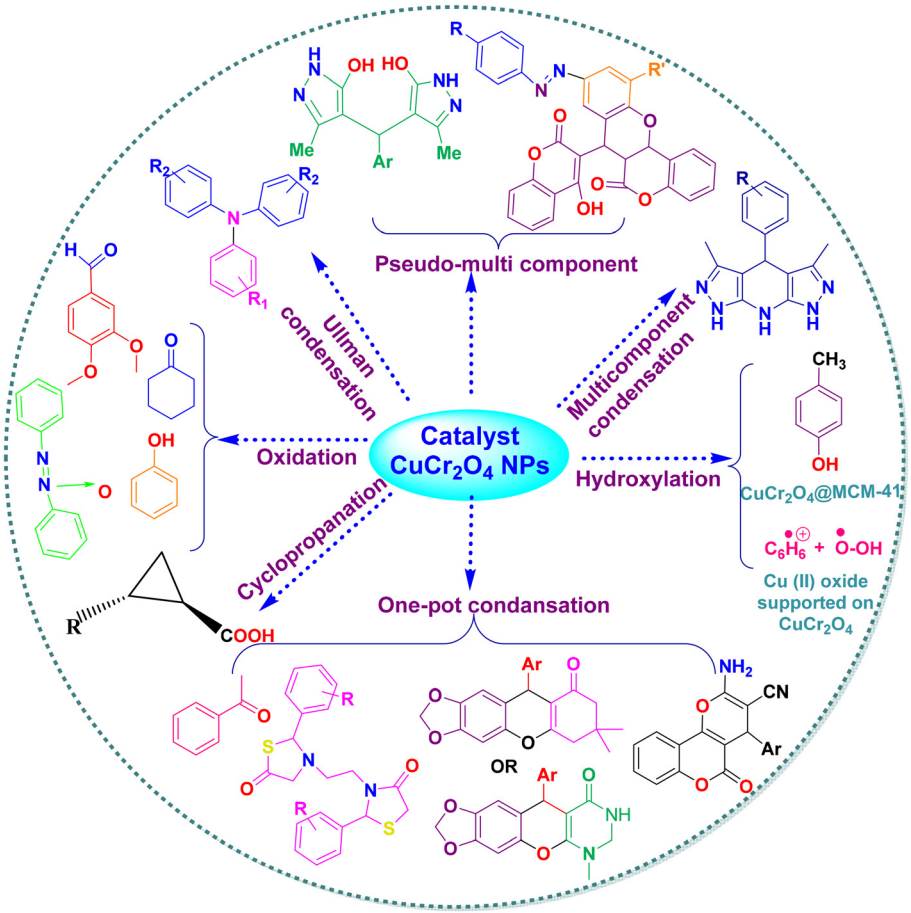


**Fig. 18** Catalytic activity of $CuCr_2O_4$ NPs for various organic transformations.

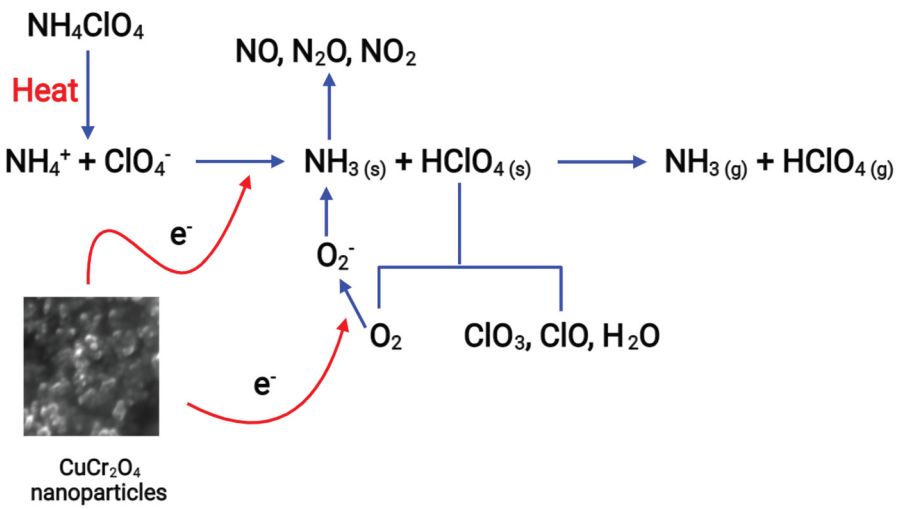


**Fig. 19** Schematic of the $CuCr_2O_4$ catalyst for AP decomposition.[79]

and the ecosystem because many dyes are not readily biodegradable and are highly toxic to the human body and aquatic life.[160,161] Photocatalytic activity has garnered significant attention recently due to its potential applications in environmental remediation, energy conversion, and sustainable chemical processes. This study investigated the effects of using a catalyst, without a catalyst, and with hydrogen peroxide ($H_2O_2$). Recent studies have illustrated that $H_2O_2$ is essential

 

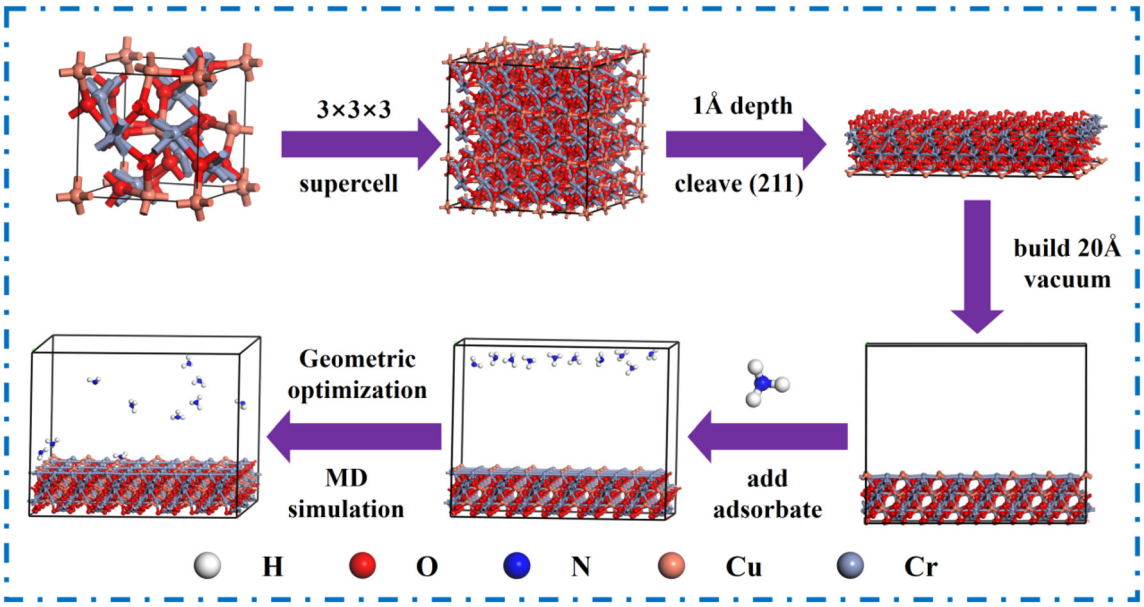


**Fig. 20** Schematic of the calculation and modeling process of adsorption heat between nano $CuCr_2O_4$ and $NH_3$.[84]

for photocatalytic activity and significantly accelerates the degradation rate.[162] Paul *et al.* proposed that $CuCr_2O_4$ NPs act as photocatalysts by absorbing solar energy, exciting electrons from the valence band (VB) to the conduction band (CB) and leaving holes in the VB. Dye is oxidized into innocuous chemicals by these holes, and hydroxyl radicals ($OH^{\bullet}$) are produced through the reduction of $H_2O_2$. The high bandgap energy and vast surface area of $CuCr_2O_4$ NPs promote the formation of electron–hole pairs, while inhibiting recombination, significantly increasing the photocatalytic efficiency.[23]

Pan *et al.* suggested that a pH of 9 plays a crucial role in the catalytic process of the samples. At greater concentrations, *p*-nitrophenol was successfully destroyed by 0.3 g $L^{-1}$ of $CuCr_2O_4$ calcined at 400 °C, with excellent reproducibility.[71] Yuan *et al.* observed photocatalytic activity using Rhodamine B (RhB), methyl orange (MO), and methylene blue. The absorption peaks of RhB (554 nm) and MB (664 nm) decreased significantly with an increase in the irradiation time and almost disappeared by 60 min. In contrast, the characteristic absorption peak of MO at 464 nm only slightly decreases with an increase in exposure time.[22]

Soleimani and team investigated the degradation of malachite green (MG) using $CuCr_2O_4$ and $Mn_{0.5}Cu_{0.5}Cr_2O_4$. The results show that $Mn_{0.5}Cu_{0.5}Cr_2O_4$ is more effective than $CuCr_2O_4$. In the photodegradation process, morphology and surface area significantly influence the efficiency. $CuCr_2O_4$ exhibits an agglomerated shape and a lower surface area, which results in reduced photodegradation capability. The $Mn_{0.5}Cu_{0.5}Cr_2O_4$ sample exhibits lower overall electronegativity than $CuCr_2O_4$, which affects its band gap and facilitates easier electron transitions between the conduction and valence bands.[80]

Fig. 21 illustrates the predicted photocatalytic mechanism for the decomposition of tartrazine azo dye. Under visible light

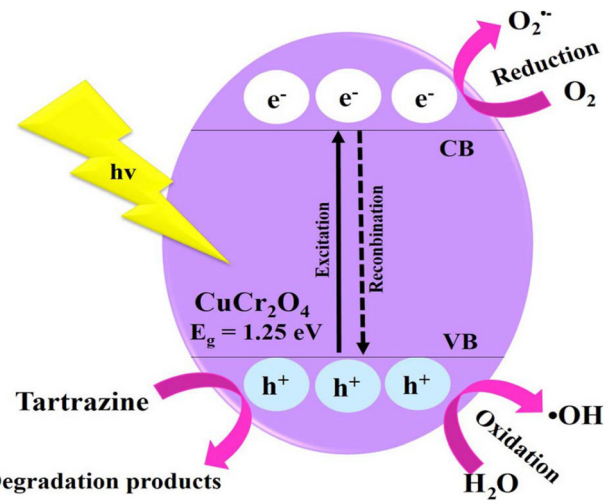


**Fig. 21** Proposed mechanism for photocatalytic degradation of a dye.[64]

(≥1.25 eV), $CuCr_2O_4$ generates electron–hole pairs (eqn (11)). Electrons react with oxygen to form $^{\bullet}O_2^-$ (eqn (12)). At the same time, holes in the valence band interact with $H_2O$ to produce $^{\bullet}OH$ radicals (eqn (13)). These reactive species, especially $^{\bullet}OH$ and $h^+$, break down the azo dye into $CO_2$, $H_2O$, phenols, aromatic amines, and acids such as oxalic, tartaric, and malic (eqn (14)).[64]

$$CuCr_2O_4 + \text{visible light} \rightarrow e^-CB + h^+VB \quad (11)$$

$$e^-CB + O_2 \rightarrow {}^{\bullet}O_2^- \quad (12)$$

$$h^+VB + H_2O \rightarrow {}^{\bullet}OH \quad (13)$$

$$\text{Tartrazine} + {}^{\bullet}OH + h^{+}VB + {}^{\bullet}O_2^{-} \rightarrow CO_2 + H_2O + \text{products of degradation} \quad (14)$$

Peymanfar *et al.* proposed that photocatalytic degradation under both visible and dark light conditions performed better than expected, suggesting that the capped $CuCr_2O_4$ structures and the produced $CuCr_2O_4$ function as photocatalytic materials rather than adsorbents.[51]

The impacts of pH, catalyst dosage, and initial concentration on photocatalytic decomposition were examined by Benrighi *et al.* They found that dye degradation was significantly influenced by the pH of the solution, with the best degradation taking place at pH values close to 4.0. Dye degradation decreases significantly as the pH increases from 4.0 to 10. This reduction can be related to the negative charge that anionic dyes acquire at higher pH values. It might impede degradation by repelling them from the surface of the photocatalyst due to charge repulsion.[52]

Han *et al.* examined the photocatalytic degradation of Congo red dye and antibiotics, including TCH, metformin hydrochloride (MFH), oxycline hydrochloride, and naproxen sodium (NPS). $CuAl_2O_4$ oxides reveal high photocatalytic performance in TCH and OCH, while MFH and NPS exhibit poor photocatalytic activity.[86] The electronic band structure (Fig. 22a and c) and density of states (DOS) of nanomaterials were computed using the DFT function. The Fermi values of $CuCr_2O_4$ and $BiI_3O_9$ were 4.32 and 1.41 eV, according to Fig. 22b and d, respectively. The DOS analysis of pure $CuCr_2O_4$ and $BiI_3O_9$ revealed electron excitation at different orbitals. $CuCr_2O_4$–$BiI_3O_9$-10% NCs outperformed other concentrations and pure $CuCr_2O_4$ and $BiI_3O_9$ NPs in terms of photocatalytic activity. The efficient photodegradation is attributed to the effective generation of heterojunctions, improved charge carrier separation and migration, and a wide surface area. $OH^{\bullet}$ significantly contributed to cefixime (CEF) deterioration. The proposed Z-scheme is effective in photodegrading CEF.[45]

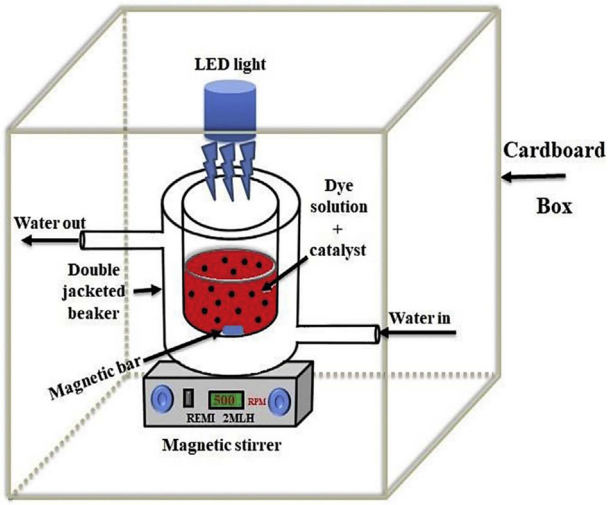


Fig. 23 Layout of the dye degradation setup.[112]

Ghorai *et al.* studied the photocatalytic performance of a $CuCr_2O_4$/BiOBr nanocomposite for degrading RhB and tetracycline hydrochloride (TC-HCl) under household LED light, as shown in Fig. 23.[112]

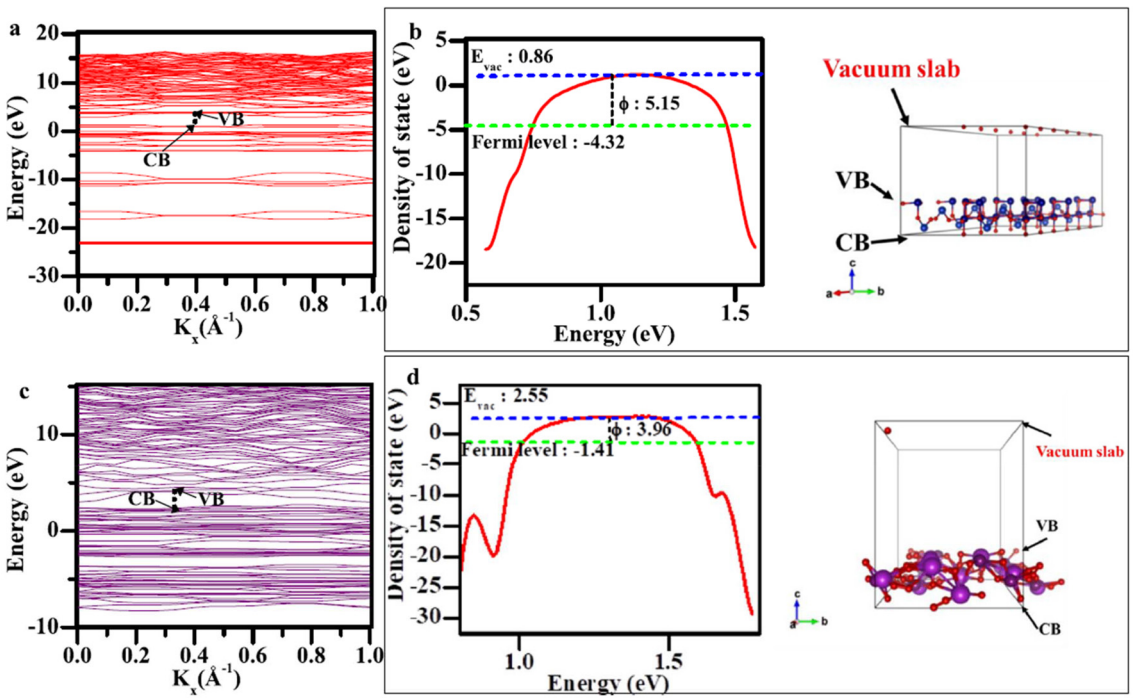


Fig. 22 Electronic band structure, work function, and atomic arrangement of $CuCr_2O_4$ (a and b) and $BiI_3O_9$ NPs (c and d).[45]

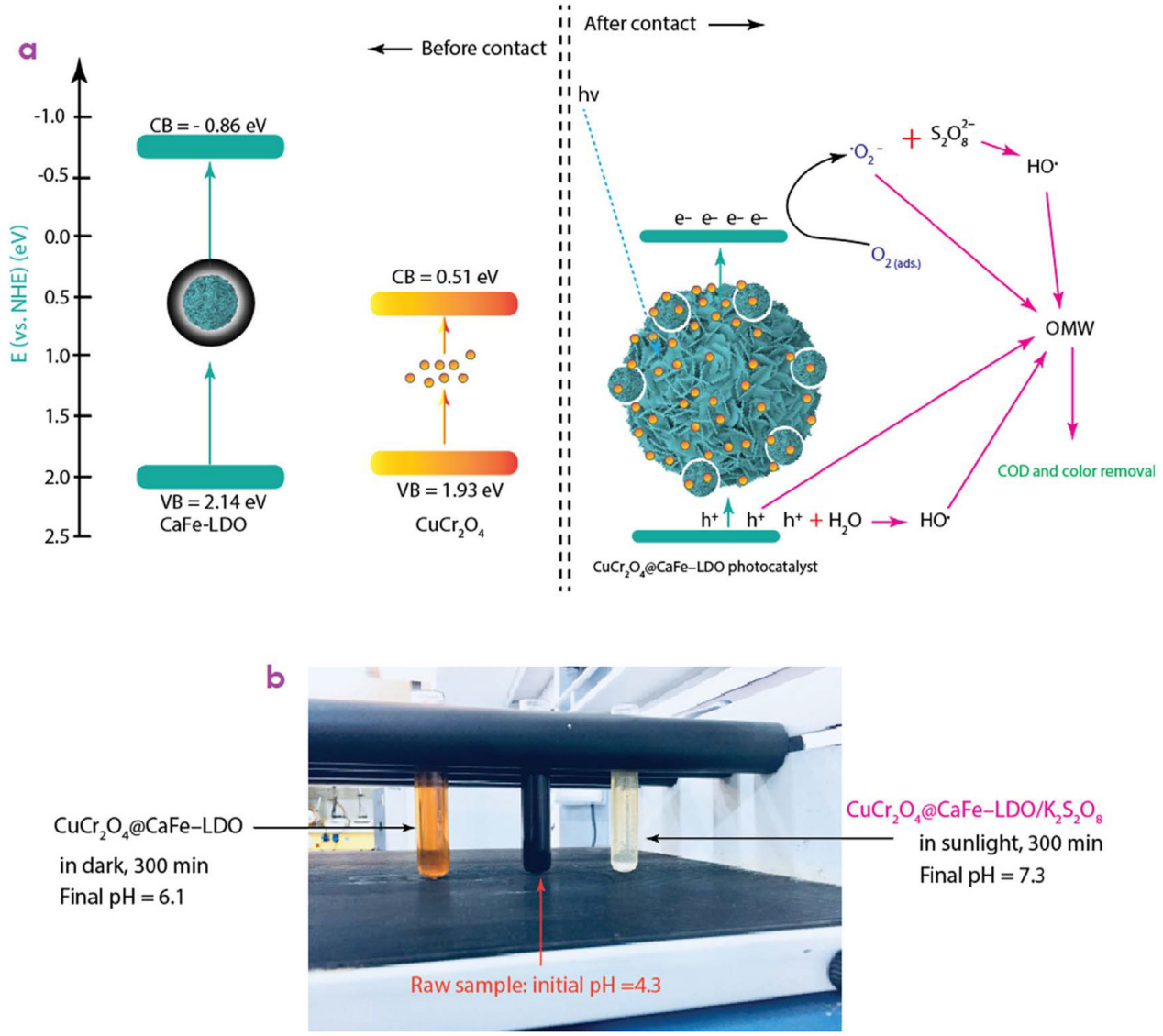


**Fig. 24** Probable reaction pathway of the $CuCr_2O_4$@CaFe-LDO/$K_2S_2O_8$/sunlight system. (b) Illustration of the catalyst performance under both dark and light conditions.[113]

The $BiVO_4$–$CuCr_2O_4$ (1 : 0.25) nanocomposite exhibits ~90% photocatalytic efficiency for MB dye degradation under visible light, which increases with PANI addition. This enhancement is attributed to the improved charge separation of electron–hole pairs, further strengthened by the incorporation of PANI.[141]

According to Oladipo *et al.*, 1.0 g $CuCr_2O_4$@CaFe-LDO removed 66% COD without an oxidant after 300 min in the dark. However, after 180 min of reaction, the $CuCr_2O_4$@CaFe-LDO/$K_2S_2O_8$/sunlight system removed ~99% and 98.3% COD and colour, respectively. The crude OMW contained seven phenolic compounds, the most abundant of which were hydroxy tyrosol (76.84%) and tyrosol (15.14%) [Fig. 24].[113] Without an oxidant, $CuCr_2O_4$@CaFe-LDO degraded phenol by 54.8% after 4 h in the dark. Within 40 min, the deterioration reached 90% when exposed to sunshine and 0.05 M $K_2S_2O_8$. After 120 min, the $CuCr_2O_4$@CaFe-LDO/$K_2S_2O_8$ system, with UV assistance, achieved 99% phenolic degradation, 95.1% COD removal, and 84.6% BOD removal.[114]

It was discovered that the 10% $CuCr_2O_4$–$CeO_2$ nanocomposite sample exhibited a remarkable photo-Fenton performance. Tests using coumarin fluorescence probes and radical trapping verified that $^{\cdot}OH$ is the main factor causing RhB degradation. Visible LED light promotes the production of $^{\cdot}OH$ during the Fenton-like reaction more efficiently than under dark conditions. The favorable redox reaction between $Ce^{4+}/Ce^{3+}$ and $Cu^{2+}/Cu^{+}$ couples triggers a dark Fenton-like reaction. However, the low-molecular-weight compounds produced during degradation accumulate on the active sites of the catalyst, reducing its reusability. Fig. 25 illustrates the photo-Fenton reaction mechanisms.[115]

The degradation of MO and MB dyes followed a pseudo-first-order kinetic model.[127] Mageshwari *et al.* analyzed the time-

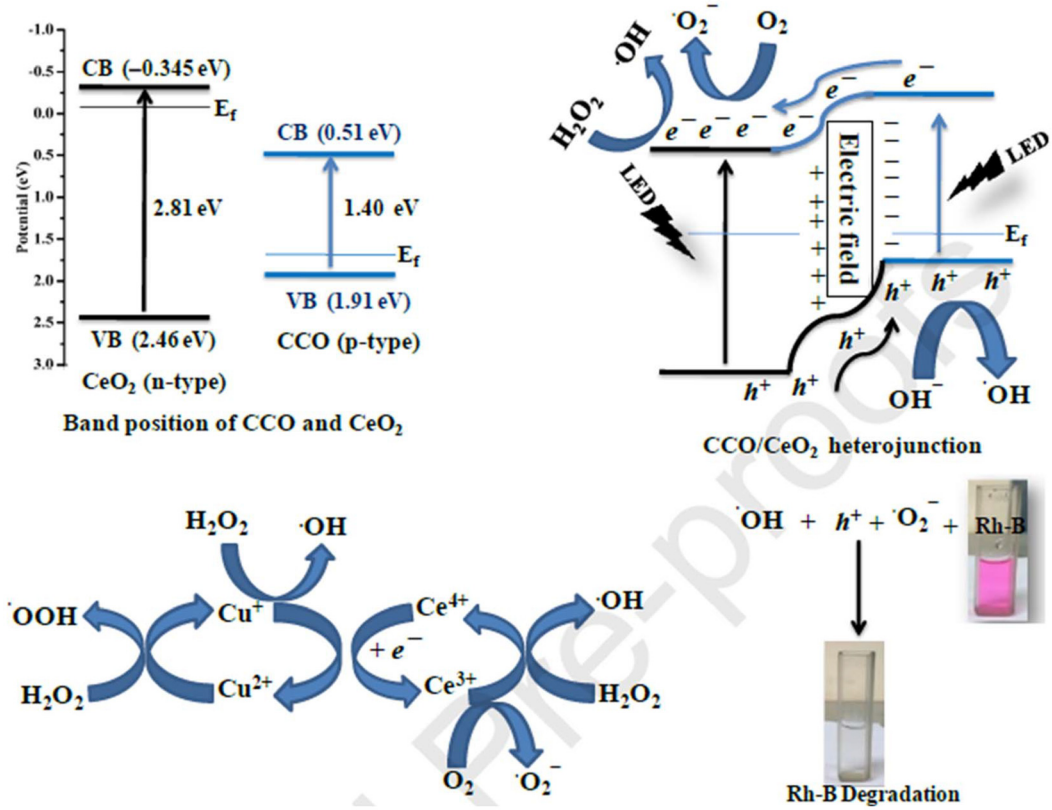


Fig. 25 Photo Fenton-like reaction process of $CuCr_2O_4$–$CeO_2$ NCs.[115]

dependent UV-vis absorption spectra of MO and MB in the presence of CuO and CuO–$CuCr_2O_4$ (20% $Cr^{3+}$). After 270 min with CuO and 145 min with CuO–$CuCr_2O_4$, the MO absorption peak at 464 nm, which was associated with the azo (–N=N–) bond, disappeared. Likewise, after 360 min with CuO and 180 min with CuO–$CuCr_2O_4$, the MB peak at 665 nm disappeared. The time-dependent UV–vis absorption spectra in Fig. 26 demonstrate the effective degradation of MO and MB dyes by the CuO and CuO–$CuCr_2O_4$ samples. The dyes gradually lost color, indicating their complete degradation. In the case of MO, the peak at 464 nm disappeared after 270 min with CuO and 145 min with CuO–$CuCr_2O_4$. In the case of MB, the 665 nm peak vanished after 360 min with CuO and 180 min with CuO–$CuCr_2O_4$, indicating that the CuO–$CuCr_2O_4$ sample exhibited superior photocatalytic activity compared to pure CuO.[26] The photocatalytic efficacy of g-$C_3N_4$-NS/$CuCr_2O_4$ NCs was evaluated by degrading MB and RhB dyes and phenol under visible light. The nanocomposite performed best with a 10 wt% $CuCr_2O_4$ loading.[119]

Mohamed *et al.* investigated $CuCr_2O_4$–g-$C_3N_4$ photocatalysts for photocatalytic hydrogen generation utilizing glycerol under visible light illumination (Fig. 27). Their findings revealed that the $CuCr_2O_4$ content in the heterojunction had a substantial impact on photocatalytic performance, with a 3 wt% composition being the optimal. At this ideal level, the 3 wt% $CuCr_2O_4$–g-$C_3N_4$ heterojunctions produced thirty-times more hydrogen from glycerol than pure g-$C_3N_4$.[117]

According to the results, when exposed to simulated sunlight, pure $CuCr_2O_4$ or $TiO_2$ showed a weak photocatalytic performance for generating hydrogen from an aqueous oxalic acid solution. However, $CuCr_2O_4$/$TiO_2$ heterojunction coupling showed noticeably higher photocatalytic activity. A mass concentration of 0.8 g $L^{-1}$ exhibited promising hydrogen evolution capability when calcined at 500 °C.[144] Baoum *et al.* investigated the bandgap energy of $CuCr_2O_4$ and PANI@$CuCr_2O_4$ composites using UV-vis spectroscopy. The bandgap values for pure $CuCr_2O_4$ and 0.02%, 0.04%, 0.06%, and 0.08% PANI@$CuCr_2O_4$ were 2.12, 2.00, 1.92, 1.73, and 1.72 eV, respectively. The outcomes indicate that the incorporation of PANI reduces the bandgap, thereby enhancing the photocatalytic activity of the nanocomposites.[123] Daimalah *et al.* demonstrated the significance of pH and dose in photocatalytic activity. An increase in catalyst dosage resulted in a higher abatement rate. Furthermore, as the pH decreased from 9 to 3.5, the cefixime (CFX) removal efficiency improved from 30% to 94%.[131]

Ghorai *et al.* investigated the photocatalytic activity of dyes and antibiotics, yielding promising results. As demonstrated in Fig. 28, radical trapping experiments revealed that in the PFL reaction, dye abatement decreased significantly with IPA and $AgNO_3$, confirming that ·OH radical and excited electrons are the main reactive species, respectively. $Na_2EDTA$ and BQ had minimal effects, indicating the limited roles of

 

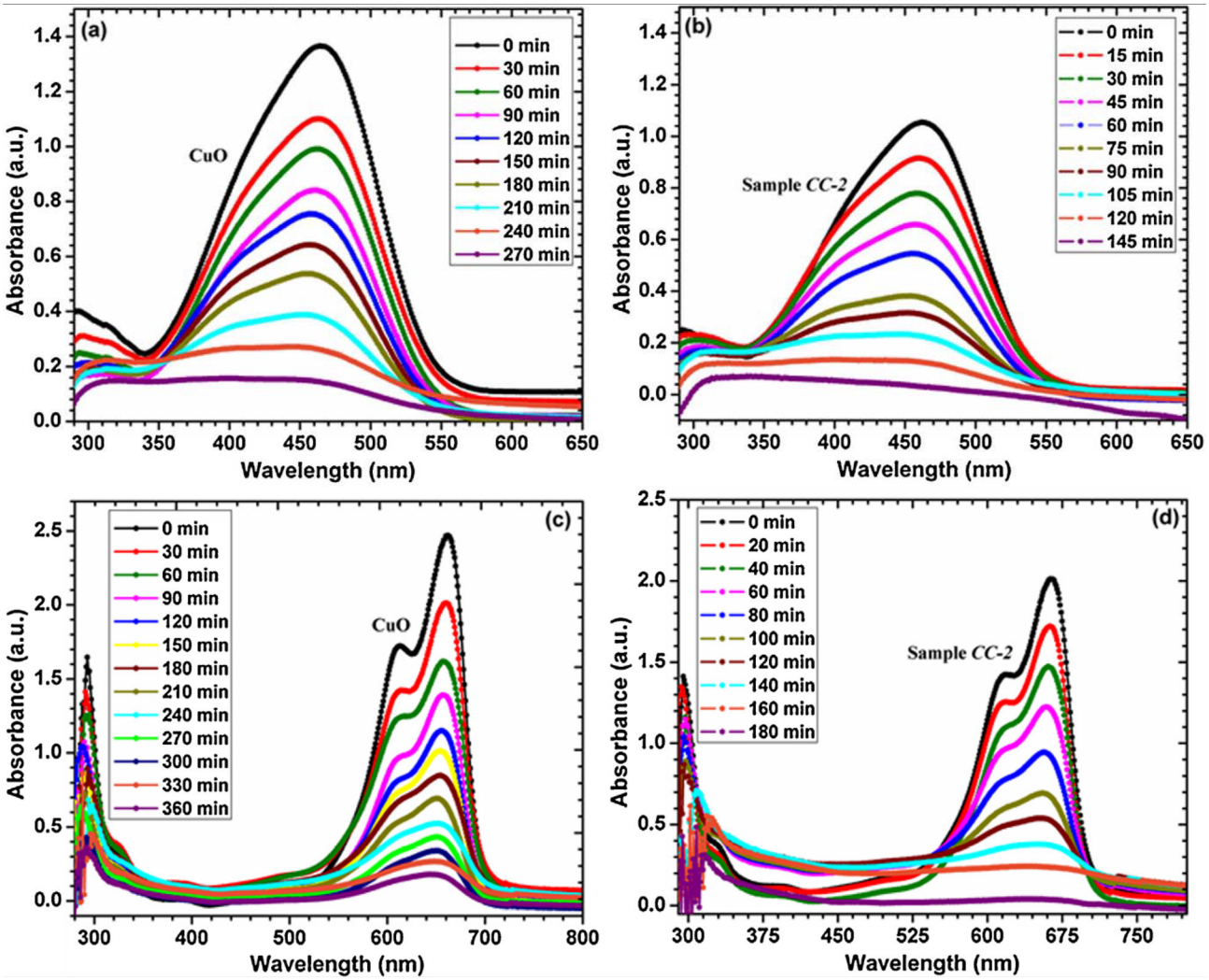


**Fig. 26** Time -dependent UV–vis absorption spectra of (a and b) MO and (c and d) MB dye solutions in the presence of CuO and CuO–$CuCr_2O_4$ (20% $Cr^{3+}$ concentration) samples under UV irradiation.[26]

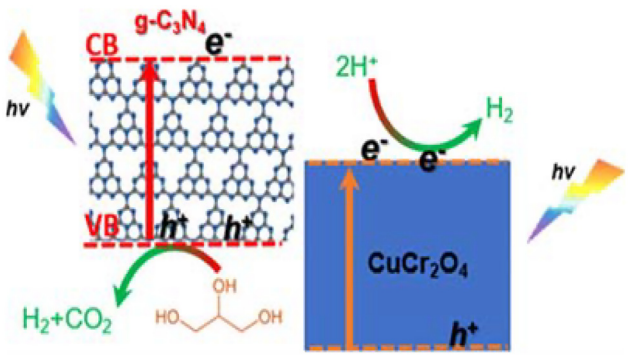


**Fig. 27** Proposed mechanism for $H_2$ gas generation using the $CuCr_2O_4$–g-$C_3N_4$ heterojunction.[117]

holes and superoxide species, respectively. In the DFL reaction, the degradation activity decreased significantly in the presence of IPA.[48]

Sivaranjani *et al.* stated that increasing the number of photons per unit area with an increase in light intensity enhances the deterioration. Furthermore, the photocatalytic process exhibits a positive relationship with pH, with the highest degradation occurring at a pH of 7.0. Degradation is reported to diminish above pH 7.0 because of the reaction between the $^{\bullet}OH$ and $h^+$ generated by the semiconductor. Compared to other anions such as $Cl^-$, $HCO_3^-$, $CH_3^-$, and $NO_3^-$, the presence of $SO_4^{2-}$ anions was considered to cause the most deterioration. The bonding behavior of the complexes and the contribution of molecular orbitals (HOMO and LUMO) were predicted by DOS plots.[118]

As shown in Fig. 29, the alizarine red dye molecule absorbs light energy, exciting electrons in $V_2O_5$/$CuCr_2O_4$–MCM-41, which generates ROS, such as $^{\bullet}OH$. These $^{\bullet}OH$ groups interact with alizarine red molecules, breaking the dye into smaller, non-toxic components such as $CO_2$, $SO_4^{2-}$, and $H_2O$.[135]

Ramezanalizadeha *et al.* highlighted the synergistic involvement of La in improving the photocatalytic activity. Notably, $CuCrLaO_4$ demonstrated remarkable degradation of both RhB

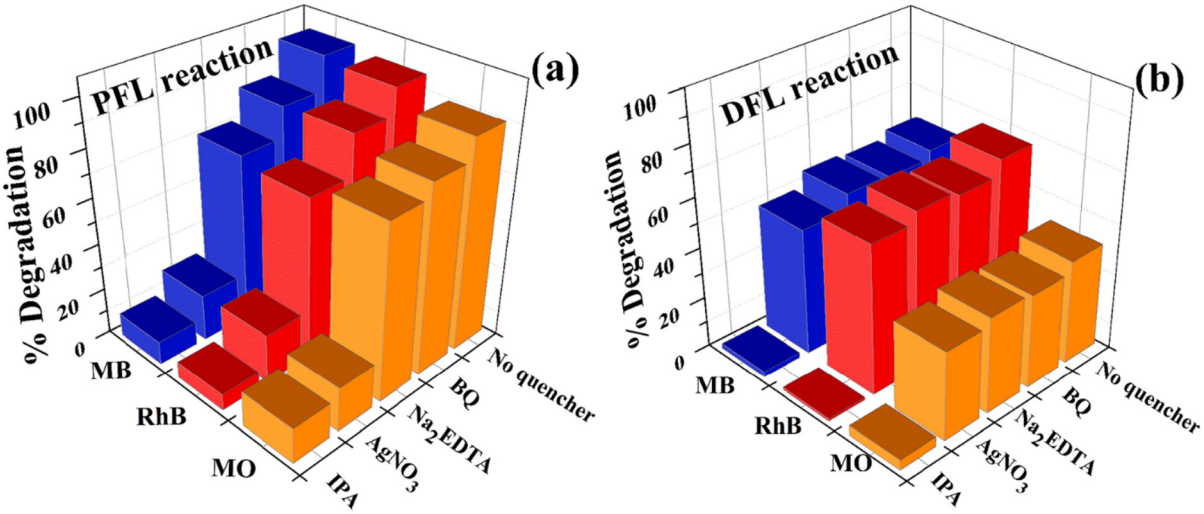


Fig. 28 Impact of various radical quenchers on the PFL and DFL activity of the 100% $CuCr_2O_4/TiO_2$ nanocomposite for MB, RhB, and MO degradation.[48]

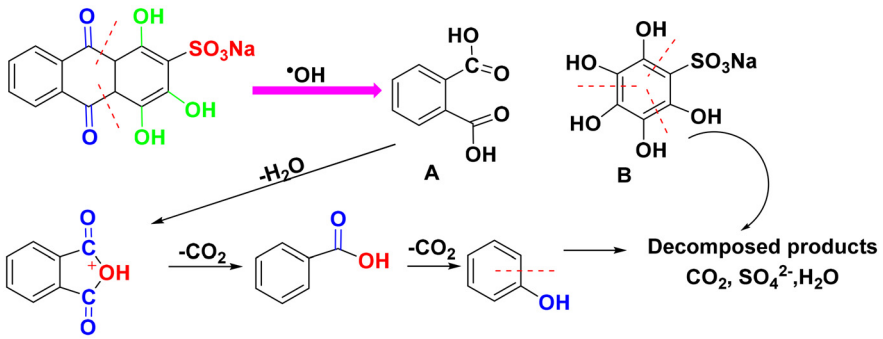


Fig. 29 Plausible mechanism for the decomposition of Alizarin Red dye.[135]

and MO dye.[100] Hosseini *et al.* investigated the photocatalytic activity of $CuCr_2O_4$ against *p*-nitrophenol contamination. The CuO content of the samples considerably influenced their photocatalytic performance. The findings demonstrate that the Cu/Cr molar ratio has a significant impact on the photocatalytic efficiency of the samples.[136]

Al-Wasidi *et al.* studied the degradation of Acid Orange 7 dye using a $CuCr_2O_4$ photocatalyst (Fig. 30). Under visible light, the copper chromite photocatalyst absorbs energy equivalent to or greater than its band gap, resulting in electron–hole ($e^-/h^+$) pairs on its surface. The photogenerated electrons combine with adsorbed oxygen molecules to form superoxide radicals ($O_2^{\bullet-}$), and holes react with water molecules to produce hydroxyl radicals ($^{\bullet}OH$). These reactive species, particularly hydroxyl radicals and holes, effectively breakdown Acid Orange 7 dye into $CO_2$, $H_2O$, or other byproducts.[81]

Abbasi *et al.* found that $CuCr_2O_4$ and $CuCr_2O_4$/Ag nanostructures effectively degraded MO, MB, and RhB dyes. The researchers found that using leucine-capped $CuCr_2O_4$/Ag (3%) nanostructures instead of $CuCr_2O_4$ NPs improved the RhB dye degradation efficiency from 76% to 91%. Their study also highlighted the role of pH in the breakdown process. As shown in Fig. 31, the surface of the particles under acidic conditions exhibits a significant positive charge, which inhibits cationic dye adsorption due to electrostatic repulsion. The best degrading efficiency for RhB was reached under neutral circumstances. The catalytic efficiency of leucine-capped $CuCr_2O_4$/Ag (3%) for RhB degradation was 91% at pH 7 compared to 73% at pH 5.[140]

Furthermore, Fig. 32 and Table 6 describe the decomposition of diverse dyes and antibiotics in detail using $CuCr_2O_4$ NPs.

### 5.3. Energy storage application of $CuCr_2O_4$ nanomaterials

**5.3.1. Supercapacitor.** Supercapacitors are among the best electrical energy storage technologies due to their extended lifespan, sustainability, high-temperature performance, fast charging capability, and long cycle life. The three primary types of supercapacitors are electrochemical double-layer capacitors (EDLCs), pseudocapacitors, and hybrid supercapacitors (HSC).[163] A hybrid supercapacitor is an energy storage device that combines the features of EDLC and pseudo-

 

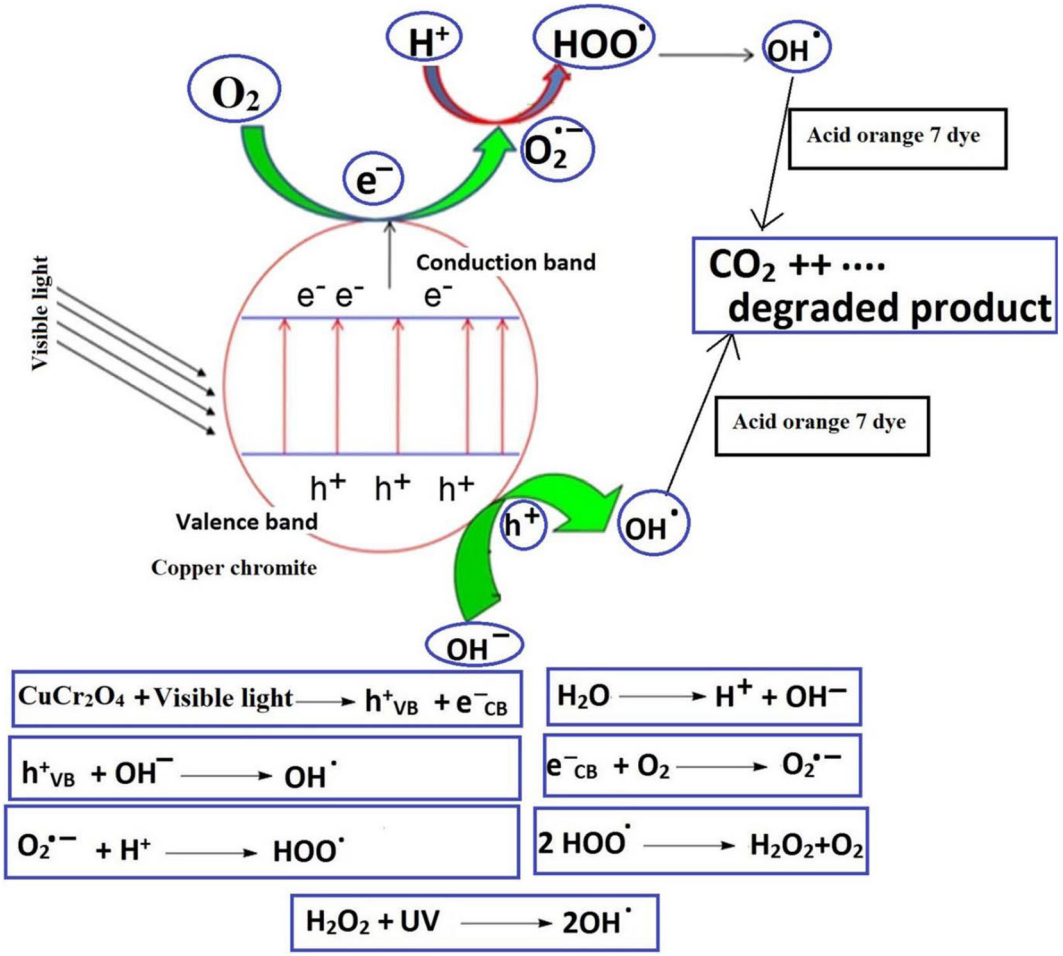


**Fig. 30** Suggested approach, utilizing $CuCr_2O_4$ as a photocatalyst for the degradation of Acid Orange 7 dye.[81]

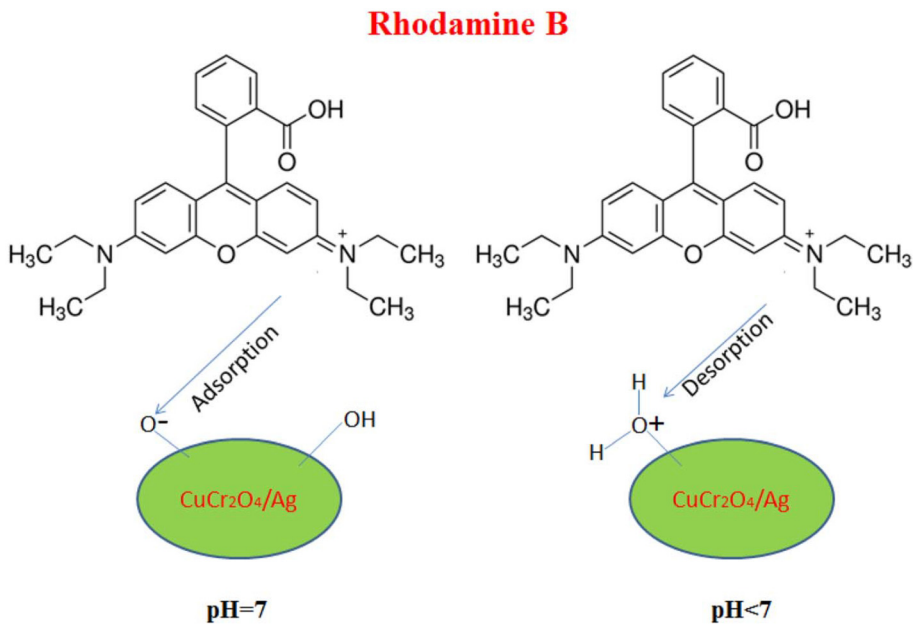


**Fig. 31** Effect of pH on the RhB adsorption and desorption on the $CuCr_2O_4$/Ag nanostructure surfaces.[140]

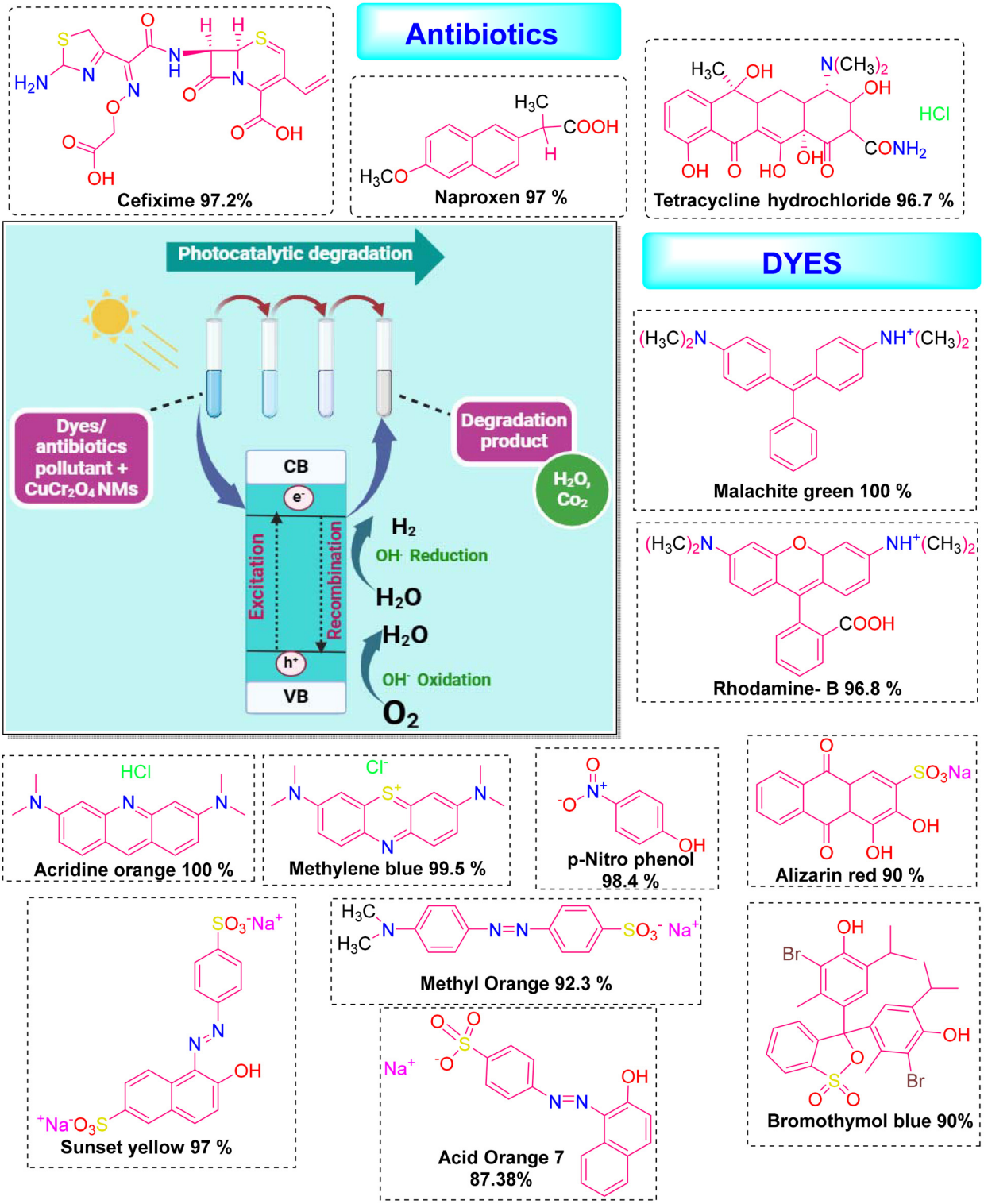


Fig. 32 Illustration of the photocatalytic decomposition of various dyes and antibiotics employing pristine $CuCr_2O_4$, metal-doped $CuCr_2O_4$, and their nanocomposites.

capacitors. Shayeh *et al.* found that incorporating $CuCr_2O_4$ NPs into polypyrrole (Ppy) films increases their active surface area and charge transfer sites, leading to improved polymeric electrode stability and capacitance after 1200 cycles (Fig. 33).[47]

Rajeswari *et al.* examined the photovoltaic efficiency of different materials. Among them, $CuCr_2O_4$ had the lowest photovoltaic efficiency, lowest fill factor, and highest short-circuit photocurrent density. In contrast, La-doped oxides had

 

**Table 6** Overview of the application of $CuCr_2O_4$ NPs in the decomposition of various dyes/antibiotics

| Dye/antibiotic | Dye conc. | $CuCr_2O_4$ NPs loaded | Band gap | Light source | Degradation (%) | Degradation time (h) | Cycles | Rate constant for degradation ($min^{-1}$) | Ref. |
|---|---|---|---|---|---|---|---|---|---|
| *p*-Nitrophenol | 20 mg $l^{-1}$ | 100 mg | — | Visible light | 400 °C-98.4<br>450 °C-95.7<br>500 °C-86.8<br>550 °C-8512<br>600 °C-77.2 | 180 | 10 | — | 71 |
| MB | 10 mg $L^{-1}$ | 10 mg | 1.4 | Solar light | 80.6 | 18 | 5 | 0.132 | 23 |
| MO | | | | | 92.3 | 18 | | 0.147 | |
| RhB | | | | | 93.6 | 12 | | 0.2095 | |
| RhB | — | 20 mg (600 °C) | — | Visible light | 96.8 | 60 | 5 | — | 22 |
| MB | | | | | 99.5 | | | | |
| MO | | | | | 14 | | | | |
| MG ($Mn_{0.5}Cu_{0.5}Cr_2O_4$) | 10 ppm | 40 mg | 1.37 | Solar light | 100 | 40 | 3 | — | 80 |
| Tartrazine azo | — | 0.5 g | 1.25 | Visible light | 99.6 | 120 | 4 | 0.04578 | 64 |
| MB $CuCr_2O_4$ | 10 mg $L^{-1}$ | 0.03 g | 2.4 | Visible light | 98 | 90 | 5 | — | 51 |
| MO capped-$CuCr_2O_4$ | | | | | 87 capped-$CuCr_2O_4$ | 100 | 5 | | |
| Sunset yellow | 0.8 g $L^{-1}$ | 10 ppm | 0.9 | Visible light | 97 | 4 h | 4 | 0.01685 | 52 |
| CEF | — | — | 1.83 $CuCr_2O_4$<br>2.31 $BiI_3O_9$ | Visible light | 97.2 | 200 | 6 | 0.0128 | 45 |
| RhB | 10 mg $L^{-1}$ | 25 mg | 1.48 $CuCr_2O_4$ | Led light | 95.97 | 15 | 4 | 0.22427 | 112 |
| TC-HCl | 10 ppm | 25 mg | 2.62 BiOBr | | 96.7 | 300 | | | |
| RhB | 10 ppm | 50 mg | 2.81 $CuCr_2O_4$ | Visible LED | 99 | 15 | — | — | 115 |
| MB | | | 1.40 $CeO_2$ | light | 85 | | | | |
| MO | | | | | 60 | | | | |
| MB | 2 mg $L^{-1}$ | 0.2 g | 2.64 | Visible light | 84 | 180 | 3 | 0.0052 | 127 |
| MO | | | | | 57 | | | 0.0025 | |
| MB | 15 mg $L^{-1}$ | 50 mg | 1.40 $CuCr_2O_4$ | UV light | 97.16 | 145 | | 0.01803 | 26 |
| MO | 15 mg $L^{-1}$ | | 1.63 CuO | | 98.16 | 180 | | 0.02211 | |
| RhB | $2.50 \times 10^{-5}$ M | — | 1.4 $CuCr_2O_4$<br>2.7 g-$C_3N_4$ | Visible light | 98.8 | 210 | 5 | — | 119 |
| Acridine orange dye | — | 2.0 g $L^{-1}$ | 1.73 | Visible light | 100 | 40 | 5 | — | 123 |
| CFX | 10 ppm | 1 g $L^{-1}$ | 0.93 | Visible light | $CuCr_2O_4$-PS-94<br>$CuCr_2O_4$-60 (pH-3.5) | 180 | 4 | — | 131 |
| Crystal violet | 15 mg $L^{-1}$ | 1 mg $mL^{-1}$ | 1.39-$CuCr_2O_4$<br>3.07-$SnO_2$ | Sun light | — | 90 | 0.012 | — | 124 |
| MB | 10 ppm | 50 mg | 1.4-$CuCr_2O_4$ | LED light | 99.2 | 15 | — | 0.30794 | 48 |
| RhB | | | 3.1-$TiO_2$ | | 97.2 | | | 0.24358 | |
| MO | | | | | 89.6 | | | 0.14943 | |
| TC-HCl | | | | | 99 (PFL)<br>58 (DFL) | 15 | | | |
| Norfloxacin (NORF) | | | | | 97 (PFL)<br>74 (DFL) | 75 | | | |
| MG | — | 30 mg | 6.48 | Visible light | 86 | — | — | 0.9855 | 118 |
| AR | — | 40 mg | 1.3 | Visible light | 90 | 60 | — | — | 135 |
| BTB | | | | | 90 | 60 | | | |
| RhB | 10 mg $l^{-1}$ (pH = 7) | 20 mg | 2.5, 2.6 and 2.65 | LED visible light | 98 | 90 | 6 | — | 100 |
| MO | | | | | 99 | 60 | | | |
| 4-NP | 20 ppm | 25 mg | 1.4 | UV light | 97.2 | 100 | — | 0.0330 | 136 |
| Acid orange 7 | 100 mg $L^{-1}$<br>25 mg $L^{-1}$<br>25 mg $L^{-1}$ | 0.10 g | $CuCr_2O_4$-1.25<br>$CuCr_2O_4$–citric acid-1.88<br>$CuCr_2O_4$–tartaric acid-1.92 | Visible light | 87.38<br>96.52<br>98.81 | 40 min | — | 0.053<br>0.083<br>0.115 | 81 |
| RhB | 10 ppm | 0.04 g | —<br>3.05<br>— | UV light | Leucine–$CuCr_2O_4$/Ag (1%)-81<br>Leucine–$CuCr_2O_4$/Ag (3%)-87<br>Leucine–$CuCr_2O_4$/Ag (5%)-91% | 60 min | — | — | 140 |

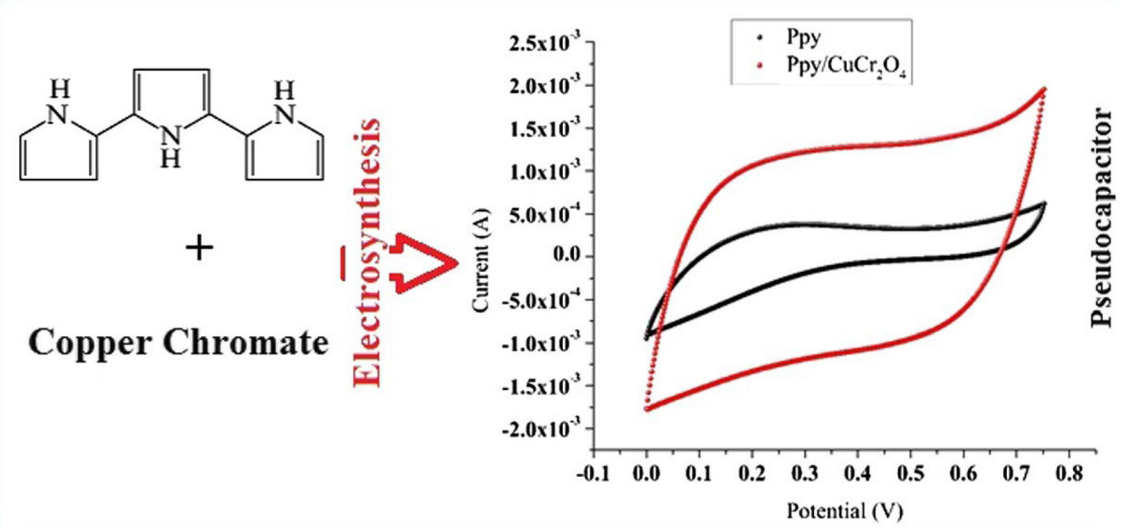


Fig. 33 Ppy/$CuCr_2O_4$ nanocomposite as a pseudocapacitor.[47]

the highest short-circuit photocurrent density and fill factor. The photoelectric efficiency of the La-doped $CuCr_2O_4$ electrode was mainly owing to its shape and the synergistic effect of a dispersive active center.[83] Bhagwan *et al.* demonstrated the application of $CuCr_2O_4$ NPs in supercapacitors, achieving a specific capacity of 72.5 mAh $g^{-1}$ at 1 A $g^{-1}$. Incorporating MWCNTs significantly enhanced the performance, yielding a higher capacity of 108.5 mAh $g^{-1}$. The MWCNT/$CuCr_2O_4$//AC HSC device produced a noteworthy energy density of 32.46 Wh $kg^{-1}$ and a power density of 775 W $kg^{-1}$. The tremendous potential of this material for energy storage applications was demonstrated through hands-on demonstrations, which powered gadgets, including LEDs, a kitchen timer, and a toy fan.[129] The maximum capacitance of 370.5 F $g^{-1}$ of the $CuCr_2O_4$/GO nanocomposite was attained with a 0.1 M $H_2SO_4$ aqueous solution, indicating its potential for capacitive energy storage.[120,143]

Sarkar *et al.* found that the 5 wt% $CuCr_2O_4$ NG nanocomposite exhibited a maximum specific capacitance of 530.6 F $g^{-1}$ at a current density of 0.5 A $g^{-1}$ and demonstrated excellent cycling stability, retaining 98.3% of its capacity after 5000 GCD cycles. $CuCr_2O_4$ enhances the supercapacitive performance by serving as a redox-active material and spacer between NG layers, thereby maintaining structural integrity, preventing agglomeration, and minimizing the capacitance loss.[121] According to Susanti *et al.*, CV and EIS measurements showed that the hybrid supercapacitor electrode (N–rGO/$CuCr_2O_4$) successfully developed a hybrid supercapacitor by combining the characteristics of EDLC and pseudocapacitors.[130] Kumar *et al.* suggested that the NPs exhibited potential as an asymmetric supercapacitor.[73]

Vinothkumar *et al.* explored the potential of $CuCr_2O_4$/$Cr_2O_3$@NF as an efficient material for energy storage. Fig. 34(a) depicts the galvanostatic charge–discharge (GCD) profiles recorded at different current densities (from 1 A $g^{-1}$ to 15 A $g^{-1}$), which display noticeable potential plateaus with non-linear features, indicating the pseudocapacitive behavior of the material. As shown in Fig. 34(b), it is evident that the specific capacitance decreases as the current density increases. Despite this trend, the material exhibits a high specific capacitance of approximately 1027.5 F $g^{-1}$ at 1 A $g^{-1}$ and maintains a good performance even at higher rates. The comparison chart in Fig. 34(c) highlights the superior electrochemical performance of $CuCr_2O_4$/$Cr_2O_3$ NCs over other spinel chromite-based materials. Finally, Fig. 34(d) presents the effective redox pseudocapacitance mechanism involving Cu and Cr ion pairs, enhanced by the well-dispersed nanoparticles and high surface area, which facilitates rapid ion diffusion and redox activity. Furthermore, the asymmetric device ($CuCr_2O_4$/$Cr_2O_3$@NF//AC@NF) delivers an energy density of 38.89 Wh $kg^{-1}$ at 800.02 W $kg^{-1}$ and retains 88.67% of its capacitance after 5000 charge–discharge cycles.[137]

**5.3.2. Hydrogen storage/water splitting.** Lachini *et al.* studied the hydrogen storage properties of $CuCr_2O_4$ NPs employing cyclic voltammetry and charge-discharge chronopotentiometry in a 3 M KOH solution. $CuCr_2O_4$ NPs produced by the sol–gel and green techniques have specific capacitance values of 2427 and 1503 F $g^{-1}$, respectively. Their discharge capabilities were 3011 and 4304 mAh $g^{-1}$ after 11 cycles, respectively. The sol–gel method demonstrated a superior hydrogen storage performance due to the enhanced porosity.[49] Ghorai *et al.* studied the photoelectrochemical oxygen evolution reaction (OER) of a 100% $CuCr_2O_4$/$TiO_2$ nanocomposite and found a current density of 1.513 mA $cm^{-2}$. This was 1.1 and 1.7 times greater than that of the pristine $CuCr_2O_4$ (1.40 mA $cm^{-2}$) and $TiO_2$ (0.91 mA $cm^{-2}$), respectively. When exposed to visible LED light, the 100% $CuCr_2O_4$/$TiO_2$ NC demonstrated extremely strong OER kinetics. In addition to being a suitable option for the oxygen evolution process, it is also a viable choice when exposed to visible LED light at

 

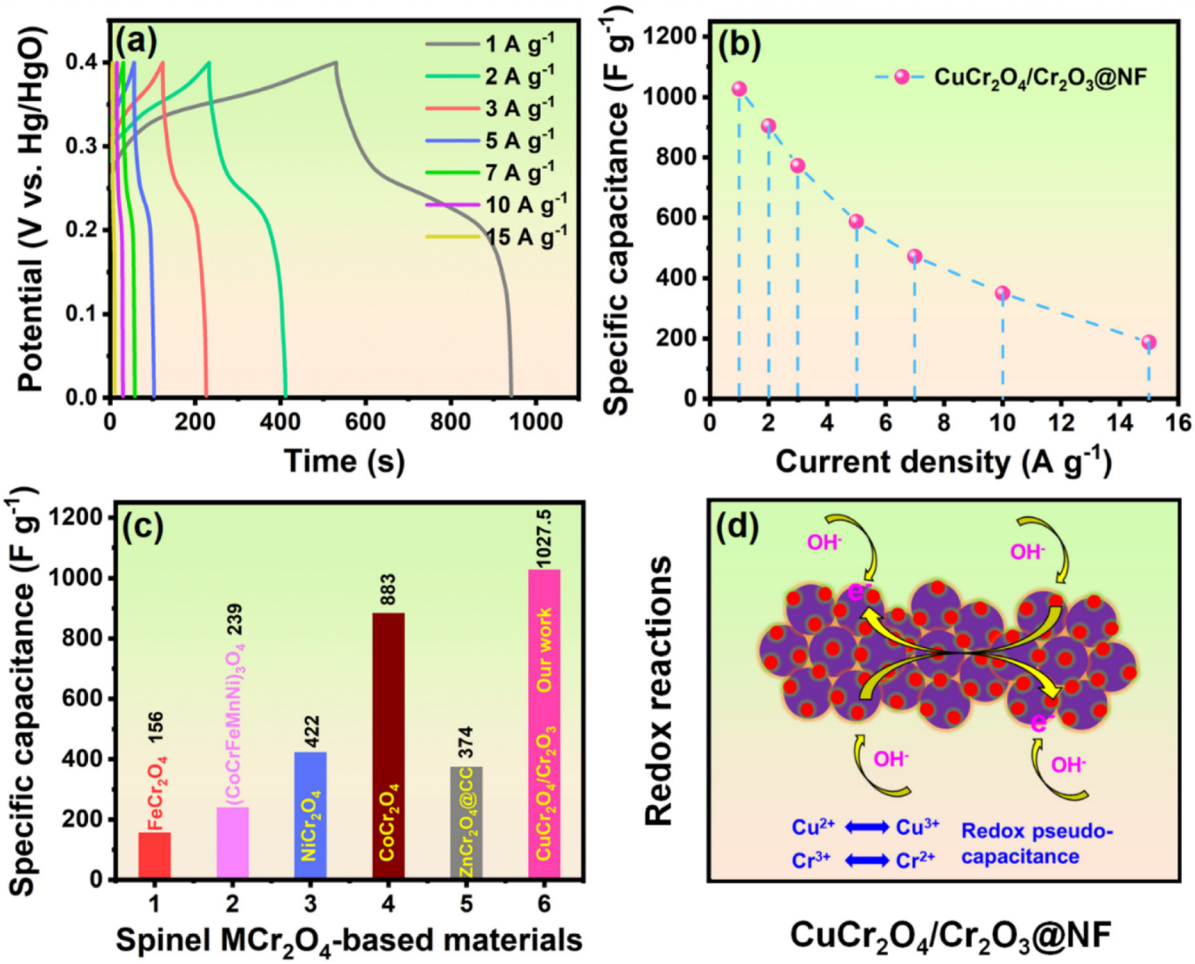


**Fig. 34** (a) GCD curves of $CuCr_2O_4/Cr_2O_3$@NF from 1 to 15 A $g^{-1}$, (b) $C_{sp}$ *vs.* current density of $CuCr_2O_4/Cr_2O_3$@NF, (c) $C_{sp}$ comparison with earlier Cr-related spinel electrodes, and (d) redox reactions of $CuCr_2O_4/Cr_2O_3$@NF.[137]

home. They also examined $^{\bullet}OH$ production in both the DFL and PFL reactions employing the coumarin fluorescence probe approach. This process creates highly fluorescent 7-hydroxycoumarin when the fluorescence-inactive coumarin combines with $^{\bullet}OH$.[48] Shi *et al.* reported that the $CuCr_2O_4/SiO_2$ composite shows reduced diffuse reflectance when wet, turning deep-black with strong solar absorbance, and achieving a water evaporation rate of 1.319 kg $m^{-2}$ $h^{-1}$, underscoring the importance of wet-state optical characteristics for improving photothermal materials.[133]

**5.3.3. Electrochemical activity.** Interestingly, cyclic voltammetry is a popular electrochemical technique for determining the oxidation and reduction potentials of materials. The oxidation potential, which is tied to electron extraction from the highest occupied molecular orbital (HOMO), coincides with the ionization potential. In contrast, the reduction potential is related to electron affinity and reflects the lowest unoccupied molecular orbital (LUMO) of the material. Cyclic voltammograms were produced at various scan rates (20, 50, 200, and 500 mV $s^{-1}$) in studies using BiOBr, $CuCr_2O_4$, and 20% $CuCr_2O_4$/BiOBr, indicating repeatability in anodic and cathodic peak potentials. BiOBr, $CuCr_2O_4$, and 20% $CuCr_2O_4$/BiOBr exhibit HOMO values of ~5.27 eV, ~5.21 eV, and ~5.24 eV, while the LUMO levels are ~2.97 eV, ~3.12 eV, and ~2.98 eV, respectively. Under controlled conditions, the oxidation and reduction potentials of these materials showed minor differences (Fig. 35).[112]

Shafique *et al.* described the electrochemical stability of a nanoelectrode material, which was tested for commercial uses by scanning modified electrodes for 500 cycles in 1 M KOH and 0.1 M $H_2SO_4$ electrolytes at a scan rate of 100 mV $s^{-1}$. EIS spectra show a quicker electron transfer rate in 0.1 M $H_2SO_4$, with a maximum specific capacitance of 445.5 F $g^{-1}$ determined using CV.[122] Furthermore, a three-electrode setup using $CuCr_2O_4$–CTAB as the electrode material produced capacitance values of up to 965 F $g^{-1}$ at a scan rate of 1 A $g^{-1}$. Additionally, it provides excellent cyclic stability in a 1 M $Na_2SO_4$ electrolyte, retaining 91% of its initial capacitance after 5000 cycles.[73]

Using a simple drop-coating method, Kong *et al.* successfully fabricated a non-enzymatic electrochemical $H_2O_2$ sensor. The broad apparent active area of the $CuCr_2O_4$/GCE probe, low charge transfer resistance, and the synergistic redox coupling

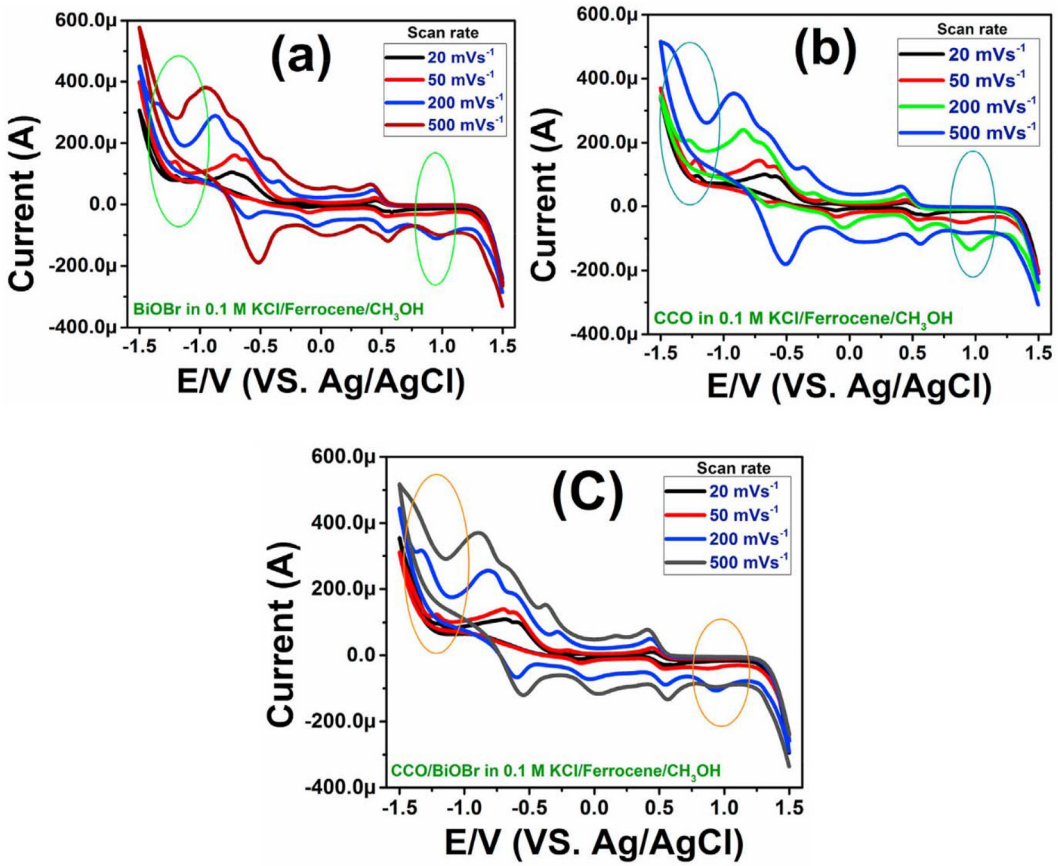


**Fig. 35** Highlighted area in the CV of (a) BiOBr, (b) $CuCr_2O_4$, and (c) 20% $CuCr_2O_4$/BiOBr in 0.1 M KCl/$CH_3OH$/ferrocene shows the change in potential in each case, with GC serving as the working electrode, Pt wire serving as the counter electrode, and Ag/AgCl serving as the reference electrode.[112]

of $CuCr_2O_4$ and GCE were responsible for its high sensitivity (886 μA $mM^{-1}$ $cm^{-2}$), low detection limit (160 nM), and wide linear detection range (0.3 μM to 8.1 mM) in 0.1 M NaOH.[60] Lao *et al.* reported the electrochemical performance of a $CuCr_2O_4$Ag composite. Compared to the uncoated $CuCr_2O_4$, the Ag coating on $CuCr_2O_4$ improves its coulombic efficiency, cycling stability, and initial discharge capacity, making it a more efficient anode material for lithium-ion batteries.[46]

### 5.4. Biological activities of $CuCr_2O_4$ nanomaterials/composite

In the study by Ahmed *et al.*, they examined the toxicity of $CuCr_2O_4$ NPs in MCF-7 cells using the MTT test. The rosemary essential nanoemulsion helps prevent cancer. This study found that rosemary-mediated $CuCr_2O_4$ NPs had a stronger cell-killing effect than Nolvadex-D. The $IC_{50}$ value of the synthesized NPs was 247.7 ppm. Furthermore, a hemolysis assay was performed on red blood cells (RBCs) using different concentrations of the compound. The results revealed no hemolysis at any tested concentration, suggesting that the NPs are non-toxic. This confirms the absence of cytotoxic effects on RBC in the toxicity screening test.[41] Mirzaei *et al.* tested the antibacterial activities of bare or modified NPs against Gram-positive (*S. aureus*) and Gram-negative (*E. coli*) bacteria in silicone rubber and PVDF matrices. They discovered that the size of the NPs and the matrix medium are critical for inhibiting bacterial growth.[42] Khan *et al.* studied antibacterial activities achieved through the photoinhibition of both *E. coli* and *S. aureus* bacteria. $V_2O_5$/$CuCr_2O_4$/MCM-41 inhibited *E. coli* and *S. aureus* in a zone of 18 ± 0.3 mm and 22 ± 0.2 mm, respectively, when exposed to visible light. The nanostructures efficiently inhibited bacterial growth and survival, demonstrating their suitability for applications in water disinfection and $V_2O_5$/$CuCr_2O_4$/MCM-41 antibacterial coatings.[135] Heydari *et al.* evaluated the bone-forming ability of human adipose-derived stem cells (hADSCs) using a nanocomposite scaffold synthesized from glycerol and azelaic acid (Gl–Az) with $CuCr_2O_4$ NPs. The findings demonstrated that the Gl–Az–1%$CuCr_2O_4$ scaffold considerably raised bone differentiation markers in hADSCs after 14 days and exhibited good mechanical strength, biocompatibility, and degradability.[44] $CuCr_2O_4$–$BiI_3O_9$ NCs were tested for their potential genotoxicity on *Allium cepa* root tips. The mitotic cycle and nuclei index impact the genotoxic nature of NCs and phase disruption. Modifying the stages of the cycle impairs protein synthesis and DNA replication, thereby enhancing the cytotoxicity. Furthermore, the NCs

 

Table 7 Summary of the biological activities of $CuCr_2O_4$ nanomaterials/composites

| Nanomaterials | Applications | Cell line/ bacteria | Results | Mechanism of action | Observations | Ref. |
|---|---|---|---|---|---|---|
| Rosemary mediated-$CuCr_2O_4$ NPs | Anti-breast cancer (MTT assay) | MCF-7 | $IC_{50}$-247.7 ppm | Generation of reactive oxygen species (ROS), induced oxidative stress, mitochondrial damage | Dose-dependent cell death: up to 64% reduction at 320 ppm after 24 h; apoptosis observed | 41 |
| Modified $CuCr_2O_4$/ silicone rubber (soaked in Tween80) | Antibacterial activity (Agar diffusion method) | *E. coli*<br>*S. aureus* | ZOI<br>11 mm<br>12 mm | Damage cell membrane | Size and medium are crucial factors in preventing bacterial development because a higher surface area-to-volume ratio promotes better interactions | 42 |
| Bare $CuCr_2O_4$/silicone rubber (soaked in Tween80) | | *E. coli*<br>*S. aureus* | 12 mm<br>14 mm | | | |
| $V_2O_5$/$CuCr_2O_4$/ MCM-41 (light) | Antibacterial activity (Agar well diffusion method) | *E. coli* | ZOI<br>18 ± 0.3 mm<br>MIC<br>50 μg $mL^{-1}$ | Disruption of the cell membrane, and generation of ROS | Blocked bacterial growth and viability | 135 |
| | | *S. aureus* | ZOI<br>22 ± 0.2 mm<br>MIC<br>40 μg $mL^{-1}$ | | | |

Table 8 Summary of the toxicological activity of $CuCr_2O_4$ nanomaterials/composites

| Applications | Effective dose | Mechanism of action | Observations | Ref. |
|---|---|---|---|---|
| Homolysis (blood cells) | 50, 250, and 500 μg $mL^{-1}$ | Disruption of cell membranes | Non-toxic nature for all concentration (no homolysis) | 41 |
| Genotoxicity (*Allium cepa* root tips) | — | DNA damage, chromosomal aberrations | Dependent on the NCs concentration | 45 |

showed no chromosomal aberrations or micronucleus production in *Allium cepa*, indicating their non-genotoxic nature.[45] Moreover, Tables 7 and 8 describe the biological and toxicological activities of $CuCr_2O_4$ nanomaterials/composites.

### 5.5. Miscellaneous applications of $CuCr_2O_4$ nanomaterials/ composite

Pakzad *et al.* investigated spectrally selective absorbers in thermoset acrylate-based coatings on aluminium substrates. The larger particle sizes of the produced $CuCr_2O_4$ NPs exhibit superior solar selectivity. This results in lower thermal emittance ($\varepsilon_T$) in the infrared region (2.5–20 μm) and higher solar absorption ($\alpha_s$) across the solar spectrum (0.3–2.5 μm).[17] The $\eta$ of DSSC was 44% higher than that of the pure $TiO_2$ film electrode. $CuCr_2O_4$/$TiO_2$ composite electrodes can reduce charge recombination by slowing down reverse electron transfer due to their insulating properties. Furthermore, spinel $CuCr_2O_4$ is a narrow-bandgap semiconductor with a gap energy of 1.14 eV, which facilitates the absorption of solar energy in the visible light range, thereby improving the performance of DSSCs.[72] Hu *et al.* described the doping of $MCr_2O_4$ into $TiO_2$ film electrodes, which boosted their absorbance. $CuCr_2O_4$/$TiO_2$ showed superior light responsiveness

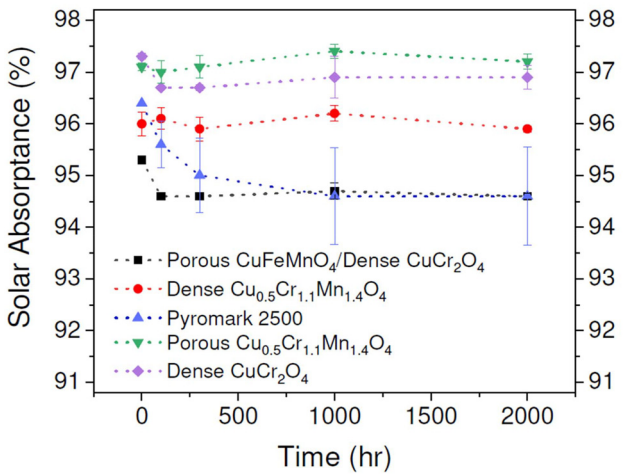


Fig. 36 Dotted line displaying the anticipated trend for solar absorptance value at 800 °C after 100, 300, 1000, and 2000 h.[14]

than $NiCr_2O_4$/$TiO_2$. 2% $CuCr_2O_4$ increased the photoelectric conversion efficiency by 54%, whereas 1% $NiCr_2O_4$ improved it by 30%.[125] Rubin and colleagues investigated solar absorber coatings. The maximum solar absorptance was observed in the porous $Cu_{0.5}Cr_{1.1}Mn_{1.4}O_4$ (Fig. 36), which was 97.1% prior to thermal annealing and remained unchanged during thermal testing, reaching 97.2% after 2000 h. Alternatively, the solar absorptance of Pyromark 2500 significantly decreased, increased from 96.4% to 94.6%.[14]

Javed *et al.* explored the temperature and frequency effect of the electrical conduction and dielectric relaxation mechanisms in $CuCr_2O_4$, tetragonally distorted spinel chromite.[59] The exchange bias behavior was discussed about the exchange coupling between the ferrimagnetic $CuCr_2O_4$ (130 K) and the

antiferromagnetic $Cr_2O_3$ (310 K). The exchange bias in $CuCr_2O_4$–$Cr_2O_3$ was attributed to the exchange coupling between ferrimagnetic $CuCr_2O_4$ (130 K) and antiferromagnetic $Cr_2O_3$ (310 K). Strong exchange bias was noticed in the field-cooled hysteresis loop at low temperatures, with both the exchange bias field and coercive field decreasing as the temperature increased, vanishing at around 200 K.[126]

## 6. Challenges and opportunities

Despite significant advancements, several challenges remain in the synthesis and application of $CuCr_2O_4$ NPs. Achieving precise control over particle size, shape, and crystallinity is challenging, given that the synthesis parameters such as temperature, pH, reaction duration, and surfactants significantly influence the final properties. Scalability and cost-effectiveness also pose hurdles, given that many synthesis methods require high energy inputs or expensive precursors, limiting their commercial viability. Furthermore, to ensure a consistent performance, additional research is also required to determine the stability and reproducibility of $CuCr_2O_4$ NPs under various environmental conditions. Concerns regarding potential cytotoxicity and environmental impact must be addressed before the widespread use of biomedical and industrial applications. According to the literature, $CuCr_2O_4$ nanocomposites and metal-doped $CuCr_2O_4$ NPs have demonstrated a remarkable capacity for energy storage and photocatalytic activity. Additional research is required, especially in the area of green synthesis. Only two studies have reported the green production of $CuCr_2O_4$ NPs from natural sources to date. This opens up a new avenue for research on sustainability. Additionally, creative approaches are necessary to enhance the compatibility and efficiency when integrating these NPs into practical devices, such as sensors, batteries, and catalysts.

However, numerous opportunities exist to overcome these challenges and expand the potential of $CuCr_2O_4$-based materials. Advanced functionalization through metal doping and nanocomposite formation can significantly enhance their catalytic, electrochemical, and biomedical properties. The development of sustainable and green synthesis techniques that use less energy and environmentally benign precursors can improve the scalability, while lessening their negative effects on the environment. $CuCr_2O_4$ NPs have enormous potential for anticancer treatments, antimicrobial coatings, and targeted drug delivery in biomedical applications. Their excellent electrochemical properties also make them ideal candidates for next-generation energy storage devices, including supercapacitors and Li-ion batteries. Furthermore, their integration into smart sensor technologies might result in extremely sensitive and specific detection systems for industrial applications, healthcare diagnostics, and environmental monitoring. By addressing existing challenges and leveraging these opportunities, $CuCr_2O_4$ NPs can be further optimized for cutting-edge applications, driving innovation across multiple scientific and technological domains.

## 7. Conclusion

In this review paper, we provide an overview of breakthroughs in $CuCr_2O_4$ nanostructures, including pristine NPs, metal-doped variants, and nanocomposites, with diverse applications spanning biological, catalytic, electrochemical, and sensing fields. Several procedures exist for the synthesis of $CuCr_2O_4$ nanomaterials, including sol–gel, hydrothermal, solution combustion, co-precipitation, and electrospinning approaches. The fabrication of these NPs is significantly influenced by variables such as temperature, pH, reaction time, precursor concentration, and the selection fuel or surfactant, which directly impact their structural and functional properties. In this review, we demonstrated that $CuCr_2O_4$ NPs demonstrate significant catalytic activity in organic transformations. They also serve as an excellent enhancer of the burning rate for AP-based solid propellant systems. Furthermore, they have demonstrated outstanding potential in energy storage devices such as Li-ion batteries and supercapacitors, as well as electrocatalysis for the OER and HER. $CuCr_2O_4$ NPs show promise in nanomedicine, including anticancer, antibacterial, and genotoxic properties. Their photocatalytic activity has also been widely investigated for the decomposition of dyes and antibiotics. $CuCr_2O_4$ NPs have great promise in these fields due to their unique physical and magnetic features. Future studies should focus on developing sustainable and scalable synthesis techniques, while exploring novel applications of $CuCr_2O_4$-based nanomaterials. By bridging the gap between synthesis and application, this review aims to contribute to the advancement of copper chromite nanotechnology for next-generation scientific and industrial innovations.

## Conflicts of interest

The authors declare no conflict of interest.

## Data availability

No primary research results, software or code have been included and no new data were generated or analysed as part of this review.

## References

1 J. Hulla, S. C. Sahu and A. W. Hayes, Nanotechnology: History and future, *Hum. Exp. Toxicol.*, 2015, **34**(12), 1318–1321.
2 S. Ghotekar, *et al.*, Spinel $ZnCr_2O_4$ nanorods synthesized by facile sol-gel auto combustion method with biomedical properties, *J. Sol-Gel Sci. Technol.*, 2023, **105**(1), 176–185.
3 K. T. Thendral, M. Amutha and R. Ragunathan, Design and development of copper cobaltite ($CuCo_2O_4$) nanoparticle for antibacterial anticancer and photocatalytic activity, *Mater. Lett.*, 2023, **349**, 134720.

 

4 R. Kalia, *et al.*, Photocatalytic degradation properties of Li–Cr ions substituted $CoFe_2O_4$ nanoparticles for wastewater treatment application, *Phys. Status solidi A*, 2022, **219**(8), 2100539.
5 Y. Gao, *et al.*, Spinel $CoMn_2O_4$ hollow nanospheres for very wide linear and sensitive detection of hydrogen peroxide, *J. Alloys Compd.*, 2022, **897**, 163158.
6 H. Adkins and R. Connor, The catalytic hydrogenation of organic compounds over copper chromite, *J. Am. Chem. Soc.*, 1931, **53**(3), 1091–1095.
7 A. M. Kawamoto, L. C. Pardini and L. C. Rezende, Synthesis of copper chromite catalyst, *Aerosp. Sci. Technol.*, 2004, **8**(7), 591–598.
8 P. Sathiskumar, C. Thomas and G. Madras, Solution combustion synthesis of nanosized copper chromite and its use as a burn rate modifier in solid propellants, *Ind. Eng. Chem. Res.*, 2012, **51**(30), 10108–10116.
9 S. Ghotekar, *et al.*, A novel green synthesis of honey-mediated $CoCr_2O_4$ nanoparticles and their expeditious heterogeneous catalytic role for the synthesis of 5-aryl-[1, 2, 4] triazolidine-3-thiones, *Res. Chem. Intermed.*, 2024, **50**(1), 49–68.
10 A. S. Namini, *et al.*, Synthesis and characterization of novel ZnO/$NiCr_2O_4$ nanocomposite for water purification by degradation of tetracycline and phenol under visible light irradiation, *Mater. Res. Bull.*, 2021, **139**, 111247.
11 B. Sriram, *et al.*, Deep eutectic solvent-mediated synthesis of spinel zinc chromite nanoparticles: a simple label-free electrochemical sensor for dopamine and ascorbic acid, *ACS Appl. Nano Mater.*, 2023, **6**(19), 17593–17602.
12 O. Crottaz, F. Kubel and H. Schmid, Jumping crystals of the spinels $NiCr_2O_4$ and$CuCr_2O_4$, *J. Mater. Chem.*, 1997, **7**(1), 143–146.
13 L. Patron, *et al.*, New synthetic route in obtaining copper chromite I. Hydrolysis of some soluble salts, *Mater. Res. Bull.*, 2001, **36**(7–8), 1269–1276.
14 E. B. Rubin, Y. Chen and R. Chen, Optical properties and thermal stability of Cu spinel oxide nanoparticle solar absorber coatings, *Sol. Energy Mater. Sol. Cells*, 2019, **195**, 81–88.
15 S. S. Acharyya, *et al.*, Cetyl alcohol mediated synthesis of $CuCr_2O_4$ spinel nanoparticles: a green catalyst for selective oxidation of aromatic C–H bonds with hydrogen peroxide, *RSC Adv.*, 2015, **5**(7), 4838–4843.
16 J. Safaei-Ghomi, Z. Akbarzadeh and B. Khojastehbakht-Koopaei, C–N cross-coupling reaction catalysed by reusable $CuCr_2O_4$ nanoparticles under ligand-free conditions: a highly efficient synthesis of triarylamines, *RSC Adv.*, 2015, **5**(37), 28879–28884.
17 E. Pakzad, Z. Ranjbar and M. Ghahari, Synthesized of octahedral cupper chromite spinel for spectrally selective absorber (SSA) coatings, *Prog. Org. Coat.*, 2019, **132**, 21–28.
18 Monika, R. Sharma and A. Singh, Structural and optical properties of chromium oxide in $CuCr_2O_{4-\delta}$ nanostructured materials, *Mater. Today: Proc.*, 2023, 1–5.
19 B. Gou, *et al.*, Effect of Nano–Copper Chromite on the Thermal Decomposition and Combustion of AP–Based Solid Propellants, *Propellants, Explos., Pyrotech.*, 2022, **47**(10), e202200087.
20 X. Sun, *et al.*, A CTAB-assisted hydrothermal orientation growth of ZnO nanorods, *Mater. Chem. Phys.*, 2003, **78**(1), 99–104.
21 R. Mohamed, Synthesis and characterization of AgCl@ graphitic carbon nitride hybrid materials for the photocatalytic degradation of atrazine, *Ceram. Int.*, 2015, **41**(1), 1197–1204.
22 W. Yuan, X. Liu and L. Li, Synthesis, characterization and photocatalytic activity of cubic-like $CuCr_2O_4$ for dye degradation under visible light irradiation, *Appl. Surf. Sci.*, 2014, **319**, 350–357.
23 B. Paul, *et al.*, Facile synthesis of spinel $CuCr_2O_4$ nanoparticles and studies of their photocatalytic activity in degradation of some selected organic dyes, *J. Alloys Compd.*, 2015, **648**, 629–635.
24 S. S. Acharyya, *et al.*, Synergistic effect between ultrasmall Cu(II) oxide and $CuCr_2O_4$ spinel nanoparticles in selective hydroxylation of benzene to phenol with air as oxidant, *ACS Catal.*, 2015, **5**(5), 2850–2858.
25 A. Sanoop, R. Rajeev and B. K. George, Synthesis and characterization of a novel copper chromite catalyst for the thermal decomposition of ammonium perchlorate, *Thermochim. Acta*, 2015, **606**, 34–40.
26 K. Mageshwari, *et al.*, Novel $CuCr_2O_4$ embedded CuO nanocomposites for efficient photodegradation of organic dyes, *Appl. Surf. Sci.*, 2015, **353**, 95–102.
27 M. H. Ghasemi and E. Kowsari, The synergistic effect of copper chromite spinel nanoparticles (CuCr 2 O 4) and basic ionic liquid on the synthesis of cyclopropanecarboxylic acids, *Res. Chem. Intermed.*, 2016, **42**, 7963–7975.
28 W. Zhang, *et al.*, Progress of ethylene action mechanism and its application on plant type formation in crops, *Saudi J. Biol. Sci.*, 2020, **27**(6), 1667–1673.
29 X. Zenggang, *et al.*, Research on image retrieval algorithm based on combination of color and shape features, *J. Signal Process. Syst.*, 2021, **93**, 139–146.
30 C. Zuo, *et al.*, Transport of intensity phase retrieval and computational imaging for partially coherent fields: The phase space perspective, *Opt. Laser Eng.*, 2015, **71**, 20–32.
31 C. Zuo, *et al.*, High-speed three-dimensional shape measurement for dynamic scenes using bi-frequency tripolar pulse-width-modulation fringe projection, *Opt. Laser Eng.*, 2013, **51**(8), 953–960.
32 X. Li, *et al.*, Silver–catalyzed decarboxylative allylation of difluoroarylacetic acids with allyl sulfones in water, *Chem. – Asian J.*, 2020, **15**(7), 1175–1179.
33 Y. Liu, *et al.*, Hierarchical nanocomposite electrocatalyst of bimetallic zeolitic imidazolate framework and $MoS_2$ sheets for non-Pt methanol oxidation and water splitting, *Appl. Catal., B*, 2019, **258**, 117970.
34 P. Li, *et al.*, A novel hydrolysis method to synthesize chromium hydroxide nanoparticles and its catalytic effect in

the thermal decomposition of ammonium perchlorate, *Thermochim. Acta*, 2012, **544**, 71–76.
35 S. S. Acharyya, S. Ghosh and R. Bal, Catalytic oxidation of aniline to azoxybenzene over $CuCr_2O_4$ spinel nanoparticle catalyst, *ACS Sustainable Chem. Eng.*, 2014, **2**(4), 584–589.
36 B. M. Latha, V. Sadasivam and B. Sivasankar, A highly selective synthesis of pyrazine from ethylenediamine on copper oxide/copper chromite catalysts, *Catal. Commun.*, 2007, **8**(7), 1070–1073.
37 D. Liu, *et al.*, Deactivation mechanistic studies of copper chromite catalyst for selective hydrogenation of 2-furfuraldehyde, *J. Catal.*, 2013, **299**, 336–345.
38 Z. Karimi-Jaberi, *et al.*, Nano-copper chromite (nano-$CuCr_2O_4$): a novel and efficient catalyst for the synthesis of biscoumarin and pyrano [c] chromene derivatives in water at room temperature, *Res. Chem. Intermed.*, 2016, **42**, 4641–4650.
39 S. S. Acharyya, *et al.*, Preparation of the $CuCr_2O_4$ spinel nanoparticles catalyst for selective oxidation of toluene to benzaldehyde, *Green Chem.*, 2014, **16**(5), 2500–2508.
40 S. Abdolmohammadi and S. Dahi, Azar, Sustainable synthesis of [1] benzopyran azo dyes using $CuCr_2O_4$ NPs., *J. Heterocycl. Chem.*, 2021, **58**(11), 2181–2188.
41 H. S. Ahmed, M. Hammadi and W. Majeed, Green Synthesis of $CuCr_2O_4$ Nano Composite from Rosemary Extract and Evaluation of its Anti-Breast Cancer Properties, *J. Nanostruct.*, 2024, **14**(4), 1183–1190.
42 A. Mirzaei, R. Peymanfar and N. Khodamoradipoor, Investigation of size and medium effects on antimicrobial properties by $CuCr_2O_4$ nanoparticles and silicone rubber or PVDF, *Mater. Res. Express*, 2019, **6**(8), 085412.
43 P. Sankudevan, *et al.*, Enhancement of luminescence mechanisms in structural, morphological, and catalytic properties of undoped $CuCr_2O_4$ and Mn-doped $CuCr_2O_4$, *J. Cluster Sci.*, 2023, **34**(3), 1527–1534.
44 M. Heydari, *et al.*, The role of copper chromite nanoparticles on physical and bio properties of scaffolds based on poly (glycerol-azelaic acid) for application in tissue engineering fields, *Cell Tissue Res.*, 2023, **391**(2), 357–373.
45 S. Balasurya, *et al.*, Novel self-propelled $CuCr_2O_4$-$BiI_3O_9$ nanojets for the efficient photodegradation of organics in wastewater: A non-genotoxic nanomaterial for water treatment, *J. Water Process Eng.*, 2023, **53**, 103657.
46 M. Lao, *et al.*, Enhanced electrochemical performance of Ag-coated $CuCr_2O_4$ as anode material for lithium-ion batteries, *Ceram. Int.*, 2014, **40**(8), 11899–11904.
47 J. S. Shayeh, *et al.*, A novel route for electrosynthesis of $CuCr_2O_4$ nanocomposite with p-type conductive polymer as a high performance material for electrochemical supercapacitors, *J. Colloid Interface Sci.*, 2017, **496**, 401–406.
48 K. Ghorai, *et al.*, Anatase $TiO_2$ decorated $CuCr_2O_4$ nanocomposite: A versatile photocatalyst under domestic LED light irradiation, *Appl. Surf. Sci.*, 2021, **568**, 150838.
49 S. A. Lachini, A. Eslami and M. Enhessari, A comparative study of sol-gel and green synthesized $CuCr_2O_4$ nanoparticles as an electrode material for enhanced electrochemical hydrogen storage, *Int. J. Hydrogen Energy*, 2024, **88**, 841–849.
50 S. G. Hosseini, R. Abazari and A. Gavi, Pure $CuCr_2O_4$ nanoparticles: synthesis, characterization and their morphological and size effects on the catalytic thermal decomposition of ammonium perchlorate, *Solid State Sci.*, 2014, **37**, 72–79.
51 R. Peymanfar and H. Ramezanalizadeh, Sol-gel assisted synthesis of $CuCr_2O_4$ nanoparticles: an efficient visible-light driven photocatalyst for the degradation of water pollutions, *Optik*, 2018, **169**, 424–431.
52 Y. Benrighi, *et al.*, Characterization and application of the spinel $CuCr_2O_4$ synthesized by sol–gel method for sunset yellow photodegradation, *J. Sol-Gel Sci. Technol.*, 2022, **101**(2), 390–400.
53 R. Peymanfar and N. Khodamoradipoor, Preparation and Identification of $CuCr_2O_4$ Nanoparticles and Investigation of Its Microwave Absorption Characteristics at X-Band Frequency Using Silicone Rubber Polymeric Matrix, *Proceedings*, 2018, 1–6.
54 R. Peymanfar and N. Khodamoradipoor, Preparation and characterization of copper chromium oxide nanoparticles using modified sol–gel route and evaluation of their microwave absorption properties, *Phys. Status solidi A*, 2019, **216**(11), 1900057.
55 M. H. Habibi and F. Fakhri, Fabrication and Characterization of $CuCr_2O_4$ Nanocomposite by XRD, FESEM, FTIR, and DRS, *Synth. React. Inorg., Met.-Org., Nano-Met. Chem.*, 2016, **46**(6), 847–851.
56 Y. Wang, *et al.*, Nanochromates $MCr_2O_4$ (M = Co, Ni, Cu, Zn): preparation, characterization, and catalytic activity on the thermal decomposition of fine AP and CL-20, *ACS Omega*, 2019, **5**(1), 327–333.
57 W. Li and H. Cheng, Synthesis and characterization of Cu-Cr-O nanocomposites, *J. Cent. South Univ. Technol.*, 2007, **14**(3), 291–295.
58 J. Billman, *et al.*, $CuCr_2O_4$ particle growth and evolution across sol–gel routes and calcination profiles, *Adv. Appl. Ceram.*, 2023, **122**(3–4), 197–214.
59 M. Javed, *et al.*, Temperature and frequency dependent response of electrical conduction and dielectric relaxation mechanism in $CuCr_2O_4$ tetragonally distorted spinel chromite, *Ceram. Int.*, 2024, **50**(3), 4767–4781.
60 D.-R. Kong, *et al.*, Non-enzymatic $CuCr_2O_4$/GCE amperometric sensor for high sensing and rapid detection of nM level $H_2O_2$, *Microchem. J.*, 2023, **194**, 109343.
61 H. Cui, M. Zayat and D. Levy, Sol-gel synthesis of nanoscaled spinels using propylene oxide as a gelation agent, *J. Sol-Gel Sci. Technol.*, 2005, **35**, 175–181.
62 M. H. Habibi and F. Fakhri, Sol–gel combustion synthesis and characterization of nanostructure copper chromite spinel, *J. Therm. Anal. Calorim.*, 2014, **115**, 1329–1333.
63 B. S. Barros, *et al.*, Preparation and characterization of spinel $MCr_2O_4$ (M = Zn, Co, Cu and Ni) by combustion reaction, *J. Metastable Nanocryst. Mater.*, 2004, **20**, 325–332.

 

64 P. de Jesus Cubas, *et al.*, Synthesis of $CuCr_2O_4$ by self-combustion method and photocatalytic activity in the degradation of Azo Dye with visible light, *J. Photochem. Photobiol., A*, 2020, **401**, 112797.
65 J. V. Viswanath, *et al.*, Copper chromite as ballistic modifier in a typical solid rocket propellant composition: A novel synthetic route involved, *J. Energ. Mater.*, 2018, **36**(1), 69–81.
66 P. Tamizhdurai, *et al.*, Renewable Energy from Waste Plastic: Hydroprocessing of Polypropylene Pyrolysis Oil to Diesel Fuel Using Novel Catalyst. *SSRN*, 2024, 1–29.
67 J. Safaei-Ghomi, B. Khojastehbakht-Koopaei and S. Zahedi, Copper chromite nanoparticles as an efficient and recyclable catalyst for facile synthesis of 4, 4′-(arylmethanediyl) bis (3-methyl-1 H-pyrazol-5-ol) derivatives, *Chem. Heterocycl. Compd.*, 2015, **51**, 34–38.
68 H. Shahbazi-Alavi, J. Safaei-Ghomi and S. H. Nazemzadeh, $CuCr_2O_4$ nanoparticles: An efficient heterogeneous catalyst for the synthesis of bis-thiazolidinones, *Org. Chem. Res.*, 2018, **4**(1), 116–123.
69 M. Edrissi, S. Hosseini and M. Soleymani, Synthesis and characterisation of copper chromite nanoparticles using coprecipitation method, *Micro Nano Lett.*, 2011, **6**(10), 836–839.
70 H. Tavakoli, M. R. Sarraf and A. Zarei, *Inverse Co-precipitation Synthesis of Copper Chromite Nanoparticles*, 2016.
71 L. Pan, *et al.*, Highly photocatalytic activity for p-nitrophenol degradation with spinel-structured $CuCr_2O_4$, *Micro Nano Lett.*, 2012, **7**(5), 415–418.
72 Z. Q. Hu, *et al.*, Preparation and photoelectric properties of $CuCr_2O_4$ nanopowders, *Adv. Mater. Res.*, 2011, **284**, 974–979.
73 S. A. Kumar, T. Shahanas and G. Harichandran, Synthesis and fabrication of tetragonal copper chromite nanospheres for usage as the cathode material in asymmetric supercapacitors, *J. Energy Storage*, 2025, **106**, 114839.
74 S. S. Acharyya, *et al.*, Facile synthesis of $CuCr_2O_4$ spinel nanoparticles: a recyclable heterogeneous catalyst for the one pot hydroxylation of benzene, *Catal. Sci. Technol.*, 2014, **4**(12), 4232–4241.
75 S. S. Acharyya, S. Ghosh and R. Bal, Surfactant promoted synthesis of $CuCr_2O_4$ spinel nanoparticles: a recyclable catalyst for one-pot synthesis of acetophenone from ethylbenzene, *Ind. Eng. Chem. Res.*, 2014, **53**(51), 20056–20063.
76 S. S. Acharyya, *et al.*, Fabrication of $CuCr_2O_4$ spinel nanoparticles: A potential catalyst for the selective oxidation of cycloalkanes via activation of $C_{sp3}$–H bond, *Catal. Commun.*, 2015, **59**, 145–150.
77 S. Mobini, F. Meshkani and M. Rezaei, Surfactant-assisted hydrothermal synthesis of $CuCr_2O_4$ spinel catalyst and its application in CO oxidation process, *J. Environ. Chem. Eng.*, 2017, **5**(5), 4906–4916.
78 S. S. Acharyya, S. Ghosh and R. Bal, Fabrication of three-dimensional (3D) raspberry-like copper chromite spinel catalyst in a facile hydrothermal route and its activity in selective hydroxylation of benzene to phenol, *ACS Appl. Mater. Interfaces*, 2014, **6**(16), 14451–14459.
79 S. Ismael, *et al.*, Facile Synthesis and Catalytic Activity Assessment of Copper Chromite Nanoparticles for Ammonium Perchlorate Decomposition, *J. Phys.: Conf. Ser.*, 2022, 1–11.
80 F. Soleimani, M. Salehi and A. Gholizadeh, Synthesis and characterization of new spinel $Mn_{0.5}Cu_{0.5}Cr_2O_4$ and degradation of Malachite Green from wastewater in comparison with $CuCr_2O_4$, *Int. J. Nano Dimens.*, 2019, **10**(3), 260–271.
81 A. S. Al-Wasidi, *et al.*, Facile hydrothermal synthesis of copper chromite nanoparticles for efficient photocatalytic degradation of acid orange 7 dye, *J. Inorg. Organomet. Polym. Mater.*, 2022, 1–12.
82 N. Bisht, *et al.*, Novel microwave synthesis of copper chromite nanoparticles, *Inorg. Chem. Commun.*, 2021, **134**, 109072.
83 G. Rajeswari, *et al.*, Enhancement of the structure, solar cells and vibrational studies of undoped $CuCr_2O_4$ and La-doped $CuCr_2O_4$ semiconductor compounds, *Heliyon*, 2022, **8**(4), 1–6.
84 F. Chen, *et al.*, Comparative Study of Typical Copper-Based Catalysts for Catalyzing Thermal Decomposition of High Energy Oxidant Ammonium Dinitramide. Available at SSRN 4903523.
85 D. Zhang, *et al.*, Significantly enhanced thermal decomposition of mechanically activated ammonium perchlorate coupling with nano copper chromite, *ACS Omega*, 2021, **6**(24), 16110–16118.
86 M. Han, *et al.*, Spinel $CuB_2O_4$ (B = Fe, Cr, and Al) oxides for selective adsorption of Congo red and photocatalytic removal of antibiotics, *ACS Appl. Nano Mater.*, 2022, **5**(8), 11194–11207.
87 S. Appalakutti, *et al.*, Process intensification of copper chromite ($CuCr_2O_4$) nanoparticle production using continuous flow microreactor, *Chem. Eng. Process.*, 2015, **89**, 28–34.
88 T.-W. Chiu, C.-H. Tu and Y.-T. Chen, Fabrication of electrospun $CuCr_2O_4$ fibers, *Ceram. Int.*, 2015, **41**, S399–S406.
89 D.-C. Tsai, *et al.*, Annealing effect on the structural and optoelectronic properties of Cu-Cr-O thin films deposited by reactive magnetron sputtering using a single CuCr target, *Mater. Sci.-Pol.*, 2023, **41**(1), 191–201.
90 G.-z. Hao, *et al.*, Preparation and characterization of copper-based nanoparticles as catalyst for ammonium perchlorate (AP), in *2015 IEEE 15th International Conference on Nanotechnology (IEEE-NANO)*, IEEE, 2015.
91 J. Schorne-Pinto, *et al.*, Thermodynamic and structural properties of $CuCrO_2$ and $CuCr_2O_4$: experimental investigation and phase equilibria modeling of the Cu–Cr–O system, *J. Phys. Chem. C*, 2021, **125**(27), 15069–15084.
92 A. Wołosiak-Hnat, E. Milchert and G. Lewandowski, The influence of technological parameters on hydrogenolysis of glycerol in the presence of $CuCr_2O_4$ catalyst, *J. Adv. Oxid. Technol.*, 2012, **15**(2), 405–417.

93 A. Ashraf, *et al.*, The potentials of copper chromite nanoparticles on ammonium nitrate decomposition: Towards eco-friendly oxidizers for green solid propellants, *J. Phys.: Conf. Ser.*, 2024, 1–9.
94 K. Batool, *et al.*, Facile chemical synthesis of cadmium and neodymium doped copper chromite by sol gel method, *J. Nanoscope*, 2021, **2**(2), 163–184.
95 T. Anusree and A. A. Vargeese, Enhanced performance of barium and cobalt doped spinel $CuCr_2O_4$ as decomposition catalyst for ammonium perchlorate, *J. Solid State Chem.*, 2022, **315**, 123481.
96 S. S. Acharyya, S. Ghosh and R. Bal, Direct catalytic oxyamination of benzene to aniline over Cu(II) nanoclusters supported on $CuCr_2O_4$ spinel nanoparticles via simultaneous activation of C–H and N–H bonds, *Chem. Commun.*, 2014, **50**(87), 13311–13314.
97 S. S. Acharyyaa, S. Ghosh, S. Adak, R. Singh, V. Kumar and R. Bal, Highly efficient $Cu^{2+}/CuCr_2O_4$ nanoparticles catalyst for selective oxidation of ethanol, *Sci. Lett.*, 2015, **4**, 153.
98 M. Bai, *et al.*, Synthesis and characterization of Fe/Mn co-doped $CuCr_2O_4$ black pigment with high near-infrared reflectance, *Sol. Energy*, 2022, **234**, 240–250.
99 K. Yadagiri, *et al.*, Structural transformation and magnetic properties of Fe-substituted nano $CuCr_2O_4$ spinel structure, *Ceram. Int.*, 2024, **50**(3), 4987–4993.
100 H. Ramezanalizadeh, R. Peymanfar and N. Khodamoradipoor, Design and development of a novel lanthanum inserted $CuCr_2O_4$ nanoparticles photocatalyst for the efficient removal of water pollutions, *Optik*, 2019, **180**, 113–124.
101 S. Jagadeesan, *et al.*, Liquid phase selective oxidation of veratryl alcohol to veratraldehyde using pure and Mg-doped copper chromite catalysts, *RSC Adv.*, 2024, **14**(25), 18093–18102.
102 K. Batool, *et al.*, Synthesis and characterization of Zinc-Doped Copper Chromites by sol gel method, *J. Nanoscope*, 2021, **2**(1), 15–28.
103 Y. Youn, *et al.*, Effects of metal dopings on $CuCr_2O_4$ pigment for use in concentrated solar power solar selective coatings, *ACS Appl. Energy Mater.*, 2019, **2**(1), 882–888.
104 A. T. Apostolov, I. N. Apostolova and J. M. Wesselinova, Magnetic, electric and optical properties of ion doped $CuCr_2O_4$ nanoparticles, *Magnetochemistry*, 2022, **8**(10), 122.
105 K. Batool, *et al.*, Nanosized magnesium doped copper chromites spinel particles synthesis and characterization, *ECS J. Solid State Sci. Technol.*, 2020, **9**(12), 126005.
106 S. Khostavan, *et al.*, The effect of interaction between nanofillers and epoxy on mechanical and thermal properties of nanocomposites: theoretical prediction and experimental analysis, *Adv. Polym. Technol.*, 2019, **2019**(1), 8156718.
107 K. T. Marla and J. C. Meredith, Simulation of interaction forces between nanoparticles: End-grafted polymer modifiers, *J. Chem. Theory Comput.*, 2006, **2**(6), 1624–1631.
108 H. Eslami, M. Rahimi and F. Müller-Plathe, Molecular dynamics simulation of a silica nanoparticle in oligomeric poly (methyl methacrylate): a model system for studying the interphase thickness in a polymer–nanocomposite via different properties, *Macromolecules*, 2013, **46**(21), 8680–8692.
109 P. T. Kien, N. Q. Thiet and T. Van Khai, Promoting aspect of palladium nanoparticles on spinel Pd@ $CuCr_2O_4/\gamma$–$Al_2O_3$ catalytic system in carbon monoxide oxidation, *Vietnam J. Sci. Technol. B*, 2017, **55**(1), 70–76.
110 W. Li, Facile synthesis of monodisperse $Bi_2O_3$ nanoparticles, *Mater. Chem. Phys.*, 2006, **99**(1), 174–180.
111 W. Li and H. Cheng, $Bi_2O_3/CuCr_2O_4$–CuO core/shell structured nanocomposites: Facile synthesis and catalysis characterization, *J. Alloys Compd.*, 2008, **448**(1–2), 287–292.
112 K. Ghorai, *et al.*, Facile synthesis of $CuCr_2O_4$/BiOBr nanocomposite and its photocatalytic activity towards RhB and tetracycline hydrochloride degradation under household visible LED light irradiation, *J. Alloys Compd.*, 2021, **867**, 157947.
113 A. A. Oladipo, $CuCr_2O_4$@ CaFe–LDO photocatalyst for remarkable removal of COD from high-strength olive mill wastewater, *J. Colloid Interface Sci.*, 2021, **591**, 193–202.
114 A. A. Oladipo, Rapid photocatalytic treatment of high-strength olive mill wastewater by sunlight and UV-induced $CuCr_2O_4$@CaFe–LDO, *J. Water Process Eng.*, 2021, **40**, 101932.
115 K. Ghorai, *et al.*, Facile synthesis of $CuCr_2O_4/CeO_2$ nanocomposite: A new Fenton like catalyst with domestic LED light assisted improved photocatalytic activity for the degradation of RhB, MB and MO dyes, *Appl. Surf. Sci.*, 2021, **536**, 147604.
116 C.-L. Chiang, *et al.*, Conversion of hydrogen/carbon dioxide into formic acid and methanol over $Cu/CuCr_2O_4$ catalyst, *Int. J. Hydrogen Energy*, 2017, **42**(37), 23647–23663.
117 R. M. Mohamed and M. W. Kadi, Generation of hydrogen gas using $CuCr_2O_4$-g-$C_3N_4$ nanocomposites under illumination by visible light, *ACS Omega*, 2021, **6**(6), 4485–4494.
118 S. K. Sivaranjani, *et al.*, Efficiency of $CuCr_2O_4$/Titanium dioxide nanoparticles composite for organic dye removal in aqueous solutions, *Environ. Res.*, 2023, **236**, 116692.
119 A. Akhundi and A. Habibi-Yangjeh, Graphitic carbon nitride nanosheets decorated with $CuCr_2O_4$ nanoparticles: novel photocatalysts with high performances in visible light degradation of water pollutants, *J. Colloid Interface Sci.*, 2017, **504**, 697–710.
120 S. K. Korde, *et al.*, *Experimental investigations on copper-based nanoparticles for energy storage applications*, 2023.
121 S. Sarkar, R. Akshaya and S. Ghosh, Nitrogen doped graphene/$CuCr_2O_4$ nanocomposites for supercapacitors application: effect of nitrogen doping on coulombic efficiency, *Electrochim. Acta*, 2020, **332**, 135368.
122 R. Shafique, *et al.*, Fabrication and characterization of MXene/$CuCr_2O_4$ nanocomposite for diverse energy applications, *J. Mater. Res. Technol.*, 2023, **24**, 2668–2677.

 

123 A. Baoum, M. Amin and R. Mohamed, Development of $CuCr_2O_4$ nanocomposite adopting decoration with polyaniline for acridine orange dye degradation, *Appl. Nanosci.*, 2020, **10**, 1501–1510.
124 H. Lahmar, *et al.*, Photocatalytic degradation of crystal violet dye on the novel $CuCr_2O_4/SnO_2$ hetero-system under sunlight, *Optik*, 2020, **219**, 165042.
125 Z. Q. Hu, *et al.*, Preparation and photoelectric properties of spinel $MCr_2O_4$ (M = Cu, Ni) nanopowders, *Adv. Mater. Res.*, 2012, **415**, 1594–1598.
126 Y. Gao, *et al.*, Exchange bias effect in $CuCr_2O_4/Cr_2O_3$ nanogranular systems, *J. Alloys Compd.*, 2016, **673**, 126–130.
127 A. Mohammadi, V. Mahdikhah and S. Sheibani, Mechano-thermally synthesized $CuCrO_2/CuCr_2O_4$ nanocomposite and improvement of photocatalytic activity by structure modification, *Opt. Mater.*, 2022, **131**, 112716.
128 M. Sarafrazi, A. R. Ghasemi and M. Hamadanian, Synergistic effect between $CuCr_2O_4$ nanoparticles and plasticizer on mechanical properties of EP/PU/$CuCr_2O_4$ nanocomposites: Experimental approach and molecular dynamics simulation, *J. Appl. Polym. Sci.*, 2020, **137**(46), 49425.
129 J. Bhagwan and J. I. Han, Facile synthesis of MWCNT/$CuCr_2O_4$ nanocomposite for aqueous hybrid supercapacitor, *Inorg. Chem. Commun.*, 2024, **170**, 113325.
130 D. Susanti, A. N. R. Pratama and H. Nurdiansah, The Effect of Nitrogen on the Capacitive Properties of N-Doped rGO/$CuCr_2O_4$ Composites as Materials for Supercapacitors, *Eng. Chem.*, 2024, **5**, 49–56.
131 M. Daimalah, N. A. Laoufi and A. Mouheb, $CuCr_2O_4$-polystyrene immobilized photocatalyst: Facile fabrication, characterization and enhanced photodegradation of cefixime under visible light, *Mater. Sci. Semicond. Process.*, 2022, **146**, 106675.
132 Z. Chen, *et al.*, Synthesis of $CuCr_2O_4$/Reduced Graphene Oxide Composite: A Green Catalyst for Selective Oxidation of Cyclohexane to Cyclohexanone with Hydrogen Peroxide, *ChemistrySelect*, 2017, **2**(33), 10941–10945.
133 Y. Shi, *et al.*, A robust $CuCr_2O_4/SiO_2$ composite photothermal material with underwater black property and extremely high thermal stability for solar–driven water evaporation, *Adv. Sustainable Syst.*, 2018, **2**(3), 1700145.
134 P. Holec, *et al.*, $ACr_2O_4/SiO_2$ (A = Zn, Cu, Cd) nanocomposites, their preparation and physical properties, *IOP Conf. Ser.: Mater. Sci. Eng.*, 2011, 1–4.
135 I. A. Khan, *et al.*, Dual-functional nanostructures: Photocatalytic and biomedical applications of vanadium oxide activated $CuCr_2O_4$/MCM-41, *Chem. Eng. Sci.*, 2024, **287**, 119714.
136 S. G. Hosseini, H. Sharifnezhad and M. Fathollahi, Quantitative and qualitative characterization of pure copper chromite nanocomposites for photodegradation of p-nitrophenol in aqueous medium, *J. Electron. Mater.*, 2019, **48**(7), 4207–4216.
137 V. Vinothkumar, *et al.*, One-step designing of spinel $CuCr_2O_4/Cr_2O_3$ nanostructures as efficient positive electrode for a high-performance supercapacitor, *Surf. Interfaces*, 2024, **54**, 105290.
138 S. Barman, *et al.*, Kinetics of reductive isopropylation of benzene with acetone over nano-copper chromite-loaded H-mordenite, *Ind. Eng. Chem. Res.*, 2006, **45**(10), 3481–3487.
139 M. Ştefănescu, *et al.*, Preparation and characterization of $CuCr_2O_4/SiO_2$ and $Cu_2Cr_2O_4/SiO_2$ nanocomposites obtained from carboxylate complex combinations, *J. Therm. Anal. Calorim.*, 2019, **138**, 1887–1894.
140 A. Abbasi, *et al.*, Investigation of the synergic effect of silver on the photodegradation behavior of copper chromite nanostructures, *J. Mater. Sci.: Mater. Electron.*, 2019, **30**, 13994–14006.
141 R. Bajaj, M. Sharma and D. Bahadur, Visible light-driven novel nanocomposite ($BiVO_4/CuCr_2O_4$) for efficient degradation of organic dye, *Dalton Trans.*, 2013, **42**(19), 6736–6744.
142 S. G. Hosseini, *et al.*, Orthogonal array design method for optimization experiments of composite oxides ($CuCr_2O_4$/CuO) synthesis and investigation of their catalytic activity on thermal decomposition of ammonium perchlorate particles, *J. Energ. Mater.*, 2024, **42**(2), 187–205.
143 R. Shafique, *et al.*, Copper chromite/graphene oxide nanocomposite for capacitive energy storage and electrochemical applications, *Int. J. Environ. Sci. Technol.*, 2022, **19**(8), 7517–7526.
144 J. Yan, *et al.*, $CuCr_2O_4/TiO_2$ heterojunction for photocatalytic $H_2$ evolution under simulated sunlight irradiation, *Sol. Energy*, 2009, **83**(9), 1534–1539.
145 H. Kumar, *et al.*, The effect of reduced graphene oxide on the catalytic activity of Cu–Cr–O–$TiO_2$ to enhance the thermal decomposition rate of ammonium perchlorate: an efficient fuel oxidizer for solid rocket motors and missiles, *RSC Adv.*, 2017, **7**(58), 36594–36604.
146 A. F. Shojaei, F. Shirini and E. Hedayati, Comparison of selective oxidation of aromatic alcohols using copper(II) chromite-titanium dioxide nanocomposite at reflux, light irradiation, and microwave conditions, *Inorg. Nano-Met. Chem.*, 2017, **47**(9), 1312–1317.
147 M. Nasrollahzadeh, *et al.*, Green synthesis of CuO nanoparticles using aqueous extract of Thymus vulgaris L. leaves and their catalytic performance for N-arylation of indoles and amines, *J. Colloid Interface Sci.*, 2016, **466**, 113–119.
148 F. Nalimu, *et al.*, Review on the phytochemistry and toxicological profiles of Aloe vera and Aloe ferox, *Future J. Pharm. Sci.*, 2021, **7**(1), 145.
149 M. Sánchez, *et al.*, Pharmacological update properties of Aloe vera and its major active constituents, *Molecules*, 2020, **25**(6), 1324.
150 S. Arunkumar and M. Muthuselvam, Analysis of phytochemical constituents and antimicrobial activities of Aloe

vera L. against clinical pathogens, *World J. Agric. Sci.*, 2009, **5**(5), 572–576.

151 K. Patel, *et al.*, Insights into the solar-light-driven photocatalysis of greenly synthesized $CoCr_2O_4$ nanoparticles using Azadirachta indica, *J. Sol-Gel Sci. Technol.*, 2025, 1–18.

152 H. Shahbazi-Alavi, *et al.*, Nano-$CuCr_2O_4$: an efficient catalyst for a one-pot synthesis of tetrahydrodipyrazolopyridine, *J. Chem. Res.*, 2016, **40**(6), 361–363.

153 Y. Luo, *et al.*, Selective catalytic transformation of cellulose into bio-based cresol with $CuCr_2O_4$@ MCM-41 catalyst, *Cellulose*, 2022, **29**(1), 303–319.

154 S. Abdolmohammadi, H. Shahrokhi and S. Dahi-Azar, An Efficacious Synthesis of Xanthenones and Chromenopyrimidinediones Catalyzed by Copper Chromite Nanoparticles and Preliminary Assessment of Their Bioactivity, *Polycyclic Aromat. Compd.*, 2024, **44**(1), 418–430.

155 M. H. Ghasemi and E. Kowsari, The synergistic effect of copper chromite spinel nanoparticles ($CuCr_2O_4$) and basic ionic liquid on the synthesis of cyclopropanecarboxylic acids, *Res. Chem. Intermed.*, 2016, **42**, 7963–7975.

156 P. R. Patil, V. e. N. Krishnamurthy and S. S. Joshi, Effect of nano–copper oxide and copper chromite on the thermal decomposition of ammonium perchlorate, *Propellants, Explos., Pyrotech.*, 2008, **33**(4), 266–270.

157 H. Lahmar, *et al.*, Photocatalytic reduction of Cr(VI) on the new hetero-system $CuCr_2O_4$/ZnO, *J. Mol. Catal. A: Chem.*, 2012, **353**, 74–79.

158 R. Vinu, S. U. Akki and G. Madras, Investigation of dye functional group on the photocatalytic degradation of dyes by nano-$TiO_2$, *J. Hazard. Mater.*, 2010, **176**(1–3), 765–773.

159 X. Liu, *et al.*, Light down-converting characteristics of ZnO–$Y_2O_2S$: $Eu^{3+}$ for visible light photocatalysis, *J. Colloid Interface Sci.*, 2013, **404**, 150–154.

160 P. Amornpitoksuk, *et al.*, Effect of phosphate salts ($Na_3PO_4$, $Na_2HPO_4$, and $NaH_2PO_4$) on $Ag_3PO_4$ morphology for photocatalytic dye degradation under visible light and toxicity of the degraded dye products, *Ind. Eng. Chem. Res.*, 2013, **52**(49), 17369–17375.

161 X. Cai, *et al.*, Photocatalytic degradation properties of Ni$(OH)_2$ nanosheets/ZnO nanorods composites for azo dyes under visible-light irradiation, *Ceram. Int.*, 2014, **40**(1), 57–65.

162 K. Pagar, *et al.*, Bio-inspired Sustainable Fabrication of CdO Nanoparticles Using Citrus sinensis Peel Extract for Photocatalytic Degradation of Rhodamine B Dye, *Top. Catal.*, 2024, **67**(17), 1169–1182.

163 H. Lund, Renewable energy strategies for sustainable development, *Energy*, 2007, **32**(6), 912–919.

 